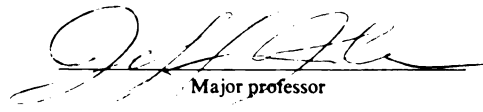




This is to certify that the
dissertation entitled
"Precision Infrared and Visible Solar Photometry
A Photometric Study of the Solar Irradiance Variation"
presented by
Haosheng Lin
has been accepted towards fulfillment
of the requirements for
Ph.D. degree in Physics



Major professor

Date November 10, 1992

**LIBRARY
Michigan State
University**

**PLACE IN RETURN BOX to remove this checkout from your record.
TO AVOID FINES return on or before date due.**

DATE DUE	DATE DUE	DATE DUE
_____	_____	_____
_____	_____	_____
_____	_____	_____
_____	_____	_____
_____	_____	_____
_____	_____	_____
_____	_____	_____

PRECISION INFRARED AND VISIBLE SOLAR PHOTOMETRY
A PHOTOMETRIC STUDY
OF
THE SOLAR IRRADIANCE VARIATION

By

Haosheng Lin

A DISSERTATION

Submitted to

Michigan State University

in partial fulfillment of the requirements

for the degree of

DOCTOR OF PHILOSOPHY

Department of Physics and Astronomy

1992

ABSTRACT

PRECISION INFRARED AND VISIBLE SOLAR PHOTOMETRY A PHOTOMETRIC STUDY OF THE SOLAR IRRADIANCE VARIATION

By

Haosheng Lin

The solar irradiance was observed to be varying with time scale of days to the 11 years solar cycle time scale. The daily variations were well correlated with the passage of the dark sunspots and bright facular area on the photosphere. However, the cause of the small irradiance variation with amplitude of 10^{-3} of the total solar irradiance correlated with the solar cycle is not well understood. Several scenarios with observable surface effects were suggested by various authors to explain this phenomenon, but no observational confirmation is available up to date. Thus, a precision Solar Photometric Telescope (SPT) was constructed to study the large scale brightness structure of the solar photosphere. This instrument does full disk, broad band (10 nm FWHM), two colors (500 nm and 650 nm) imaging of the solar photosphere. Photometry with a newly constructed Infrared Array Camera (IAC) extends these measurements to 1.2, 1.6 and 2.2 micron. This dissertation reports the observations done with these instruments, which revealed low contrast brightness structures with scale ranging from 10^4 km to some fraction of the solar disk on the solar photosphere. The contribution of these structures to the total solar irradiance were discussed.

For Peiling

ACKNOWLEDGEMENTS

Living in a foreign land is no easy task for anybody. Studying in a foreign university is even harder. I would like to thank the many people who helped to make it easier, and turn it into a wonderful adventure.

First I would like to thank my wife, Peiling, who shared all the frustrations and joys with me, and provided a home full of love. She also shielded me from all the distractions in life so I could finish this dissertation.

Dr. Jeffrey R. Kuhn, with whom I learned all the fun of the astrophysics of the sun and astronomy in general, also gave the living example of a great scientist at work. He was also the first person to greet us with warm welcome. All the astronomy folks in the north wing of the third floor, especially Debbie Benedict, provided a homelike atmosphere in which I can do my work and sometimes just hang around.

I am grateful to the observing staffs of the National Solar Observatory at Sacramento Peak, New Mexico, who helped with the infrared observations that comprise half of the data presented in this dissertation. The hospitality of the whole Sac. Peak community also made our three months' stay a memorable experience.

Finally, I would like to thank my parents and my brothers and sisters for their love and support, without which I won't have been able to finish my study.

TABLE OF CONTENTS

INTRODUCTION	1
1.1 Motivation	1
1.2 The Physics	6
1.2.1 Magnetohydrodynamics	7
1.2.2 The Surface Magnetic Field	11
1.2.3 The Subsurface Magnetic Field	15
1.3 This Thesis	17
1.4 Related Subjects	20
INSTRUMENTATION	24
2.1 General Considerations	24
2.2 The Solar Photometric Telescope	26
2.2.1 Optical System	30
2.2.2 The Shutter Assembly	32
2.2.3 The Computer Control and Data Acquisition System	34
2.3 The Infrared Array Camera	36
OBSERVATIONS AND DATA REDUCTION	39
3.1 Observing Procedure	39
3.2 The Visible Wavelength Data	40
3.3 The Infrared Data	42
3.4 Data Reduction	42

3.4.1 Dark Subtraction and Flatfielding	44
3.4.2 Calibration of Solar Disk Center	56
3.4.3 Image Shift and Rotation	57
3.4.4 Image Distortion Correction	58
3.4.5 Image Averaging	61
3.4.6 Fractional Residual Image Construction	61
PROPERTIES OF PHOTOSPHERIC	
NETWORK AND FACULAE	63
4.1 Introduction	63
4.2 Noise Estimate	67
4.3 Properties of The Photospheric Network	72
4.3.1 Cross-Correlation Between Different Timesteps and Colors	72
4.3.2 Power Spectrum Analysis	73
4.3.3 Cross-Correlation With the Chromospheric Network	81
4.3.4 Cross-Correlation With the Supergranulation Velocity Field	82
4.3.5 Line Contribution to the Network Contrast	85
4.3.6 Photospheric Network Contrast Near Disk Center	88
4.3.7 Center-to-Limb Variation of Network Contrast	89
4.3.8 Temperature Structure of Supergranulation	96
4.4 Properties of Photospheric Faculae	96
4.4.1 Spatial Distribution of Faculae	96
4.4.2 Faculae Contrast Near Disk Center and its Center-To-Limb Variation	97
THE SOLAR IRRADIANCE VARIATIONS	
AND CONCLUSIONS	105

5.1 Introduction	105
5.2 Irradiance Contribution of Faculae and Sunspots	107
5.3 Energy Balance of Active Regions	109
5.4 The Average Photosphere	113
5.5 Interpretations	117
5.6 Conclusions	122

APPENDICES

Appendix A On The Gauge Freedom of the Gain Iterating Algorithm	123
Appendix B Least Square Algorithm to Find the Disk Center Coordinates of Full Disk Solar Images	127
Bibliography	131

LIST OF TABLES

Table 3.1 Summary of Visible Wavelength Observations	40
Table 3.2 Summary of Infrared Wavelength Observations	42
Table 5.1 The Sunspots and Faculae Irradiance Contributions of 1991 Data	108

LIST OF FIGURES

Figure 1.1 Solar Irradiance Data from ACRIM and ERB Experiments	2
Figure 2.1 System Diagram of the Solar Photometric Telescope	27
Figure 2.2 The Heliostat of the SPT	28
Figure 2.3 The Optical System of the SPT	29
Figure 2.4 Ray-Tracing Diagram of the Optics of the SPT in Low Resolution Mode.	31
Figure 2.5 Ray-Tracing Diagram of the Optics of the SPT in High Resolution Mode.	33
Figure 2.6 The Shutter Assembly and the Filter Wheel	35
Figure 2.7 Experimental Setup of the Infrared Array Camera	38
Figure 3.1 Raw Solar Image in the Green Bandpass	41
Figure 3.2 Raw Solar Image in the Infrared H Band	43
Figure 3.3 Green Bandpass Flatfield	45
Figure 3.4 Infrared H Band Flatfield	46
Figure 3.5 Green Time-Averaged Solar Image	47
Figure 3.6 H Band Time-Averaged Solar Image	48
Figure 3.7 Time-Averaged Residual Image in the Green Bandpass Before Distortion Correction	49
Figure 3.8 Time-Averaged Residual Image in the Green Bandpass	50
Figure 3.9 Time-Averaged Residual Image in the Red Bandpass	51
Figure 3.10 Time-Averaged Residual Image in the Infrared J band	52

Figure 3.11 Time-Averaged Residual Image in the Infrared H band	53
Figure 3.12 Residual Image in the Infrared K band	54
Figure 3.13 $A_2(r)$ Optical Distortion Amplitude	60
Figure 4.1 Histograms of Contrast from Quiet and Active Regions	65
Figure 4.2 Difference Between Active and Quiet Region Contrast histograms	66
Figure 4.3 Red Contrast Image with Large Scattered Light Contamination	71
Figure 4.4 Filtered Green Band Contrast Image Showing Photospheric Network	74
Figure 4.5 Filtered Red Band Contrast Image Showing Photospheric Network	75
Figure 4.6 Cross-Correlation of Visible Wavelengths Images	76
Figure 4.7 Cross-Correlation of Infrared wavelengths Images at Disk Center	77
Figure 4.8 Comparison of Faculae in J and H Band Near Disk Center	78
Figure 4.9 Average Power Spectrum of Photospheric Network	79
Figure 4.10 Cross-Correlation Between Photospheric Network and Ca K Network	83
Figure 4.11 Cross-Correlation Between Supergranulation and Photospheric Network	84
Figure 4.12 Transmission Function of the Red Filter	87
Figure 4.13 Transmission Function of the Green Filter	90
Figure 4.14 Photospheric Network Contrast Near Disk Center	86
Figure 4.15 Network Contrast Center-to-Limb Variation in Green Band	91
Figure 4.16 Network Contrast Center-to-Limb Variation in Red Band	92
Figure 4.17 Network Contrast Center-to-Limb Variation in Infrared H Band	93
Figure 4.18 Network Contrast Center-to-Limb Variation in Infrared K Band	94
Figure 4.19 Center-to-Limb Variation of Faculae Contrast	103
Figure 5.1 Sunspots and Faculae Irradiance Contribution	110
Figure 5.2 The Average Photosphere in Green Bandpass	115
Figure 5.3 The Average Photosphere in Red Bandpass	116

Figure 5.4 Limb Brightness Profile of the Average Photosphere	118
Figure 5.5 Brightness Temperature Profile of The Average Photosphere	119

CHAPTER 1

INTRODUCTION

1.1 Motivations

The Active Cavity Radiometer Irradiance Monitor (ACRIM) experiment on board the Solar Maximum Mission (SMM) satellite (Willson and Hudson 1988), and the Earth Radiation Budget (ERB) experiment on board the Nimbus-7 satellite revealed that the solar irradiance is variable (Figure 1.1). The time scale of this variation ranges from days to years. On the time scale of days, the irradiance is observed to vary with amplitude of a few tenths of a percent. On the long term, the irradiance increases and decrease with sunspot number, being higher by 1×10^{-3} during the solar maximum. The integrated-light observations of ACRIM and ERB do not provide us information on how the sun modulates its radiative output, nor does it tell us if it is the total luminosity that is changing. However, correlations suggest that the mechanism is related to the magnetic activity on the sun.

Solar magnetic activity manifests itself as magnetic flux tubes with various sizes in the solar photosphere. Brightness changes are always associated with these magnetic flux tubes. The sunspots are the best known. They appear as dark spots on the Solar photosphere, and reduce the total Solar irradiance. Faculae are also associated with the surface magnetic flux tubes. They are the most visible bright feature in a whitelight Solar image. However, their brightness is not exceedingly high when observed with moderate spatial resolution. Their brightness is the great-

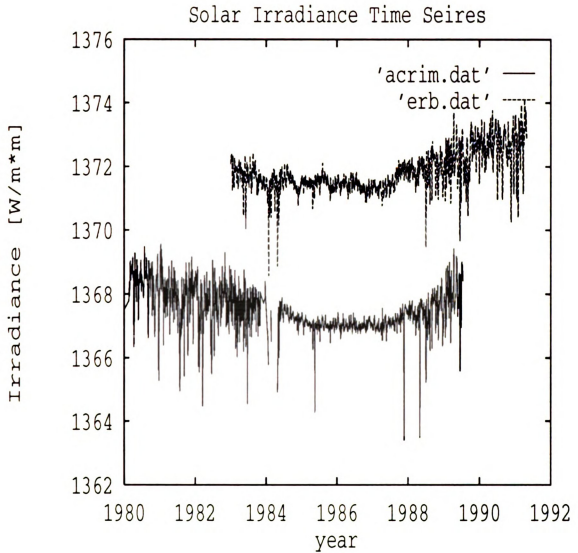


Figure 1.1 Solar Irradiance Data From ACRIM and ERB Experiments. The offset of about 3 W/m^2 is due to a real difference of the absolute calibration between the two instruments. The large fluctuations of the irradiance with short timescales, as well as the slow decrease toward 1986 and the subsequent increase of the irradiance are truly of solar origin. This is evident from the good agreement between the two data sets.

est near the Solar limb, and falls off rapidly as they are rotated into disk center. Since sunspots and faculae are the most visible brightness components on the Solar surface, it is only natural to try to model the Solar irradiance variations with only the contributions from these two components. The brightness of a large sunspot can be as low as about 20 % of the quiet photosphere. Indeed, the passage of large sunspot groups across the observable solar disk was found to be well correlated with large dips in the ACRIM and ERB data.

An early difficulty was that there were no ground based observations with photometric accuracy comparable to the satellite experiments to directly measure the irradiance contributions of each magnetic element. Thus, sunspot and facular contributions were modeled in terms of the Photometric Sunspot Index (PSI) and Photometric Faculae Index (PFI). That is, given the measured contrast of sunspot and faculae as a function of μ , the cosine of the angle between our line-of-sight to the disk center and the radius vector of the sunspot/faculae, one can infer the irradiance contribution of the sunspot/faculae from its area. The daily sunspot and facular area can be measured from the synoptic measurements being carried out at the major observatories. Calculations of this type were able to model the short-term irradiance variations reasonably well (Willson, Gulkis, Janssen, Hudson, and Chapman 1981). However, people also realized that the 11-year irradiance variations cannot be accounted for with just the sunspot and facular contributions (see the review articles of, e.g. Chapman 1987, Hudson 1988, and Fröhlich, Foukal, Hickey, Hudson, and Willson 1991).

In an attempt to identify the brightness structure that is modulating the solar irradiance, Foukal and Lean (1988) compared the Data from ACRIM and the ERB experiment with the HeI $\lambda 10830$ Å index, and CaII K plage data. Both the

HeI $\lambda 10830 \text{ \AA}$ and CaII K are resonance absorption lines in the solar Fraunhofer spectrum. The electron configuration of the CaII ion is $1s^2 2s^2 2p^6 3s^2 3p^6 4s^1$. The transitions between the $2s$ and $2p$ states form a doublet at $\lambda = 3934 \text{ \AA}$ and $\lambda = 3968 \text{ \AA}$, known as the CaII K and H lines, respectively. The CaII K line has a total angular momentum of $J = 3/2$, and is the stronger of the doublet. It is formed in the chromosphere, and its brightness was found to be well correlated with the magnetic field strength (Frazier, 1970). The full-disk integrated CaII K flux thus measures the magnetic activity of the sun, and spatially resolved CaII K spectroheliograms are used to measure the area of faculae, or the CaII K plage index. The HeI $\lambda 10830 \text{ \AA}$ line is the result of the transition between the $2s$ and $2p$ states of neutral helium. Its strength is increased in magnetic elements like plages, and prominences, and its equivalent width was found to be well correlated with global magnetic activity (Harvey 1984, Donnelly, Harvey, Heath, and Repoff 1985), and Foukal et al. used it as a measurement of the combined area of the faculae and network. They found that while the short term irradiance variation is well modeled by the sunspot index and the CaII K plage index, the long-term irradiance variations must be modeled with the HeI $\lambda 10830 \text{ \AA}$ index. This they argued is the proof of the need of a third component, the "active network" contribution, to account for the observed total solar irradiance variation.

The limb brightness measurement (Kuhn, Libbrecht, and Dicke 1988) provided more evidence of a third contribution to the solar irradiance. In this experiment, Kuhn et al. showed evidence of a variable limb brightness temperature excess at active latitudes with an amplitude (peak-to-peak) of 7 K correlated with the SMM measurements. Assuming that this limb brightness excess is a thermal temperature excess, integration over the Solar disk reproduced the solar cycle irradiance variation

observed by SMM. Another important result of this experiment is that the polar flux did not change as the active latitudes flux did. This implies that the Solar luminosity is indeed varying with the Solar cycle.

The "active network model" of Foukal interprets the solar irradiance variation as the result of the solar cycle modulation of the brightness of the surface magnetic elements, and it favors the surface magnetic field to modulate the solar irradiance output. The limb brightness observations of Kuhn et al. may not be incompatible with the "active network" model at first glance. Indeed, the higher photospheric brightness along the active latitudes may be due to a higher active network contrast, which is unresolved in the limb brightness observations and is included in the quiet photosphere components. However, Kuhn et al. argued that it is due to a real increase in the photospheric temperature along the solar active latitudes, and that a deep-seated horizontal magnetic field under the active latitudes is the modulating mechanism of the observed solar irradiance variations. Thus, there are subtle differences between the two models. Which is right? Unfortunately, there are not enough observations to prove or disprove either model. The satellite measurements of the irradiance are spatially unresolved, and they don't provide a clear picture of what is causing the total irradiance variation. Modeling with proxy measurements relies on our knowledge of the sunspot and facular contrast center-to-limb variations which may be enough to model variations in the total solar irradiance, but they don't tell us much about the sun. The limb brightness observations did provide some spatial resolution, but it still is not enough for a full understanding for the irradiance modulating mechanism at work. Thus, the next logical step would be a precise, spatially resolved full-disk photometric measurement to try to resolve the contributions of the various brightness components on the Solar photosphere, and

this is the motivation for this research.

Before large format CCD detectors were made generally available to the astronomy community, photoelectric imaging was done by scanning with single element detectors, or with linear array detectors. The Extreme Limb Photometer (ELP) of Chapman and Meyer (1986) and the observations of Hirayama, Hamana, and Mizugaki (1985) are two examples. This type of observation requires a long scanning process to obtain large area coverage, and the fluctuating atmosphere of the earth limits the large-scale photometric sensitivity. The ELP and the photometer of Hirayama et al. produced some useful results on the facular contrast measurements, however, no measurements of the total solar irradiance variations were achieved with this type of instruments.

The first attempt to do precise full disk photometric observation of the Sun with CCD array detectors was reported by Nishikawa (1990a, 1990b) and Nishikawa and Hirayama (1990). These experiments employed two telescopes equipped with video CCD cameras to obtain simultaneous 2-color measurements of the Sun. Nishikawa was able to reproduce the short-term solar irradiance variation measured by ACRIM, taking into account only the contributions from faculae and sunspots. However, the author concluded that the large scale noise in their data was too great and it was useless for the study of large scale brightness structure contributions to the total irradiance.

1.2 The Physics

We have learned a lot from observations about the Solar irradiance variations. However, as discussed above, these observations not only did not provide clear-cut answers to the questions we had, but raised more new questions. On the theoretical side, the situation isn't any better. We know that the Solar magnetic field is at

work, but exactly how is not clear. In the outer 25 % or so of the solar radius, convection is the dominant mechanism of energy transport. The full hydrodynamic fluid equations of convection are complicated and analytical solution is impossible. Mixing-Length theory is the best model we have to treat this problem. The Sun is composed mainly of hydrogen and helium. Hydrogen accounts for about 91 % of the solar materials, and helium accounts for 8 %. The remaining 1 % is a mixture of the heavier elements (Zirin 1988). The ionization energy of hydrogen atom is 13.6 eV, and the hydrogen atoms can easily be ionized at 15000 K. Thus, the majority of the hydrogen atoms are ionized except for the outermost layer where the temperature of the solar plasma drops below the hydrogen ionization temperature. The boundary of the hydrogen ionization layer is about 2000 km below the photosphere. Since the solar plasma is highly ionized, the convective efficiency may be strongly influenced by the presence of magnetic fields.

The solar magnetic field on the surface manifests itself in the form of sunspots, faculae and network. Deeper into the interior, we believe there exists a global-scale magnetic field. The effect of the surface magnetic field is readily observable, and there are models explaining qualitatively the brightness of faculae and darkness of sunspots (Spruit, 1977, Deinzer, Hensler, Schüssler, and Weisshaar, 1984, Schatten, Mayr, Omidvar, and Maier 1986, Knölker, Schüssler, and Weisshaar, 1988). The effects of the subsurface magnetic field is less certain, because the opacity of the solar plasma limits our ability to probe deep into the solar interior. Despite these limitations, we will review theories related to this subject and will try to patch together a picture of how the magnetic fields modulate the solar radiative output.

1.2.1 The Magnetohydrodynamics

Although the MHD problem of the solar plasma is complicated and there are few

analytical solutions, we can still gain some insight by examining some special cases for which analytical solutions are possible. An important concept, the "frozen-in" field, is the basis of almost all the modeling concerning solar magnetic phenomenon. It is a special case when the magnetic Reynolds number R_M of the solar plasma is large and the magnetic field is carried with the fluid flow, or "frozen" into the fluid flow. Its physics is described below.

The behavior of plasma in a magnetic field is governed by the Maxwell equations and the hydrodynamic equations. Since the solar plasma is highly ionized, it can be considered as a good conductor and the Maxwell's displacement current can be ignored. Thus, we have the two curl equations for the magnetic and electric field in cgs unit as

$$\nabla \times \vec{\mathbf{E}} = -\frac{1}{c} \frac{\partial \vec{\mathbf{B}}}{\partial t} \quad (1-1)$$

$$\nabla \times \vec{\mathbf{B}} = \frac{4\pi}{c} \vec{j} \quad (1-2)$$

In the presence of magnetic field, the generalized Ohm's law includes the Lorentz force,

$$\vec{j} = \sigma \left(\vec{\mathbf{E}} + \frac{\vec{v}}{c} \times \vec{\mathbf{B}} \right) \quad (1-3)$$

where σ is the conductivity of the plasma. When combined, these three equations give the induction equation of $\vec{\mathbf{B}}$ that describes the time variation of the magnetic field:

$$\frac{\partial \vec{\mathbf{B}}}{\partial t} = \nabla \times (\vec{v} \times \vec{\mathbf{B}}) + \eta \nabla^2 \vec{\mathbf{B}} \quad (1-4)$$

where $\eta = c^2/4\pi\sigma$ is the magnetic diffusivity. In the special case with $\vec{v} = 0$, equation (1-4) becomes a diffusion equation.

$$\frac{\partial \vec{\mathbf{B}}}{\partial t} = \eta \nabla^2 \vec{\mathbf{B}} \quad (1-5)$$

Equation (1-5) indicates that the initial configuration of magnetic field will decay in a diffusion time scale of

$$\tau_D = \frac{4\pi\sigma L^2}{c^2} \quad (1-6)$$

where L is the scale length of the spatial variation of $\vec{\mathbf{B}}$. The typical diffusion time scale in the solar environment for magnetic structure like sunspot is of order of 10^2 years.

A different limiting case is that the plasma is in motion and has negligible electrical resistance. Then equation (1-4) becomes

$$\frac{\partial \vec{\mathbf{B}}}{\partial t} = \nabla \times (\vec{v} \times \vec{\mathbf{B}}) \quad (1-7)$$

This equation says that the magnetic field flux through any loop moving with the local fluid velocity is constant in time, or, the magnetic field line is frozen into the fluid and are carried along with it.

In general, both the diffusion term and the transport term in the right-hand-side of equation (1-4) are not negligible, and the time-variation of $\vec{\mathbf{B}}$ is the combination of the two effects. Simple dimensional considerations show that when the product of the characteristic size and velocity of the system is large compared with the diffusion constant η , then the transport term dominates the diffusion term. Hence, we can define a magnetic Reynolds number R_M given by

$$R_M = \frac{LV}{\eta} \quad (1-8)$$

where L and V are the scale length, and characteristic velocity of the fluid, respectively. If R_M is large compared with unity, then the transport term dominates the diffusion term. If R_M is small, then the diffusion term dominates. In the solar environment, the magnetic Reynolds number is usually large, due to the large size and velocity of the system involved. Thus, the frozen-in field approximation is a good working assumption.

The predominant magnetic field configuration in the sun is the magnetic flux tube, at least near the surface. In the solar convection zone, the convective flow tends to carry the magnetic flux tube with it, due to the large magnetic Reynolds number R_M . However, the magnetic flux tubes of sunspot and faculae do not just float around, but are anchored at the base of the convection zone. Thus they will only be bent, instead of been carried away. The magnetic energy $B^2/8\pi$, and magnetic tension $B^2/4\pi$ along the direction of the field lines associated with any magnetic field, may affect fluid motion. The mechanical effect of the magnetic energy is the magnetic pressure, and can be neglected when considering the interaction between the magnetic field and the fluid flow. Its effect is to reduce the thermal

pressure inside the flux tube, since the pressure balance between the ambient non-magnetic plasma and the magnetic flux tube must be maintained. The magnetic tension tends to resist the bending, or in other words, obstruct the fluid motion perpendicular to the direction of the field.

1.2.2 The Surface Magnetic Fields

The surface magnetic field influences Solar luminosity by changing the effective surface emissivity of the magnetic elements. Sunspots appear dark, hence emit less energy, while faculae and network are bright compared with the surrounding photosphere, and emit more energy than the "normal" photosphere with equal surface area. Sunspots and faculae are different manifestation of slender magnetic flux tubes perpendicular to the solar surface localized near the photosphere (Observations have shown that faculae and network are composed of small magnetic flux tubes, and the term "faculae" refers to both faculae and network flux tubes in the rest of this thesis, unless otherwise specified). The reason for their radically different behavior is apparently the different size of the flux tubes. The size of the sunspots range from a few thousand km for small spots to fractions of the solar radius. The size of the faculae flux tube, however, is small. It is equal to or beyond the best spatial resolution achievable from ground based observations. The generally accepted value is about 200 km in diameter. In both cases, the strong magnetic field of the flux tubes (1 to 3 KG for sunspots, and 1.5 KG for faculae. See, e.g., McPherson, Lin, and Kuhn 1992, Solanky, Ruedi, and Livingston 1992, and Rabin 1992) prevent convective energy transport across the flux tube, but the small size of the facular flux tube makes it possible for the radiative energy transport to achieve thermal balance between the solar plasma in and outside of the flux tube. Since the lifetime of the faculae flux tube is 5 minutes and is much longer than the dynamical time

scale for the solar plasma to adjust to any pressure perturbation, magnetohydrostatic equilibrium is also achieved between the facular flux tube and the surrounding photosphere. The presence of magnetic pressure inside the facular flux tube reduces the thermal pressure. This requires a decrease of flux tube plasma density since the temperature is balanced in and outside of the tube, and results in a lower opacity inside. Thus, optical density unity is reached in a deeper layer of atmosphere inside the flux tube where the plasma temperature is higher. Thus it appears brighter than the surrounding nonmagnetic photosphere even near disk center. Near the limb, the brightness of the faculae is largely due to the "hot wall" effect. Because of the depression of the geometrical height of the layer with unit optical density inside the flux tube, we see the wall of the flux tube nearly face on when observing near the limb. Since the limb-darkening of the photosphere is a strong effect, the faculae appear with high contrast near the limb. The faculae thus act as a "leak" where the energy of the deeper atmosphere can escape more easily. However, Kuhn (1992) argued that, in a model where energy is transported by diffusion and the photon mean-free-path is decreasing exponentially, the horizontal energy transport is much more effective than the vertical energy transport. Eventually the excess flux of the facular flux tube comes from the surrounding layers. Thus this "window" effect does not lead to overall higher luminosity.

Sunspots, on the other hand, block the convective energy transport and reduce the emitted flux by as much as 75 % for a large spot. This is due to the large diameter of the flux tube which prevents radiative energy transport to from penetrating deep into the flux tube. However, magnetohydrostatic equilibrium must hold, and the presence of the strong magnetic field requires a lower thermal pressure of the plasmas. The plasma temperature inside the sunspots is thus lower. The cooler

sunspot plasma thus results in a reduced energy flux in the direction vertical to the solar surface. Where does the blocked energy go? This is still a controversial subject. Some believe that the blocked energy is re-radiated away by the accompanying faculae with a timescale comparable to the lifetime of the active regions, while others believe that the solar convection is very effective in mixing any local excess energy throughout the entire convection zone within a short timescale. Kuhn (1992) argued that photospheric magnetic fields produce anisotropic radiation fields, as is evident in the case of the faculae. Thus, the sunspot blocked energy is redirected to the direction parallel to the solar surface. He also showed some evidence of this anisotropic sunspot radiation field in the autocorrelation of the ACRIM data. In this case the sunspots do not decrease the solar luminosity on a long timescale.

The "hot wall" model of faculae described above is plausible; however, alternative explanations exist. In the "hillock" model, the excess facular brightness can be due to non-thermal heating by, e.g., acoustic wave, hydromagnetic waves, electrical current dissipation, or by systematic upflows of hot plasma from deeper layers (Vainstein, Kuklin, and Maksimov 1977 and references therein). Indeed, the "hot wall" effect alone cannot produce the observed facular contrast. For example, the calculation of Deinzer, Hensler, Schüssler, and Weisshaar (1984) cannot account for the observed high contrast value at the extreme limb, and they concluded that some heating mechanism in addition to the "hot wall" effect is needed to explain observations. Schatten, Mayr, Omidvar, and Maier (1986) described a dynamical model in which faculae are the result of systematic upflows along the facular magnetic field line. In this model, the facular flux tubes carry ionized Hydrogen from the ionization layer 2000 km below the surface upward. Thus, the material inside the facular flux tube contains more energy (the Hydrogen recombination energy) compared with the

surrounding nonmagnetic photosphere composed of neutral hydrogen. The facular flux tube thus acts as a channel within which the hotter material can be transported to the surface more easily. The hotter material results in a uplifted solar surface in the flux tubes. The heating and the geometry of the "hillock" as seen from different angle may produce the observed facular center-to-limb contrast variation.

Whatever the model of the faculae and sunspots is, they operate in the outer layer of the Sun. The limb-brightness observations of Kuhn et al showed that the observed irradiance variation is indeed solar luminosity change. Thus, the sun may modulate its energy generating rate in the core in sync with the solar cycle. Simple calculation show that the time for a photon to diffuse from the core to the surface is of the order of 10^5 years. It is then hard to imagine how something happening near the surface can have any effect on what happened in the core 10^5 years ago. Another possibility is that the solar core does not generate more energy during solar maximum. The increased surface magnetic activities simply increase the total effective emissivity, and thus increases the total luminosity during solar maximum. This scenario requires an energy reservoir for the excess energy not radiated away during solar minimum. This energy cannot be stored as magnetic energy, since most of the models of solar magnetic cycle (See, for example, the discussions in Foukal, 1990) predict that the magnetic activity is the weakest during solar minimum. The solar convection zone, with its huge heat capacity, can easily store the 10^{-3} solar luminosity not radiated away without causing any significant change in the convection zone. If this excess energy is stored purely in the form of thermal energy, then the accompanying temperature perturbation should be of the same order of magnitude, and should be an observable effect. However, we must note that the net result of the complementary effects on solar luminosity of the sunspots and faculae

are not clear yet. There are observations and models arguing that the flux excess of faculae and deficit of sunspots should balance each other (Chapman, Herzog, Lawrence, and Shelton 1986, Schatten 1985, Bruning and LaBonte 1983). If this is true, then we need some other mechanism to explain the solar cycle irradiance variations.

1.2.3 The Subsurface Magnetic Fields

We believe that the increased surface magnetic activity during solar maximum is the surface signature of a toroidal magnetic field near the base of the solar convection zone intensified by the solar differential rotation. The estimated strength of the magnetic field is of order of a few thousand gauss (Parker, 1987b). MHD theory, as discussed in Section 1.2.1, predicts that such an intense magnetic field should block convective flow. Thus, it is important to consider the effect of this intense magnetic field on the solar luminosity variation. Interestingly, its effect depends on the location of the field. If it lives in the convection zone, then its effect is to block the convective flow, thus reducing the efficiency of the convective energy transport. The solar plasma directly above these field line receives less energy from the below, thus forming a "thermal shadow". On the other hand, if these field live in the radiative zone, since the magnetohydrostatic equilibrium must be maintained in and outside the tube, the plasma density inside the magnetic flux tube must be lower, as in the case of the faculae flux tube. The "evacuated" flux tube thus has lower opacity and higher radiative transfer efficiency. The solar plasma above it will see more flux coming through, and the temperature should be higher than the plasma at the same level without a magnetic field below. Thus, if the toroidal field is responsible for the observed 11-year luminosity variations, it must exist near or below the base of the solar convection zone.

The exact location of the toroidal magnetic field is not well determined, both theoretically and observationally, however. Also, the interactions between the magnetic field and the energy transport mechanism are more complicated than the simplified picture above. Parker, in a series of papers (1987a, 1987b, 1987c), considered the dynamics of a strong and broad horizontal magnetic field in the convection zone of a star. He argued that the result of the interaction between the magnetic buoyancy of the intense horizontal magnetic field and the weight of the thermal shadow formed above the field due to the blocking of the convective flow is that the weight of the thermal shadows would overcome the magnetic buoyancy and press the magnetic field down against the bottom of the convection zone. Also, the inhibition of the convective flow results in the accumulation of heat beneath the magnetic field. This causes the gas density below the field to decline, and eventually triggers the Rayleigh-Taylor instability. The Rayleigh-Taylor instability arises between the interface of two fluids with different density in the presence of a gravitational field (Chandrasekhar 1970). Consider two vertically adjacent fluids, with the lower fluid having density ρ_1 and the upper layer with density ρ_2 , and the gravitational field is pointing downward. If $\rho_2 < \rho_1$, then the configuration is stable against perturbations, whereas it is unstable if $\rho_2 > \rho_1$. If there is surface tension then the configuration will be stabilized for perturbations with sufficiently short wavelengths. If a horizontal magnetic field is introduced, the magnetic tension of the field serves as the surface tension due to the frozen-in field approximation. Thus, the accumulation of heat beneath the magnetic field will eventually cause the hot gas to penetrate through the field to rise to the surface, carrying some of the magnetic field with it. This phenomenon is interpreted as the cause for the onset of the active regions. Parker's work provided some support to the model in which the subsurface magnetic field is the modulation mechanism, since the predicted location

of the subsurface magnetic field should increase the energy flux received by the solar plasma directly above it. The amplitude and phase of this modulation should also be in phase with the sunspot cycle, consistent with observations.

Spruit (1991) made a mixing-length calculation on the effect of the surface and subsurface magnetic field on the solar luminosity and radius variations. Two important time-scales in this calculation are the turbulent diffusive timescale τ_{tu} , and the thermal time scale of the convection zone, τ_{th} . The estimated values are $\tau_{tu} \approx 1$ yr., and $\tau_{th} \approx 10^5$ yr. An isotropic turbulent diffusivity was assumed. Because of the short turbulent diffusion timescale and the large heat capacity of the convection zone, perturbations originating from the base of the convection zone are smeared horizontally and lose their identity before reaching the surface. He concluded that, any temperature perturbations originating from layers deeper than 40000 km below the surface will have unobservable effects on the luminosity and radius, and all the observable effects result from the surface magnetic field. Thus, this calculation would rule out the subsurface magnetic field as the cause of the observed irradiance variations. However, numerical simulations of realistic convection are not consistent with Spruit's assumptions (Kuhn 1991).

1.3 This Thesis

It is clear from the above discussions that the question of how, and which solar magnetic field component is modulating the long-term solar luminosity variations is not answered by the current theoretical modeling. There is room for improvement at both theoretical and observational front. We took a step forward by constructing a specialized instrument, the Solar Photometric Telescope, to obtain precision full-disk photometric observations of the Sun. New observing techniques, along with new analysis methods were developed to achieve high photometric sensitivity.

The Solar Photometric Telescope (SPT), is designed to achieve both small and large scale photometric accuracy. We employed a cryogenically cooled CCD array to obtain better photometric accuracy. The optical system is carefully designed to minimize noise due to scattered light, internal reflection, and optical imperfection of the optical components. CCD array observations require careful calibration of the difference between the gain of each detector element, the so-called "flatfielding problem". The SPT was designed to allow us to take gain calibration data, the flatfield, with exactly the same optical setup used for taking data. This is essential to achieve the desired photometric accuracy, since the "true" gain variation includes both the pixel-to-pixel sensitivity variation of the CCD, and the optical modulation of the light beam due to optics, e.g., the dust shadows. The daytime sky was used as our "flatfield". Although it provides the best flatfield over other uniform light sources, it is the most time-consuming step of the whole observing procedure, taking up 2/3 of the observing time. This is a compromise we have to make to achieve the large scale photometric accuracy. Compared with the SPT, Nishikawa's instrument employed video CCDs operating at room temperature. He also used diffusers to make calibration observation. Our experience showed that this method of flatfielding introduced large scale error, since the insertion of diffusers changes the optical configuration of the system. This is the limiting factor of the largescale photometric accuracy of his instrument.

Although the sun radiates about 70 % of its energy in the visible part of the spectrum with wavelengths below 1μ (Foukal 1990), the infrared solar spectrum is still of particular interest to the solar astronomers. The opacity of H^- , the dominant source of absorption in the solar photosphere (Chandrasekhar and Breen 1946), is smallest at the infrared J band at 1.6μ . Thus, we have access to the deepest

observable layer of the solar photosphere at this wavelength (Vernazza, Avrett, and Loeser 1976). Although this layer is only 35 km below the layer with τ_{5000} , this is an important 35 km since the solar opacity is changing rapidly in this region. For example, some photometry showed that the faculae appear dark, not bright near disk center at 1.6μ (Foukal, Little, and Mooney 1989, Foukal, Little, Graves, Rabin, and Lynch 1990). Although this result was not confirmed by other observers, it could bear important information on the structure of the small magnetic flux tube if proved to be true. Another important property of the infrared spectrum is the height dependence of the source function, i.e., at longer wavelengths, we observe higher up in the solar atmosphere. This is due to the fact that the H^- dominates the continuum opacity for light with wavelength longer than 1.6μ . Also, the H^- is in Local Thermal Equilibrium (LTE) with the electron gas. Thus, the infrared spectrum can be used to probe the temperature structure of different layer of the solar atmosphere.

Infrared observations have numerous advantages as described above; however, imaging in this part of the spectrum has long been closed to astronomers due to the lack of adequate infrared array detectors. There were some single element infrared detectors available, but imaging with a single element detector is difficult. The long time required to scan an image limits the time resolution and data rate, and the changing sky condition and the small amount of data limit the photometric accuracy achievable. Some examples of this kind of observation can be found in Koutchmy (1978), and Worden (1975).

With recent progress in infrared array technology, large format infrared arrays became accessible to astronomers. Another new instrument, an infrared camera was built with a Rockwell TCM1000C infrared array, sensitive to light with wavelength

from 1 to 2.5 μ . It has a large format of 128×128 pixels, with a pixel size of 60 μm . The full well capacity is of order of 10^7 , and is operated at liquid Nitrogen temperature of 77 K. These properties make it an ideal instrument for solar photometric observations. To take advantage of this new instrument, we used it to obtain images of the Sun at the infrared J (1.2 μ), H (1.6 μ), and K (2.2 μ) band. The infrared data presented in this thesis were obtained at the National Solar Observatory at Sacramento Peak, New Mexico. This observatory, at 3200 meters above the sea level, is ideal for infrared observations since it is above most of the water vapor in the earth's atmosphere which is responsible for most of the atmospheric absorption of the infrared light (Jackson, 1985).

One of the new analysis techniques developed is an algorithm to calculate the flatfield of an array detector with only a set of shifted data frames. This technique is indispensable when good flatfields are not easily available, like the infrared observations where sky brightness is fractionally lower than in the visible. New algorithms for finding the coordinates of the solar disk center, averaging images, and constructing the contrast image of the averaged solar images were also developed. These will be presented in Chapter 3.

1.4 Related Subjects

The solar cycle irradiance variation is not the only subject that can be studied with new high accuracy photometric observations. For example, the energy balance between sunspot and faculae, the facular and network contrast, and the thermal signature of large scale solar convection like supergranulation and giant cells are interesting subjects that can be studied.

The photospheric network is known to outline the supergranulation seen in photospheric velocity maps and the photospheric magnetic network (Frazier 1970,

Muller 1983). High resolution observations show that it consists of isolated bright points, with contrast of 1.2 to 1.4, and sizes of $0.2''$, imbedded in intergranular lanes, and was considered to be the same as the facular bright points (Muller and Keil 1983, and references therein). The observation of Nishikawa and Hirayama (1990), which showed that the center-to-limb variation of the facular two-color contrast in the quiet network and active region are the same, supported this finding, but different views exist.

The center-to-limb variation of the contrast bears the information of the vertical structure of the small magnetic flux tube considered to be the basic constituent of network and faculae. However, no reliable photometric measurement of the network contrast in the continuum is available up to date, due to its smallness. Becker (1968) obtained $\approx 0.3\%$ contrast with broad band continuum images centered at 4850 \AA . Frazier (1970) found 1% contrast at 4850 \AA . Liu (1974) used time-averaging techniques on white light images to obtain images of the network near disk center, but the contrast was not measured. Infrared observations (Worden 1975) at 1.6μ showed temperature structure weakly correlated with chromospheric network, but the author reported a huge temperature difference of 500 K. Other monochromatic studies found 0.29% at 5265 \AA (Skumanich, Cmythe, and Frazier 1975), 0.1% at 5256 \AA (Foukal and Fowler 1984).

Since the network is found both in the active and quiet sun regions, it will be instructive to study the differences of the characteristics in these two regions. This study should yield information on how the network is formed, and its relation to the supergranulation.

Faculae, when observed in continuum wavelengths with low to medium spatial resolution, appear as extended bright patches in the active regions near solar limb.

They are almost invisible near disk center. As pointed out earlier, the Facular Bright Points are considered by some to be identical to the Network Bright Points, but it is not proved, or disapproved observationally. The major difference between faculae and network has been the spatial appearance of the two components. It is an important component to the solar irradiance since it is the brightest feature observable in a continuum image. Nevertheless, the spatial distribution, as well as the center-to-limb variation of contrast, are still not well determined. The CLV of facular contrast has been measured in different region of μ , in a wide range of wavelengths (e.g., Lawrence, Chapmann, and Herzog 1988, Lawrence 1988, Hirayama, Hamana, and Mizogaki 1985, Libbrecht and Kuhn 1986, Wang and Zirin 1987, and Nishikawa and Hirayama 1990). Most of these results showed that the facular contrast near disk center is vanishingly small, except the result of Foukal and Fowler which showed negative contrast at 1.6μ near disk center. The generally adopted value today is zero. Near the limb, there is better agreement between observations. However, at the extreme limb ($\mu \leq 0.2$) Libbrecht and Kuhn found that the faculae contrast peaked near the limb and falls off outward, while Wang and Zirin found that it continues to rise toward the limb.

The interesting question is, is FBP the same as the NBP? If not, what's the difference between the two? If yes, then what is the mechanism that distributes the NBP in a network-like structure. What is the vertical structure of the facular magnetic flux tube? There is a lot of work to be done to answer all these questions, and an accurate measurement of the contrast, and contrast center-to-limb variations will certainly provide us valuable information toward the resolutions of these problems.

This thesis reports on our effort to try to answer the questions we have raised

so far. We will start by describing the instrument in details in Chapter 2. The observation and data reduction procedures are discussed in Chapter 3. Results and interpretations of the observations of photospheric network and faculae contrast are given in Chapter 4. Chapter 5 discusses subjects related to the total solar irradiance variation, and summarizes the whole work.

CHAPTER 2

INSTRUMENTATION

2.1 General Considerations

The goal of this research is to detect the brightness variations that are causing the long-term solar irradiance changes. The limb brightness measurement provides a good guideline for the instrumental precision required. The observed brightness excess in the active latitudes range from about almost zero during solar minimum to about 7 K near solar maximum. Thus it is desirable to have a 1 K sensitivity to monitor the yearly change of the photospheric temperature. The sensitivity required to resolve a temperature variation of amplitude δT from a blackbody at temperature T at wavelength λ is

$$\frac{\delta I}{I} = \frac{-\frac{hc}{\lambda k T}}{\exp(-\frac{hc}{\lambda k T}) - 1} \frac{\delta T}{T} \quad (2-1)$$

where k is the Boltzmann constant, h is the Planck constant, and c is the speed of light. At the red band pass of $\lambda = 6,500 \text{ \AA}$, $\frac{\delta I}{I} = 6.5 \times 10^{-4}$ for $\delta T = 1 \text{ K}$, and $T = 6,000 \text{ K}$. In the infrared at $\lambda = 16,000 \text{ \AA}$, $\frac{\delta I}{I} = 3.3 \times 10^{-4}$ for the same magnitude temperature variation. The full well capacity of the Texas Instrument CCD used for this observation is 65,000 photons. The photon noise per pixel per exposure is 260 photons. Thus, the fractional noise is 4×10^{-3} , approximately the sensitivity desired. The full well capacity of the infrared array is about 50 times

that of the Texas Instrument CCD, hence the photon noise is not the limiting factor. However, there are other sources of error, e.g., scattered light, and flatfielding error. Thus, it is necessary to average a large number of images to minimize these errors.

Another important factor for the success of this observation is the flatfielding problem. Flatfielding is necessary for any array detector observation. Conventional flatfielding techniques use either "dome flat", or "diffuser flat". Our experience with these methods showed that they are good only to 10^{-2} level on the large scale. The 'true flatfield' should measure both the pixel-to-pixel gain variations of the detector and the 'gain' variations due to optical imperfections, like dust shadows. When a diffuser is used, or when the telescope is turned to the dome, the illumination pattern of the system is changed, hence the optical configurations used to register the data is different from that used to register the flatfields. Thus, the diffuser and dome flatfields usually produce some large scale flatfielding error. The best flatfield available for daytime observations is the sky. The sky is virtually flat, except for a small linear gradient. The measured amplitude of this linear gradient is approximately 10^{-5} /pixel, when looking at 30 degrees away from the sun. This can be fit for and removed a posteriori. The disadvantage of using the sky for flatfielding is that the sky brightness is approximately 10^{-5} to 10^{-6} that of the sun, hence the exposure time to obtain a skyflat would be 10^5 times longer.

The brightness of the infrared sky is lower than in the visible, due to the wavelength dependence of the scattering cross-section of photons scattering off air molecules. Thus, using sky as flatfield for infrared observation requires very long integration and becomes unpractical. We developed an iterating algorithm which can calculate the flatfield of an imaging array with a set of shifted data frame. This algorithm is used to calibrate the infrared data. This algorithm was tested for

nighttime star cluster observation with the MSU 24" telescope, and for the visible wavelengths full disk solar observation on the SPT. The flatfielding quality was found to be comparable to the skyflats in the visible data.

The above considerations call for a system with low scattered light, and high data rate. It also requires a 10^6 dynamical range of exposure time. The Solar Photometric Telescope was designed to meet these criteria. The following paragraphs describe the system in details.

2.2 The Solar Photometric Telescope

Figure 2.1 shows the system diagram of the SPT. Figure 2.2 and Figure 2.3 are pictures of the SPT. The heliostat was mounted on a heavy steel platform sitting on the roof of the Michigan State University Observatory. It consists of a 15 cm primary quartz mirror mounted on a Meade 8" telescope drive, and a 6 cm secondary mirror reflects sunlight down through a hole in the roof to the imaging optics. All the imaging optics and the CCD camera were mounted on a bracket attached to the heliostat platform. A fast shutter assembly, consists of a electromechanical leaf shutter and a rotating wheel shutter is mounted on a vertical bench, isolated from the imaging optics. The imaging system is enclosed in a light-tight box, and well baffled with tubes inside the box. An IBM-compatible computer is used to control the shutters, the heliostat, and the CCD camera. Images are stored on magnetic tape for later analysis. The CCD was upgraded from the Texas Instrument 384×594 array to a Ford Aerospace Inc. 1024×1024 array during the winter of 1991. The imaging optics, as well as the computer control and data storage system were modified consequently to take advantage of the higher spatial resolution offered by the new CCD.

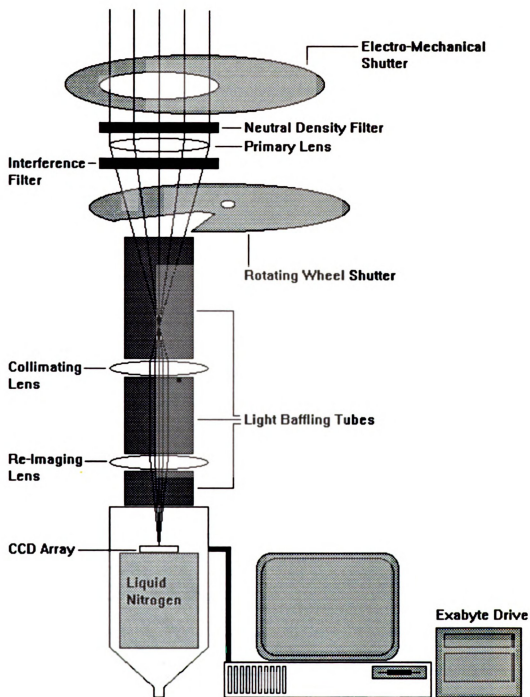


Figure 2.1 System Block Diagram of the Solar Photometric Telescope.

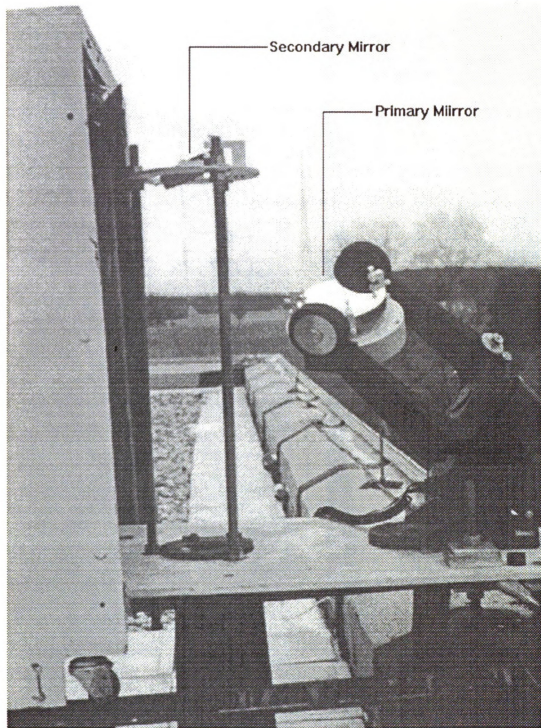


Figure 2.2 The Heliostat of the SPT.

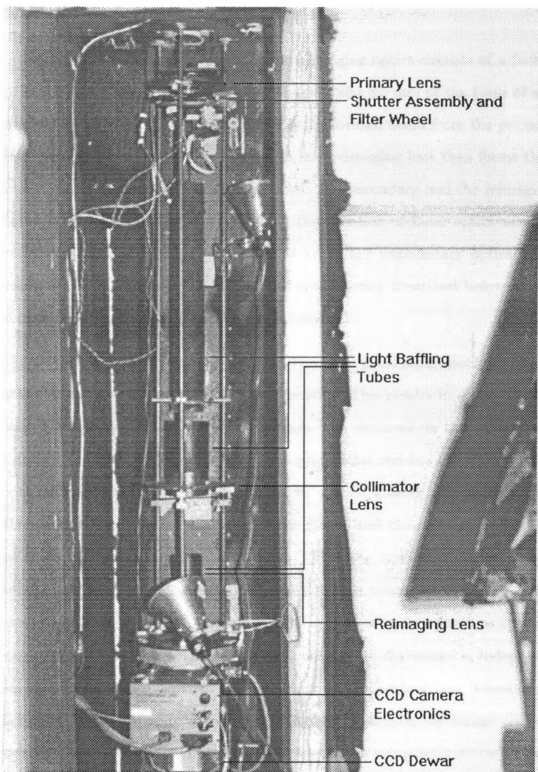
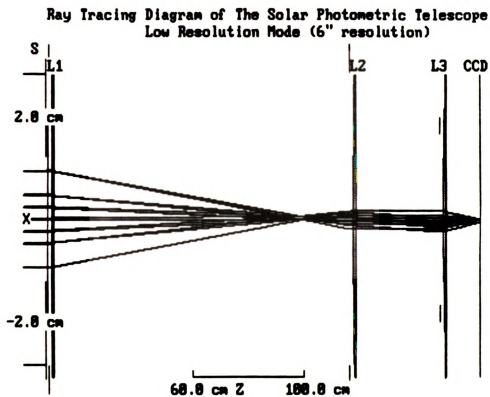


Figure 2.3 The Optical System of the SPT.

2.2.1 Optical System

In the first phase of the operation, the imaging optics consists of a $f=900$ mm primary lens, forming a full-disk solar image of size 8.3 mm at the focus of a $f=166$ mm secondary lens. This secondary turns the focused beam from the primary lens into parallel beam again. A third $f=135$ mm reimaging lens then forms the solar image on the CCD with a size of 270 pixel. The secondary and the reimaging lens combination works as an optical relay. The addition of these optics may appear redundant, and ideally, we would like to avoid any unnecessary optics to reduce scattered light. But the benefits of the optical relay described below more than compensate its drawback, and its use is justifiable.

The diameter of the primary lens is 60 mm. To avoid saturation problem, it was stopped down to 25.4 mm by an aperture stop. This results in a very slow beam, with $f/D=35.4$. A slow beam forms sharp dust shadows on the CCD. They are difficult to calibrate by flatfielding. The optical relay reduces the f/D ratio to 28.8, and makes it easier to calibrate the effects of dust shadow. To avoid vignetting, the neutral density filter, the interference filters, and the shutters were all placed as close to the primary lens as possible. This also minimizes the effect of filter inhomogeneities. But focusing with primary lens becomes impossible, since the components are so close to each other. The optical relay thus provides a convenient way to focus the image. Since the final position of the image is independent of the relative distance between the secondary and reimaging lens, focusing can be achieved simply by adjusting the secondary to focus it on the image plane of the primary lens. The optical design was checked with a computer ray-tracing program to ensure that the system is free of vignetting problem. Figure 2.4 shows the ray-tracing diagram of the optical system.



LAYOUT: Annotate CirMenu Zaxis Hdim Udim Posn Magn Random ElAz Quads ESC

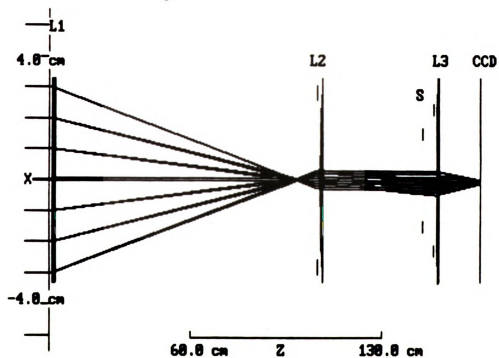
Figure 2.4 Ray-Tracing Diagram of the Solar Photometric Telescope in Low Resolution Mode.

With the installation of the 1024^2 array, the image size increases to 350 pixel due to the smaller pixel size of the new array. To take advantage of the larger format of this array, the secondary and reimaging lenses were replaced by lenses with $f=81$ mm and $f=160$ mm, respectively. The new image size is 886 pixel, or $2.16''/\text{pixel}$. This is well below the diffraction limit of $6.5''$ of a 25.4 mm telescope at $6,500 \text{ \AA}$. To achieve $2''/\text{pixel}$ resolution, the aperture stop of the primary lens is removed to yield a resolution of $2.09''$ at $5,000 \text{ \AA}$ and $2.72''$ at $6,500 \text{ \AA}$. This resolution is barely enough for the green wavelength, but not enough for the red. Since experiences from nighttime observations showed that the seeing of our site is typically $3''$, we decided to go ahead with the $D=60$ mm primary lens. Since the aperture size of the shutter and the interference filters were only 25.4 mm and 50.8 mm, respectively, they have to be increased to avoid vignetting. An alternative is to place them between the secondary and reimaging lens, where the beam size is small. The later is adopted since it does not require the acquisition of new filters and shutter. The f/D ratio of this configuration is 29.6, not significantly different from the old configuration. Figure 2.5 shows the ray tracing diagram of this setup.

2.2.2 The Shutter Assembly

The shutter assembly consists of an electromechanical leaf shutter and a rotating wheel shutter. Figure 2.6 shows a picture of the shutter assembly. The leaf shutter has an aperture of 25.4 mm. The fastest speed is about 5.5 msec. With the initial setup with a $D=3$ neutral density filter, this exposure time still leads to saturation when taking solar images. Also, an integration time of 5×10^5 longer for taking the skyflat is 45 minute. This is far from acceptable. We achieved a faster shutter speed by synchronizing the leaf shutter with the shutter wheel, running at 40 revolution per second (RPS) speed. The shutter wheel is a copper disk with

Ray Tracing Diagram of the Solar Photometric Telescope
High Resolution Mode (2" resolution)



LAYOUT: Annotate CirMenu Zaxis Hdim Vdim Posn Magn Random ElAz Quads ESC

Figure 2.5 Ray-tracing Diagram of the Solar Photometric Telescope in High Resolution Mode.

two 36 degree wedge cutoff, spaced 180 degree apart. One of the cutoff is masked by tape, allowing only one exposure for each revolution. The symmetrical cutoff is necessary to balance the wheel. The shutter is driven by a DC motor, equipped with an optical encoder. The optical encoder generates an index pulse for each revolution. The shutter wheel is aligned with the optical encoder such that when the index pulse is on, the shutter wheel cutoff is aligned with the optical axis, allowing the light from the Heliostat to pass through. Thus, when taking exposure, the control computer detects the index pulse, delays for 1/4 of the revolution, then opens the leaf shutter. On the second index pulse, the control computer delays for another 1/4 revolution, then closes the leaf shutter. The fastest speed this shutter assembly achieved was 2 msec., limited by the maximum speed of the DC motor. When taking skyflats, the shutter wheel can be parked at the open position by the computer, and the integration time is controlled by the leaf shutter. The minimum shutter speed is limited only by the number of register of the counter, which is 2^{14} second. The large range of possible integration time of this shutter system thus allow us to take both the solar images and the skyflats with exactly the same optical setup. This is critical to achieve high photometric sensitivity.

2.2.3 The Computer Control and Data Acquisition System

The first control computer used was a IBM PC-AT computer. It controls the shutter wheel speed through a D/A controller. A bidirectional parallel port is used to control the leaf shutter, the heliostat motion, and is used to monitor the status of the wheel shutter. The first mass storage system used was a 9-track tape drive. The CCD camera system is manufactured by Photometrics Inc., and is also controlled by the computer. An observing program, written with fortran and assembly language, integrates the operation of the subsystems. The upgrade to the Ford 1024² array

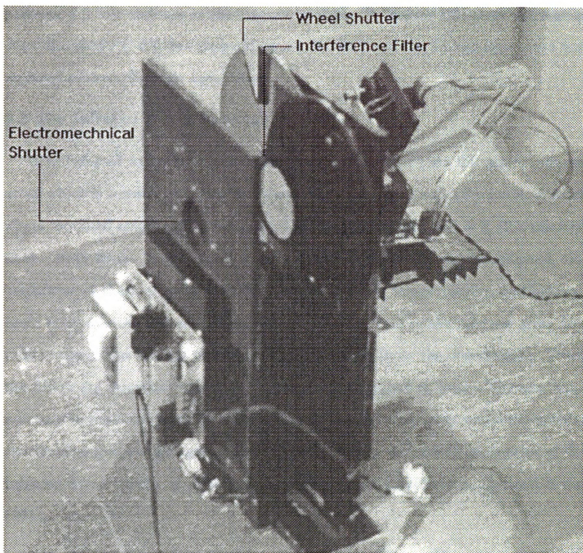


Figure 2.6 The Shutter Assembly and the Filter Wheel.

presents a 5 fold increase in the amount of data. To handle this large amount of data, the IBM PC-AT was replaced with a 386 PC, and the 9-track tape drive was replaced with an Exabyte tape drive.

2.3 The Infrared Array Detector

The Infrared Array system is a Rockwell TCM1000C 128×128 pixels infrared array which is sensitive to light with wavelength between 1 and 2.5 micron. A filter wheel mounted inside the dewar carried an H (1.6 micron) and a K (2.2 micron) filter. Both filters have a band pass of 0.2 micron FWHM. In the infrared, the brightness of thermal radiation from objects at room temperature sometimes exceeds faint celestial sources. Thus, a warm filter in front of the infrared array will radiate significant amount of infrared light to contaminate the observations. Thus, the filters are mounted inside the dewar and maintained at liquid Nitrogen temperature to minimize their thermal emission. The infrared array was electronically shuttered so that no mechanical shutter was necessary. A detailed description of the Infrared Array System is presented in another paper (McPherson, Lin, and Kuhn 1991).

The infrared data were obtained at the National Solar Observatory at Sacramento Peak, New Mexico, with the 6" celostat in the Evans Facilities, and with the Vacuum Tower Telescope (VTT). To obtain spatial resolution comparable to the SPT, we used a $f=600$ mm lens to form a 200 pixels diameter partial solar image on the infrared array. Neutral density filters were used to reduce the amount of light. Like the visible wavelengths observations, scattered light variation is the most important source of error. Since we don't have a permanent blackbox setup, we tried to minimize the scattered light by covering and baffling the infrared system with black felt and tubes. Although the covering and baffling is simple and maybe,

well, ugly, it served its purpose well. Figure 2.7 shows the experimental setup for the infrared observation.

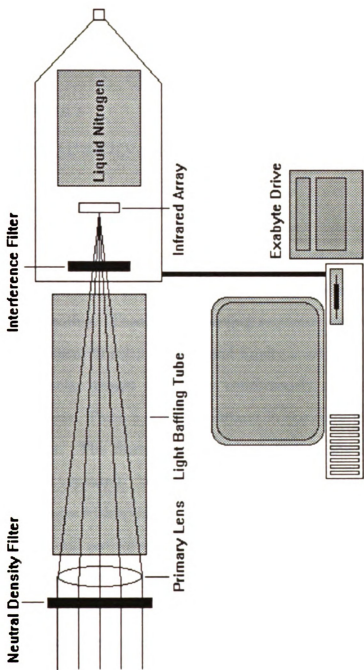


Figure 2.7 Experimental Setup for the Infrared Observations.

CHAPTER 3

THE OBSERVATIONS AND DATA REDUCTION

3.1 Observing Procedure

A complete set of imaging array data must include dark frames, flatfields, and the data frames. For the visible wavelength observations, the skyflats were used for flatfielding. Thus, the observing sequence usually starts with a set of 5 dark frames, then 20 solar images, and finally a set of five 4-minute exposure skyflats. The 20 solar images were taken continuously, and take approximately 10 minutes to complete. Thus, a complete dataset in one color takes approximately 45 minutes to collect. The filters were then switched to the next color, and the observing sequence repeated. We call a set of data with both colors a time step, since the solar images within this set will be averaged to make two time-averaged solar images in green and red wavelength. Occasionally, the sky clouded up during observation and skyflats were inaccessible. Except when the sky is completely overcasted, a set of 10 shifted solar images would be collected to use the iterating algorithm to calculate the flatfield. Since the incident angle of the light beam changes as the heliostat traces the sun across the sky, the dust shadow pattern on the CCD changes also. Thus, frequent flatfield observations are necessary.

The iterating algorithm was the primary calibrating method for the infrared observations, and because the array covers only part of the solar disk, a data set in one color consists of dark measurements, and then a series of shifted images to

cover the full solar disk. Diffuser flats were also obtained for initial flatfielding for the iterating algorithm.

3.2 The Visible Wavelength Data

The construction of the SPT was completed in the summer of 1990. It collected 5 days' data during that summer; however, only 3 days' data lasted more than four hours. The SPT was dismantled for roof work and the CCD camera upgraded with a 1024×1024 CCD in the following fall and winter. The SPT resumed operation the next summer, and obtained 9 days' data. Figure 3.1 shows a raw full disk solar image obtained with the SPT in the green bandpass. Table 1 summarizes the data set of the visible wavelengths. The length of the data set varies from a single time step to 4 time steps which last 6 hours depending on weather condition.

Table 1. Summary of Visible Wavelength Observations

Date	Red (6,500 Å)	Green (5,000 Å)
July 4, 1990	1 time step*	1 time step
Aug 4, 1990	3 time steps	3 time steps
Aug 14, 1990	3 time steps	3 time steps
June 4, 1991	1 time step	No data
June 5, 1991	3 time steps	1 time step
June 6, 1991	2 time steps	2 time steps
June 8, 1991	2 time steps	2 time steps
Sept 6, 1991	3 time steps	No data
Sept 21, 1991	3 time steps	3 time steps
Sept 28, 1991	4 time steps	4 time steps
Sept 29, 1991	2 time steps	2 time steps

*Each time step consists of 20 solar images.

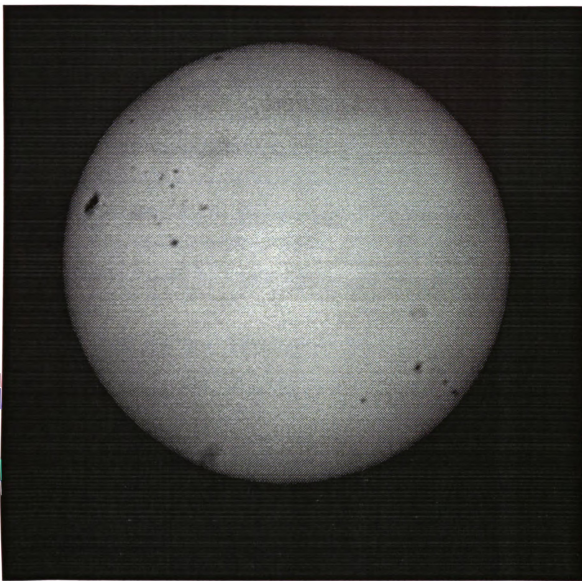


Figure 3.1 Raw Solar Image in the Green Bandpass. This image is obtained on June 4th, 1991. Image size is 448×448 pixels, and the solar radius is 170 pixels. A large sunspot near the limb, as well as several small sunspot groups appear as sharp dark spots are visible. Also visible are shadows of dust particles on the CCD window which appear as fuzzy large dark spots. Solar north is oriented approximately 135 degree counterclockwise to the $+\hat{y}$ direction.

3.3 The Infrared Data

The infrared data were obtained at NSO at Sacramento Peak during the Fall of 1990, and February of 1992. The 6" celostat of Evans Facility was used for the 1990 observations, and the Vacuum Tower Telescope (VTT) was used for the 1992 observations. Only 10 images in both H and K band were obtained in the 1990 observation. Nevertheless, this was enough to resolve the low contrast photospheric network. Several series of scans across the solar disk consisting of 100 images in J and H band were obtained for the 1992 observations. Figure 3.2 shows a typical raw image in the H band. Table 2 summarizes the Infrared dataset.

Table 2. Summary of Infrared Wavelength Observations

Date	J band (1.2μ)	H band (1.6μ)	K band (2.2μ)
Oct. 12, 1990	No data	10 images	10 images
Feb. 25, 1992	2 time steps*	1 time step	No data
Feb. 26, 1992	1 time step	2 time steps	No data

* Each time step is a 100 images scan covering the full disk.

3.4 Data Reduction

The data reduction starts with the standard procedure of dark subtraction and flatfielding. Figure 3.3 and 3.4 show two typical flatfields in the green and H band, respectively. The solar disk centers were then found and recorded. The flatfielded solar images within a time step can now be rotated, and shifted to correct for the image rotation and shift due to the heliostat. These images were then rescaled and averaged, and the fractional residual, or contrast, of the averaged solar image can be constructed. Figure 3.5 and Figure 3.6 show two flatfielded, time-averaged images in the green and H band. Figure 3.7 to Figure 3.11 show the contrast images of the

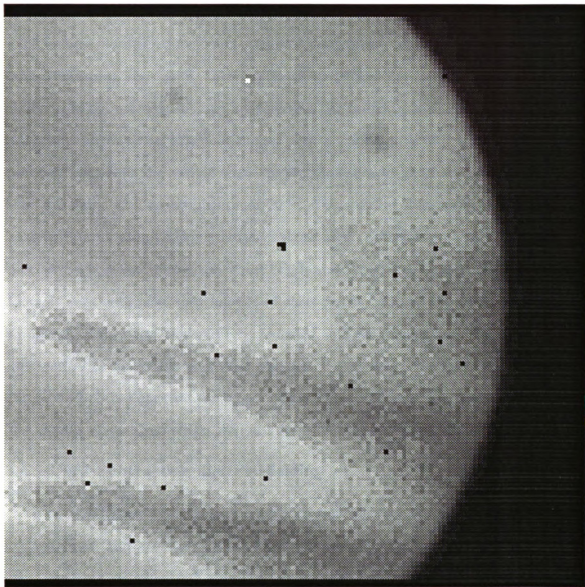


Figure 3.2 Raw Solar Image in the Infrared H Band. This image is obtained on February 12th, 1990. Image size is 130×132 pixels, and the solar radius is 100 pixels. The two fuzzy dark spots on the upper half of the image are dust shadows. The finger-like dark strips on the lower half of the image are due to large pixel-to-pixel gain variations.

five wavelengths. Since the contrast images are constructed with the time-averaged solar images, contributions from temporal brightness structures, like the 5-minute solar oscillation, are small. Low contrast structures can now be examined more easily from these contrast images. However, the imaging optics of the SPT distort the solar images to an elliptical shape, with an oblateness of 7×10^{-3} . Thus, the contrast images in the visible wavelengths showed a large second harmonics term near the limb, with an amplitude of 10^{-2} . This can be seen easily in the contrast images. Examination of this brightness structure in different time steps showed that they have a constant phase, i.e., these brightness structures do not rotate with time. Thus, it is evident that they are not of solar origin, but are due to the optics. The amplitude of the distortion can be calculated, and the images corrected before being averaged. The distortion corrected contrast of the image of Figure 3.8 is shown in Figure 3.12. It is clear that the large optical distortion error is significantly reduced. The details of each reduction step are described in the following paragraphs.

3.4.1 Dark Subtraction and Flatfielding

The dark frames and flatfields from each time step are averaged first to make an average dark, and average flatfield for each time step. In the case that no skyflats were available, or when reducing the infrared data, the iterating algorithm is used to calculate an iterated flatfield for that time step.

The principle of the iterating algorithm can be understood by observing a simple experiment in which 2 array detector images are obtained with the 2nd displaced with respect to the first image by 1 pixel in the horizontal direction. Assuming that the source flux is constant in time, then each horizontal pair of pixel between the 2 images are illuminated by the same flux. Thus we can obtain the ratio of the gain between every neighboring pixel in the horizontal direction. The same experiment

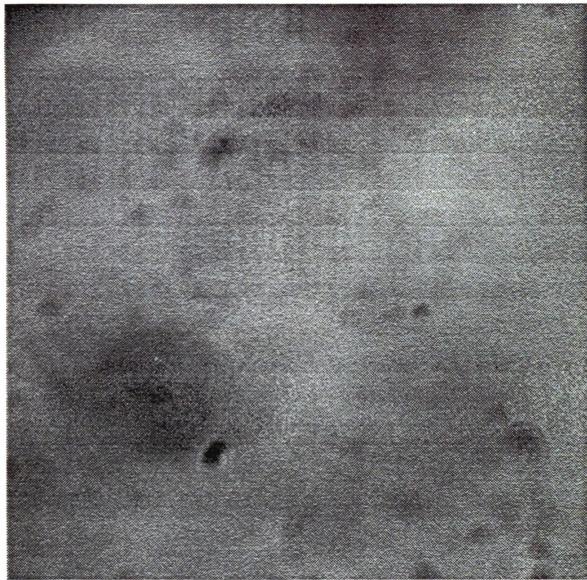


Figure 3.3 Green Bandpass Flatfield. An average skyflat obtained by summing over 5 skyflats each with 4-minute integration time. The position of the sky is 30 degrees east to the Sun. The flatfield is normalized by the average intensity of the image. Display range is 0.9 to 1.1.

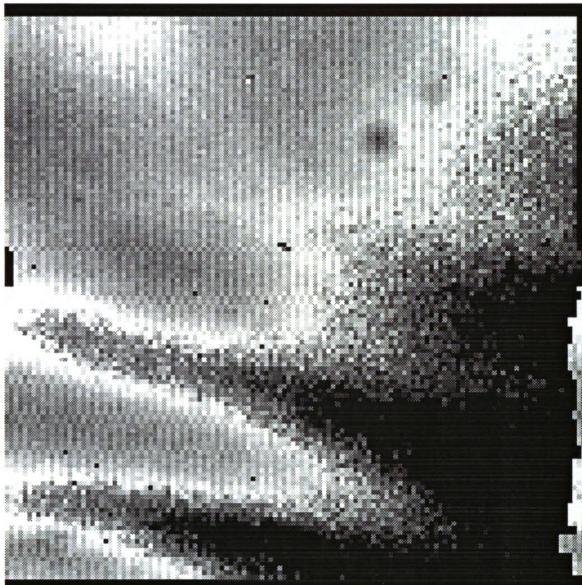


Figure 3.4 Infrared H Band Flatfield. This Flatfield was obtained with the Gain-Iterating Algorithm developed by Kuhn, Lin, and Lorz (1991). Ten partial-disk images like the one in Figure 3.2 are used for the calculation. The iteration were carried to the 10th step. The Infrared array has a large pixel-to-pixel gain variation (50 %). Display range was 0.9 to 1.1

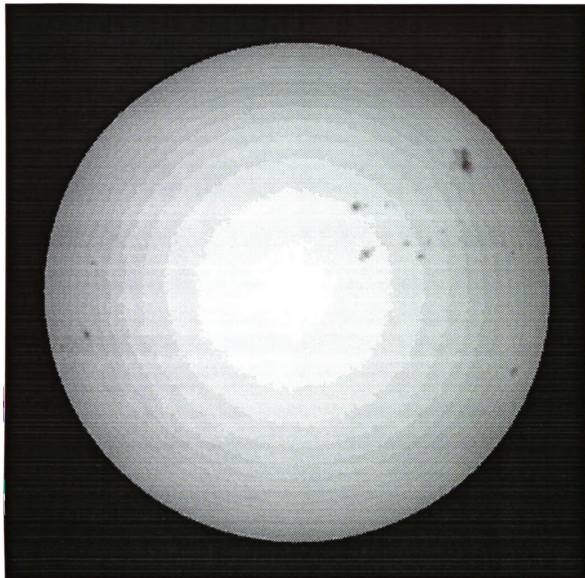


Figure 3.5 Green Time-Averaged Solar Image. This image is obtained by summing over 20 solar images, like the one in Figure 3.1, after dark-subtraction and flatfield calibration. It is clear that the dust shadows in Figure 3.1 were well calibrated. Only a 400×400 pixels subimage is displayed, with the Sun centered in the image. Solar north is oriented in the y direction, and west is to the right of the image.

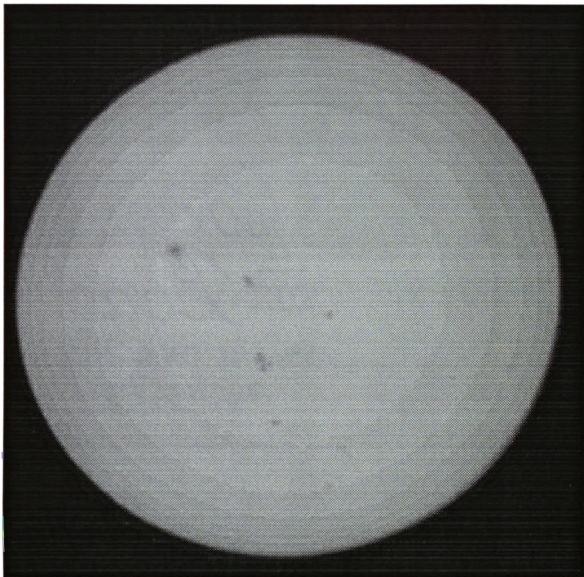


Figure 3.6 H Band Time-Averaged Solar Image. This image is constructed by summing over 100 partial-disk images of a scan obtained in February 26th, 1992. The radius of the Solar disk is 126 pixels.

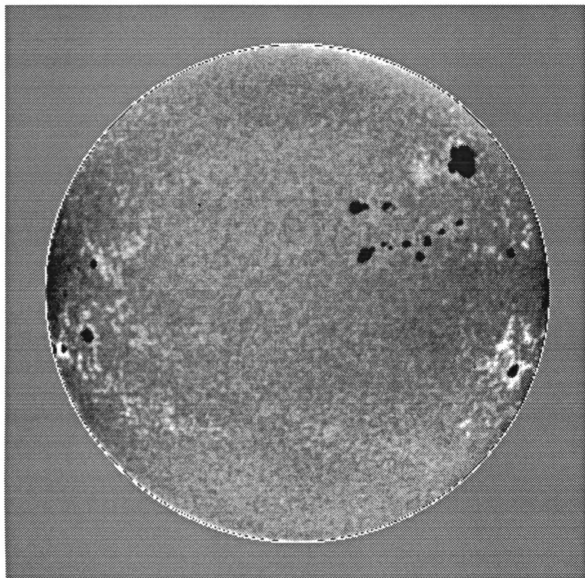


Figure 3.7 Time-Averaged Residual Image in the Green Bandpass Before Distortion Correction. The two dark patches at the top and bottom of the image are due to optical distortion. Display range is -0.02 to 0.02.

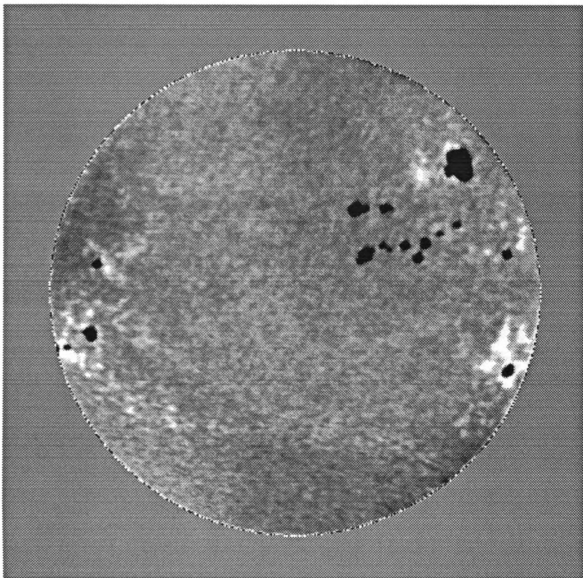


Figure 3.8 Time-Averaged Residual Image in the Green Bandpass. Optics distortion were corrected. The amplitude of the large-scale error are reduced compared with Figure 3.6. Display range is -0.02 to 0.02.

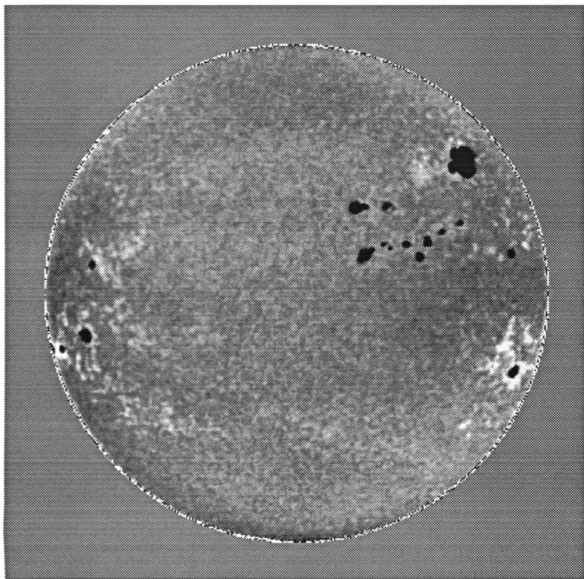


Figure 3.9 Time-Averaged Residual Image in the Red Bandpass. Optics distortion were corrected. Display range is -0.02 to 0.02.

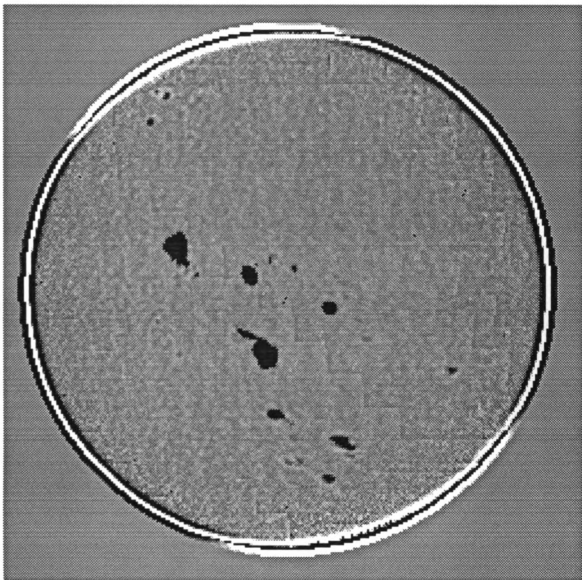


Figure 3.10 Time-Averaged Residual Image in the Infrared J Band. This is a residual contrast image of one of the scan obtain in January 26th, 1992. The image was filtered by a band-pass filter to remove large-scale error due to the error in adjusting the average intensities from image to image, as well as high frequency noise. Display range is -0.02 to 0.02.

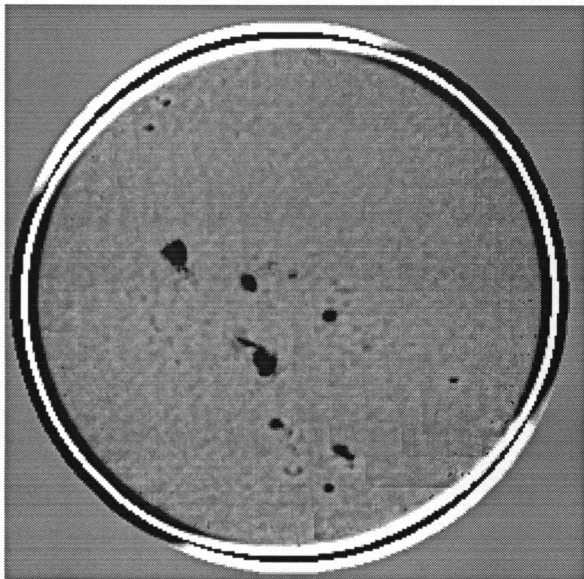


Figure 3.11 Time-Averaged Residual Image in the Infrared H Band. This is a residual contrast image of one of the scan obtain in January 26th, 1992. The image was filtered by a band-pass filter to remove large-scale error due to the error in adjusting the average intensities from image to image, as well as high frequency noise. Display range is -0.02 to 0.02.

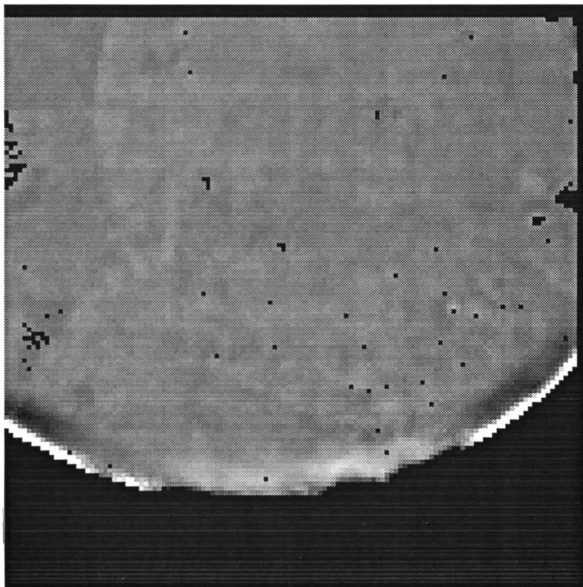


Figure 3.12 Residual Image in the Infrared K Band. This is the residual image of a single exposure obtained on Oct. 12th, 1990. The arch structures are error introduced by the iterated flat-fielding algorithm. The amplitude of this error is $\approx 1 \times 10^{-3}$, and can be reduced by averaging more images. The averaged residual images in Figure 3.10 and Figure 3.11 didn't show such error. The display range is -0.02 to 0.02.

can be repeated in the vertical direction, and the gain function of the array detector can be determined up to a scaling constant. However, in practice, it is impossible to shift the image by exactly one pixel, nor is the source flux constant in time. Nevertheless, this method can be repeated with different shifts and a least-square algorithm can be formulated to solve for the gain function $g(\vec{x})$. The full discussion of this algorithm was published in Kuhn, Lin, and Loranz (1991). Here, only the result is given.

The r th iteration of the logarithm of the gain function, $G(\mathbf{x})$, is given by

$$G^{r+1}(\mathbf{x}) = K(\mathbf{x}) + \frac{1}{n(\mathbf{x})} \sum_{i < j} [G^r(\mathbf{x} - \mathbf{a}_i + \mathbf{a}_j) + G^r(\mathbf{x} - \mathbf{a}_j + \mathbf{a}_i)] \quad (3-1)$$

with

$$K(\mathbf{x}) = \frac{1}{n(\mathbf{x})} \sum_{i < j} [D_i(\mathbf{x}) - D_j(\mathbf{x} - \mathbf{a}_i + \mathbf{a}_j)] + [D_j(\mathbf{x}) - D_i(\mathbf{x} - \mathbf{a}_j + \mathbf{a}_i)]$$

where the index r is the number of iteration, index i and j is the exposure indices, \mathbf{a}_i are the displacement of the i th exposure, and $D(\mathbf{x})$ are the logarithm of the data frames. Note that the term $K(\mathbf{x})$ is a constant and depends on the data frames only.

This algorithm was found to converge reasonably fast. The variance between successive iteration decreases like a power law of the iteration count r . 10 iterations is usually enough to reduce the variance to 10^{-4} , and takes approximately 20 minutes on a DecStation 3100 computer with $10\ 400 \times 400$ data frames. The iterated gain was found to be as good as the skyflats.

3.4.2 Calibration of Solar Disk Center

The alignment of the heliostat was less than perfect, and it produces an image motion of approximately $2''/\text{min}$. Also, images from a heliostat rotate with $360^\circ/\text{day}$ rate. Thus, the position of the disk center of each solar image is needed for rotation correction and averaging. The disk center position is found by a two-step algorithm. The first step calculates the center-of-mass of the solar disk, using the average intensity of the full image as a threshold, i.e., all the pixels with intensity higher than the average intensity are considered inside the solar disk. This method is subject to error caused by the sky gradient, the presence of sunspots, and any bright pixels outside the solar disk. Depending on the number of sunspots and bad pixels, and the amplitudes of the linear gradient, the centering error ranged from a few tenths of a pixel typically to as much as 3 pixels when the image is degraded by, e.g., passing cloud or high cirrus. No iterative process was applied to this method.

The second step uses a least-square-minimization algorithm. Since the measured oblateness of the sun is of the order of 10^{-5} (Dicke and Goldenberg 1967), we can assume that the sun is symmetrical about its center, and can be described by a radially symmetrical function $I(r)$, where r is the position vector in the disk center coordinates system. Since the sky is used for flatfielding, the linear gradient in the skyflats breaks this symmetry, and the image now is described by

$$S(x, y) = I(r)(1 + \alpha x + \beta y) \quad (3 - 2)$$

We can find the functional form of the image within any coordinate system with origin at (x'_c, y'_c) , by a transformation of the form

$$S'(x', y') = S(x - \Delta x, y - \Delta y) \quad (3-3)$$

where Δx and Δy are the relative shift between the two coordinate systems. The transformation is complicated in general, however, if $\Delta x, \Delta y, \alpha$, and β are small, we can perform the transformation with a first order expansion of $\Delta x, \Delta y, \alpha$, and β . The sky gradient is of the order of 10^{-5} per pixel at 30° away from the sun. The error in the disk center position obtained with the center of mass method is small, hence, the linear expansion is a good approximation. Thus, we can formulate a least square fitting algorithm to fit an observed image with the function of equation (3-3) to the parameters $\Delta x, \Delta y, \alpha$, and β . ($\Delta x, \Delta y$) thus give the deviation of the center-of-mass center from the true disk center, and (α, β) give the sky gradient, and can be removed. The detailed formulation of the algorithm is included in Appendix C. Test with fake solar images showed that it achieved a precision at the order of 10^{-3} pixel.

3.4.3 Image Shift and Rotation

The solar images were constantly moving and rotating, due to the missalignment and the optical nature of the heliostat. If the shift between two images is an integral number of pixel, then these two images can be summed without any degradation to the spatial resolution. However, summing images with fractional pixel shift does degrade the spatial resolution. Image rotation produces shift proportional to the radius which, when summing, also degrades spatial resolution of pixels near the limb. Thus, the solar images were shifted to the nearest grid point, and rotated to have the same orientation before averaging. The shift and rotation can be described by a transformation of the form

$$I'(\vec{\mathbf{r}}) = I(\vec{\mathbf{r}}') \quad (3-4)$$

where $I(\vec{\mathbf{r}})$ is the intensity of the image at coordinates $\vec{\mathbf{r}}$. The coordinate transformation is

$$\vec{\mathbf{r}}' = \mathbf{R} \cdot \vec{\mathbf{r}} + \mathbf{T} \quad (3-5)$$

where \mathbf{R} is a 2×2 rotational matrix,

$$\mathbf{R} = \begin{pmatrix} \cos\theta & \sin\theta \\ -\sin\theta & \cos\theta \end{pmatrix} \quad (3-6)$$

where θ is the angle of rotation, and $\mathbf{T} = (dx, dy)$ is the translation vector. Since we don't have infinite resolution, $I(\vec{\mathbf{r}})$ is really the integration of the function I within the area of the pixel at $\vec{\mathbf{r}}$. The new function $I'(\vec{\mathbf{r}})$ thus must be interpolated from the neighboring pixels of $\vec{\mathbf{r}}'$. A second order Taylor series is used for the interpolation. The error introduced by the interpolation is thus of the order of the third order derivative of the image function. This is usually negligible except for pixels near sunspots and at the extreme limb.

3.4.4 Image Distortion Correction

The optics distort the solar images to an elliptical shape. The distortion can be described by a mathematical transformation like equation (3-4), with the coordinate transformation defined as

$$\vec{r}' = \mathbf{S} \cdot \mathbf{R} \cdot \vec{r} \quad (3 - 7)$$

\mathbf{S} is a 2×2 matrix with the form

$$\mathbf{S} = \begin{pmatrix} \frac{1}{\alpha} & 0 \\ 0 & 1 \end{pmatrix} \quad (3 - 8)$$

describing the distortion of the coordinates system, and \mathbf{R} is a rotation matrix. The angle θ is defined as the angle between the x axis and the direction of distortion. The intensity plot along a fixed radius circle $I_r(\theta)$ will not be constant, but will have a nonzero 2nd harmonics component, i.e.,

$$I_r(\theta) = L(r) \cdot a_2(r) \cdot \cos(2\theta) \quad (3 - 9)$$

where $L(r)$ is the limb-darkening function. Notice that this is different from the effect of a linear gradient, which produce a nonzero 1st harmonic term. Thus, the linear gradient and image distortion can be calculated separately. This transformation can be carried out digitally, like the image rotation and shift operation. It is also interpolated with a second order Taylor series. To find the oblateness of the distorted solar images, a symmetrical solar image is constructed with the average limb-darkening function from the data. This artificial solar image is then numerically distorted with different oblateness, and the 2nd harmonics amplitudes at each radius are calculated, and compared with $a_2(r)_{data}$. Figure 3.13 shows the averaged $a_2(r)_{data}$ plotted with the a_2 calculated with artificial images with different distortion. It is clear that the distortion with $\alpha = 1.007$ agrees best with the measured curve.

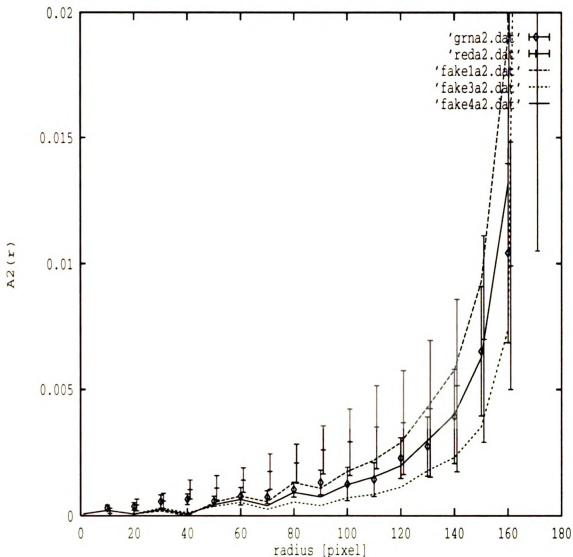


Figure 3.13 $A_2(r)$ Optical Distortion Amplitude. The $A_2(r)$ coefficients of the red and green images are plotted with that from simulated data. The simulated curves were obtained by distorting a perfectly symmetrical artificial solar image. The distortion of fake4a2.dat was 1.007, 1.01 for fake1a2.dat, and 1.0025 for fake1a3.dat. The red $A_2(r)$ was displaced by one pixel to distinguish it from the green curve. $A_2(r)$ of green images follows fake4a2.dat nicely. $A_2(r)$ of the red images are larger than the simulated curve for $r < 120$, due to the larger scattered light noise in the red images. There were 10 green images and 12 red images used for this calculation. The error bar is the 3σ error bar.

Once the amplitude and the phase of the distortion are found, correction can be made simply by performing a transformation with distortion amplitude α^{-1} .

3.4.5 Image Averaging

Given the amplitude and the phase of the distortion, the solar images can now be corrected and averaged. Since the sky transparency may change from time to time, the average intensities for each image are different, and areas with bad pixels will have less data for averaging. Thus, every solar images was rescaled to the same disk center intensity and then added. The summed image is then divided by the number of images contributing to a given pixel to construct a time-averaged image.

3.4.6 Fractional Residual Image Construction

A fractional residual image is constructed by the following formula:

$$\frac{dI}{I}(\vec{r}) = \frac{I(\vec{r})}{\bar{L}(r)} - 1 \quad (3 - 10)$$

where $\bar{L}(r)$ is the circularly averaged limb-darkening function, obtained by binning pixels with radius r from the disk center in 1 pixel intervals. Sunspots, faculae, and bad pixels were discarded by an iterative 3σ cut. Thus, the fractional residual, or contrast image represent the local deficit, or excess of intensity in units of the average photospheric intensity. The low contrast structures were greatly enhanced as is evident in Figure 3.7 and Figure 3.8. Faculae are now clearly visible near the limb. The other interesting feature is the network-like structure visible over the whole disk. This structure is also seen in the infrared data, shown in Figure 3.9 to Figure 3.11. On the large scale, we still see some dark patches appear randomly. This is more profound in the red wavelength images taken after September 6 of 1991. This is identified as due to the scattered light in the system. Next chapter

describes the analysis of the physical characteristics and interpretation of the various brightness structures.

CHAPTER 4

PROPERTIES OF PHOTOSPHERIC NETWORK AND FACULAE

4.1 Introduction

Direct imaging reveals brightness structures of all kind, as is evident from the residual images in Figure 3.8 to Figure 3.12. Solar astronomers named these brightness features by their appearance. The sunspots and faculae are well known, and can be identified clearly in these images. The low contrast cells, resembling the appearance of the better known chromospheric network, is the photospheric network. The photospheric network has been known for decades, however, direct imaging of it is difficult because of the small contrast. Most of the observations up-to-date were obtained at the line core of photospheric absorption lines where the contrast is much higher. We will show in this chapter that the low contrast cells are indeed the photospheric network.

To measure the properties of any feature, we have to find all the image pixels associated with it first. However, it isn't as straightforward as naming when it comes to attributing an image pixel to a particular brightness component. For example, it is easy to identify a sunspot in the image visually, but where do we define the boundary between the sunspot and the surrounding photosphere? Some investigators use magnetic field measurements to distinguish magnetic and nonmagnetic features. When only contrast measurements are available, most investigators make

the attribution by setting a contrast range for each component. This separation is not clear cut, and is acceptable only if the brightness distribution of all components are well separated. This, unfortunately, is not true for most of the cases. An example is the photospheric network which, we will show later, not only is co-spatial with the faculae, but their contrast distribution have a large overlapped region also.

Thus, to make an unbiased separation of the image pixels, we compare the histograms from a 25×100 pixels disk-center quiet region and an active region containing sunspots and faculae on the east limb with the same number of pixels. The range of μ is $0.3 < \mu < 0.5$. These histograms are plotted in Figure 4.1. While the quiet region histogram has a symmetric profile, the active region histogram is more complicated. It has a population scattered over the negative contrast region, and an enhanced positive contrast tail. The negative contrast population is clearly due to the presence of the sunspots. Traditionally, the term faculae refers to the bright patches in the active regions near solar limb in a white light image. Thus, the positive contrast tail can be interpreted as due to the presence of the faculae. If we assume that a quiet region histogram represents the "normal" contrast distribution of the quiet photosphere without sunspots and faculae, then we can measure the contrast distribution of sunspot and faculae by taking the difference between an active and a quiet region histogram, as shown in Figure 4.2. In this figure, the small bump with positive contrast represents the contrast distribution of the faculae. The sunspot appears as the group of image pixels scattered over the negative side of the histogram. The dip around zero contrast then represents the number of pixels in the active region that is transformed from a quiet photospheric pixel to sunspots or faculae pixel.

The quiet photosphere is not featureless, however. It includes the photospheric

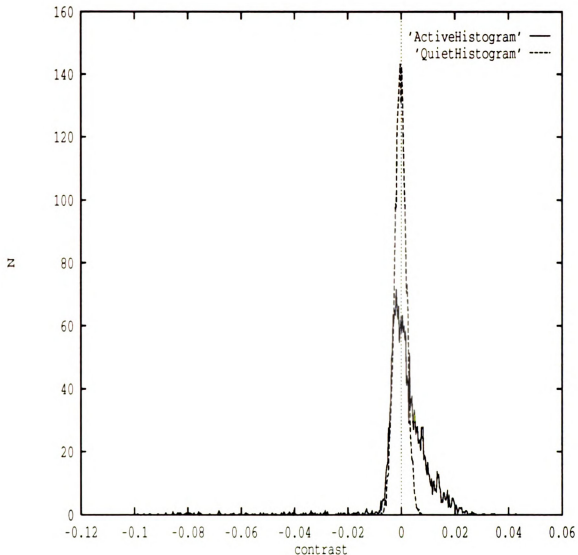


Figure 4.1 Histograms of Contrast From Quiet and Active Regions. The active region contrast histogram was obtained from a 25×100 pixels, or $125'' \times 500''$ area on the east limb with $0.3 < \mu < 0.5$.

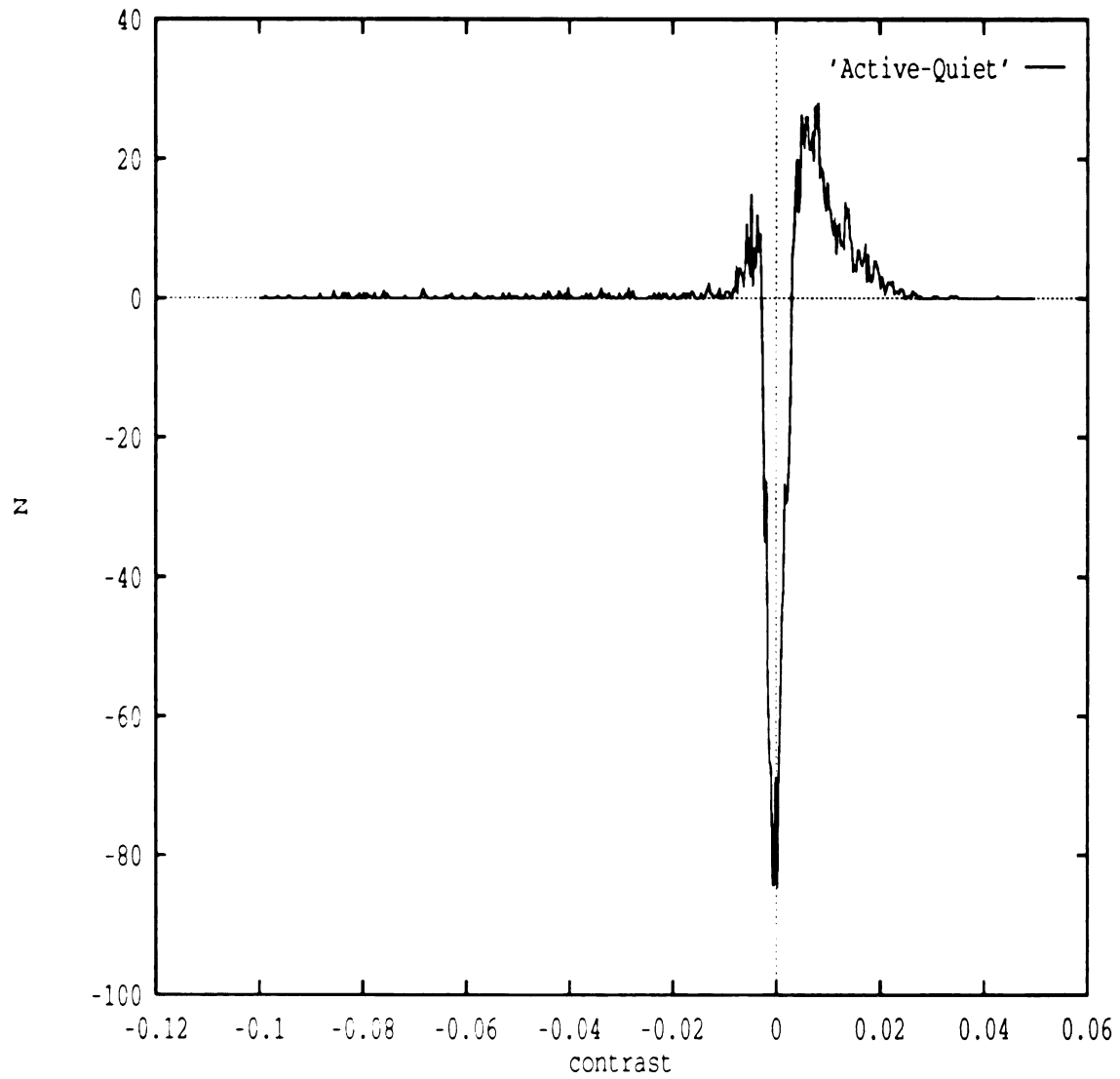


Figure 4.2 Difference Between Active and Quiet Region Contrast Histogram. The positive contrast bump is interpreted as the contrast distribution of faculae. The flat negative contrast component is due to sunspots.

network. Although we can visually identify the photospheric network, the separation of a quiet region into network pixels and quiet photospheric pixels is not possible in our data. The 6" resolution of the SPT smoothed the network brightness to such a low value that it does not appear as a distinct feature in the histograms. Thus, we cannot make an independent measurement of the contrast distribution of the network, and we can only separate the full-disk solar image into a quiet photosphere component, a faculae component, and a sunspot component. The contrast distributions are important for the measurements of the irradiance contribution, and the fact that we can't measure the network contribution to the total solar irradiance is disappointing since the "active network" model predicts that the photospheric network should play an important role in the modulation of the long-term solar irradiance variations. Nevertheless, we can still measure its properties like the spatial scale, and correlation to chromospheric network. We can also measure various properties of the root-mean-square contrast.

Having defined the three brightness components, we can go on to measure their properties. Before doing that, we will first measure the noise in the system. Then, we will present the evidence which identifies the cell structures in the residual images as the photospheric network, and measurements of its properties. The measurements of facular contrast at disk center, and its center-to-limb variations will be presented next. The global scale structure of the quiet photosphere, and the irradiance contributions of these three brightness components will be discussed in the next chapter.

4.2 Noise Estimate

The noise in a photon counting device like a CCD follows Poisson statistics, i.e., $\sigma = \sqrt{N}$, where σ is the error of the measurement in unit of number of photons,

and N is the number of photons collected by the detector. The normalized noise, $\frac{\sigma}{N} = \frac{1}{\sqrt{N}}$ is a measure of the relative photometric accuracy of the measurement. Observations with a CCD detector consist of three measurements: the measurement of the source (the solar image), the dark current measurement, and the pixel-to-pixel gain variation measurement (the flatfield). The accuracy of each measurement is limited by the photon noise. In addition, there exists a fourth term of noise, the readout noise of the detector. This term is usually small, of order of a few electrons, and can be neglected. The reduction of CCD data consists of dark subtraction, and flatfielding, as discussed in chapter III. Since the measurements of the solar flux and dark current are independent, the noise in the dark-subtracted images is the quadratic sum of the individual noise terms, i.e.,

$$\sigma_s = \sqrt{\sigma_{sun}^2 + \sigma_{dark}^2} \quad (4-1)$$

When flatfielding, however, the noise in the flatfield and in the dark-corrected image do not add up quadratically. Denote the dark-subtracted image by S , and the flatfield by g , each subjected to photon noise σ_s and σ_g , respectively. Then we can write $S = S_0 + \sigma_s$, and $g = g_0 + \sigma_g$, where S_0 and g_0 are the true signal and gain, respectively. Thus, the flatfielded image can be expressed as

$$\begin{aligned} I &= \frac{S_0 + \sigma_s}{g_0 + \sigma_g} \\ &\approx \frac{S_0}{g_0} + \sigma_s + S_0 \cdot \frac{\sigma_g}{g_0} \end{aligned} \quad (4-2)$$

The two noise terms, σ_s and $S_0 \cdot \frac{\sigma_g}{g_0}$, are measured independently. Thus, the total noise in the dark subtracted and flatfielded image is the quadratic sum of the two,

$$\sigma^2 = \sigma_{sun}^2 + \sigma_{dark}^2 + S_0^2 \cdot \left(\frac{\sigma_g}{g_0}\right)^2 \quad (4 - 3)$$

The normalized noise then can be determined by

$$\frac{\sigma}{S} = \sqrt{\left(\frac{\sigma_s}{S}\right)^2 + \left(\frac{\sigma_g}{g_0}\right)^2} \quad (4 - 4)$$

Thus, it is the normalized noise that is summed quadratically when flatfielding.

The average pixel intensity in a dark frame is only 150 adu. This is small when compared with the typical disk center intensity of 8,000 to 10000 adu in a solar image. Thus, the noise in the dark frame is usually negligible, and we can write $\sigma_s = \sigma_{sun}$. The photometric accuracy in the skyflats varies as the sky condition changes. On clear days the sky brightness is lower, and the average pixel intensity from a skyflat with 20 minute integration time is typically 1/2 to 1/3 that of the disk center intensity of the sun. The photometric accuracy of the skyflats thus is about 40 % to 70 % worse than that of the solar images. In hazy days the average intensity of a skyflat with the same integration time is usually comparable to the disk intensity of the solar images. In this case, the normalized noise from the skyflats and solar images are comparable.

As will be discussed in the following section, the small-scale noise can be measured by power spectrum analysis. For images obtained with the new Ford CCD, power spectrum fitting of disk center regions showed an average (normalized) noise level near 1×10^{-3} /pixel for the average image of each time step. The average light level of a 20 minutes integration time skyflat is about 10^4 adu/pixel. With a gain of 10 photon/adu, and averaged over 20 solar images, the statistical noise is

7×10^{-4} /pixel/time-step. The noise in a solar image is comparable to the skyflat in the worse case, and better in some cases when the sky was clear. Thus, the combined noise level is 1×10^{-3} /pixel or better, in good agreement with the measured noise. A 5 hours observation yielding 4 time steps in both color will reduce the noise level to 5×10^{-4} /pixel/day.

The infrared array has a large gain of 160 photon/adu, and the light level on the solar disk for each exposure is about 3000 adu. Thus each exposure of the sun yields noise comparable to the noise of the average of 10 visible solar images. Since the flatfields were calculated with the gain iterating algorithm, the theoretical noise in the iterated gain is limited by the noise in the data frames averaged over the number of data frame used for the calculation. This is small and can be ignored. However, the largest source of error in the gain iterating algorithm is the uncertainty in adjusting the average signal due to the fluctuation of sky transparency. This produces bright and dark patches with amplitudes of approximately 1×10^{-3} roughly aligned with the solar limb. Although the amplitude of this error is comparable to the network signal, it can be identified clearly due to the different spatial appearance. This error in the 1992 dataset was greatly reduced in the averaged images.

The photon noise is the dominant source of noise on small scale. On large scale, variation of scattered light is the largest source of error. The visible wavelength contrast images in Figure 3.8 and Figure 3.9 show some extended dark patches with amplitude of approximately 4×10^{-3} even after the optical distortion was corrected. This error was more profound in all the red images taken after Sept. 6, 1991, as shown in Figure 4.3. More careful examination of the images showed that it has roughly the same pattern, and same orientation, but shifts from frame to

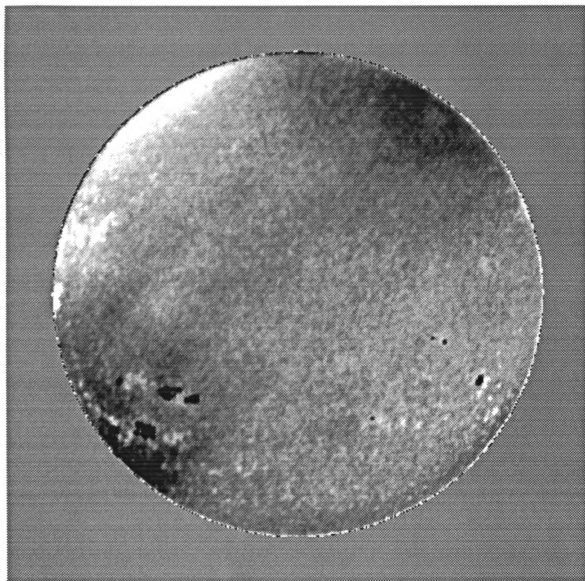


Figure 4.3 Red Contrast Image with Large Scattered Light Contamination. This image was obtained on Sept. 6th, 1991. Display range was -0.02 to 0.02.

frame. We believe that it is an additive effect due to the internal reflection between the CCD chip and the window of the CCD dewar. Some large dust particles must have fallen onto the red interference filter between Sept. 4th, and Sept. 6th. The increased scattered light in the red band pass increases the amplitude of the noise in all the red images taken after Sept. 6th. Reflections due to the highly reflective surfaces of the neutral density filter and the interference filters are unlikely, since they are placed far away from the CCD, and they are tilted slightly with respect to the optical axis.

4.3 Properties of The Photospheric Network

4.3.1 Cross-Correlation Between Different Time Steps and Colors

One of the interesting feature in Figure 3.8 and Figure 3.9 is the bright and dark mottles resembling the appearance of network. To better show the structure of these mottles, the running average of a 32 pixels diameter mask was calculated, and subtracted from each residual images. This process removes the low frequency structure from the image. We then apply a low pass filter by computing the running average of a 2 pixels radius mask. Figure 4.4 and Figure 4.5 are the filtered image of Figure 3.8 and Figure 3.9 respectively, and show more clearly the structure of the mottles. To verify that this structure is indeed of solar origin, cross-correlations between the two band passes, and between different sets for each band pass were calculated. Figure 4.6.c, Figure 4.6.f, and Figure 4. 4.6.i show the cross-correlations of the disk center region between the red and green band pass for the first to third set. Strong correlation was observed in the 2nd and 3rd sets. The cross-correlation of the 1st set is noisy, but it still shows significant correlation signal. Since there are approximately 40 minute intervals between successive sets, the cross-correlation between different datasets should show a solar rotational signal. This is clearly seen

from Figure 4.6. We conclude that the dark and bright mottles seen in Figure 3.8 and 3.9 are indeed structures on the solar photosphere.

Figure 3.10 to Figure 3.12 are infrared residual images, filtered like the visible images. Structures similar to the network in the visible images are clearly visible. There are also arc structures introduced by the iterated flatfielding routine in the K band image. This error was reduced in the J and H band images by averaging. This error was due to the uncertainty in adjusting the mean signal variation due to the fluctuation of sky transparency. Figure 4.7 shows the cross-correlations between the H and K band images of the 1990 observations near disk center, as well as the cross-correlations between different exposures of the same band pass. Figure 4.8 shows the cross-correlation between the J and H band images near disk center from the 1992 data set. Since there were only 10 images covering different part of the solar disk in each bandpass in the 1990 data set, we cannot average the images to reduce the residual flatfielding noise. The cross-correlations between the H and K band images are noisy. Nevertheless, images of the same bandpass show significant cross-correlation. In the 1992 data set, there were approximately 100 images for each scan, so we could average the images to reduce the flatfielding noise, and the good correlation between the J and H band images is evident in Figure 4.8.

4.3.2 Power Spectrum Analysis

The scale of the network was measured by power spectrum analysis. Power spectra of four 128×128 pixels ($890'' \times 890''$) regions at the disk center, filtered by a high pass filter with cutoff frequency of 0.05 radian/Mm, were calculated, and averaged to obtain an average spatial power spectrum for both the red and green band pass. Three 64×64 pixels ($606'' \times 606''$) images were used to obtain the average power spectrum of the H and K band in the infrared. Figure 4.9 shows the average

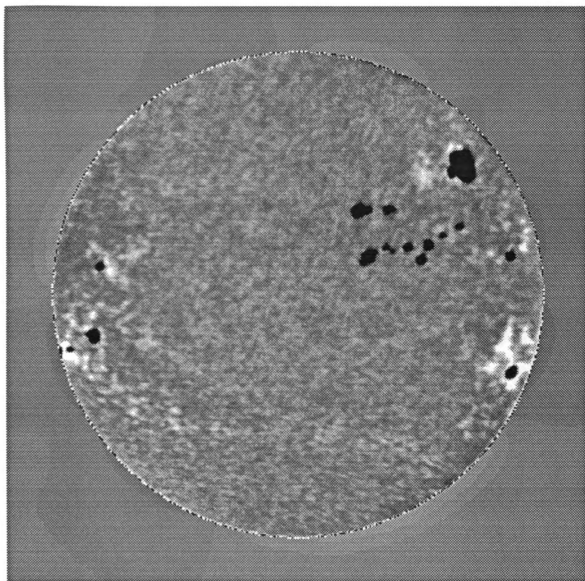


Figure 4.4 Filtered Green Band Contrast Image Showing Photospheric Network. This is the same image that is displayed in Figure 3.8. Display range is -0.02 to 0.02.

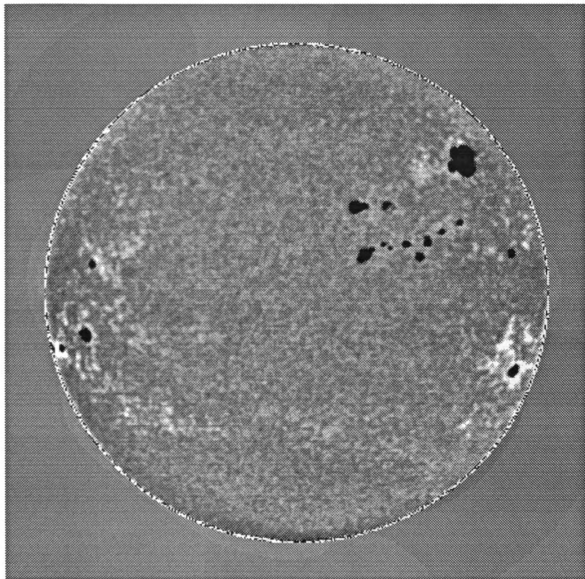


Figure 4.5 Filtered Red Band Contrast Image Showing Photospheric Network. This is the same image that is displayed in Figure 3.9. Display range is -0.02 to 0.02.

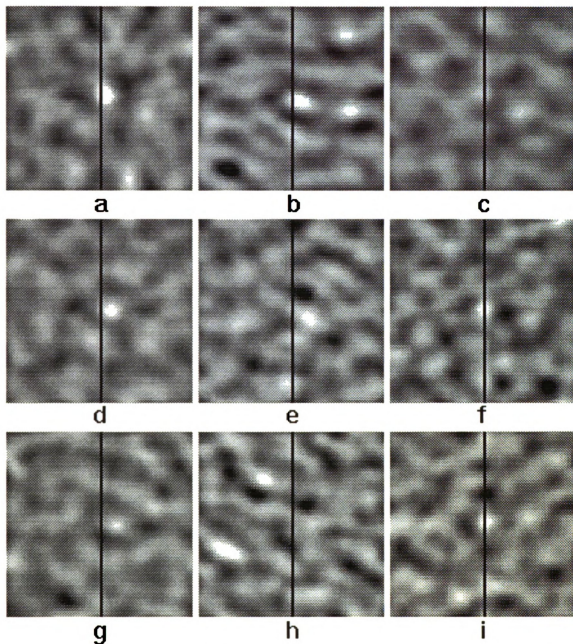


Figure 4.6 Cross-Correlation of Visible Wavelengths Images. Black lines mark zero shift position. Panel c, f, and i are the cross-correlation of the 1st, 2nd, and 3rd time step between the red and green images at disk center, respectively. Strong correlation between the two colors is evident. Panel a, d, g and b, e, h are the cross-correlation of the red and green images between the 1st and 2nd, 1st and 3rd, and 1st and 4th time step, respectively. The peaks of the time correlations (Panel a, d, c, and Panel b, e, h) shift to the right due to solar rotation. Each time step is about 80 minutes apart. The area used to do this calculation is 64×64 pixels, or $448'' \times 448''$.

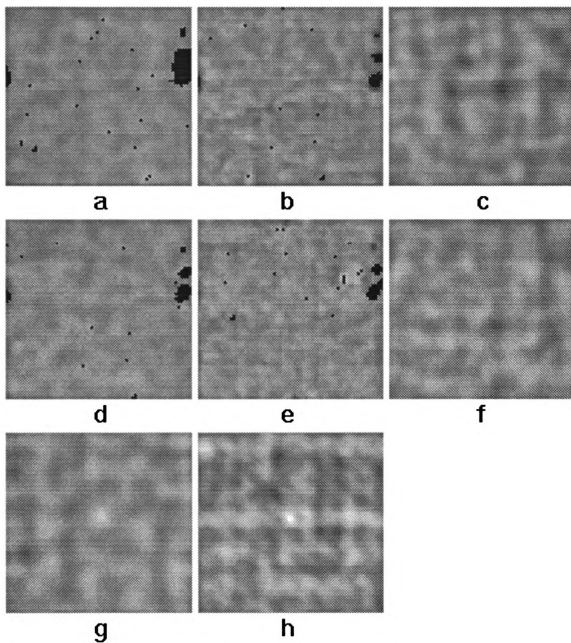


Figure 4.7 Cross-Correlation of Infrared Wavelengths Images. Panel a and d: H band residual images. The time interval between the two images were about 10 minutes. Panel g: Cross-correlation between a and d. Panel b and e: K band residual images. Panel h: Cross-correlation between b and e. Panel c: Cross-correlation between a and b. Panel f: Cross-correlation between d and e.

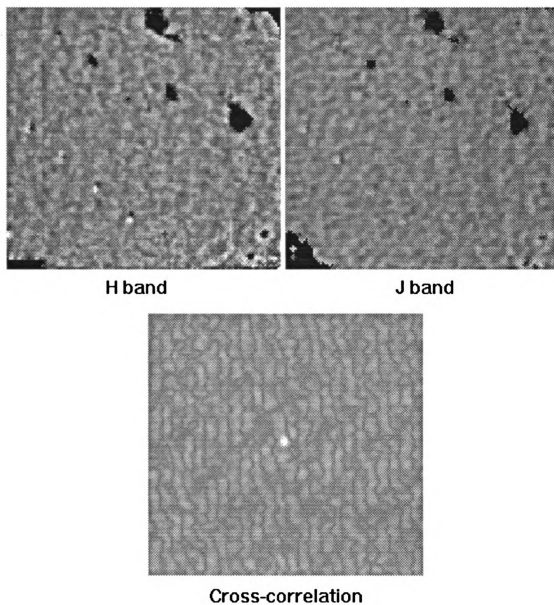


Figure 4.8 Comparison of Faculae in J and H Band Near Disk Center. The lower panel is the cross-correlation map of the two images. Sunspots were marked such that they don't contribute to the cross-correlation calculation. Large positive peak at zero shift indicating positive correlation is clearly visible.

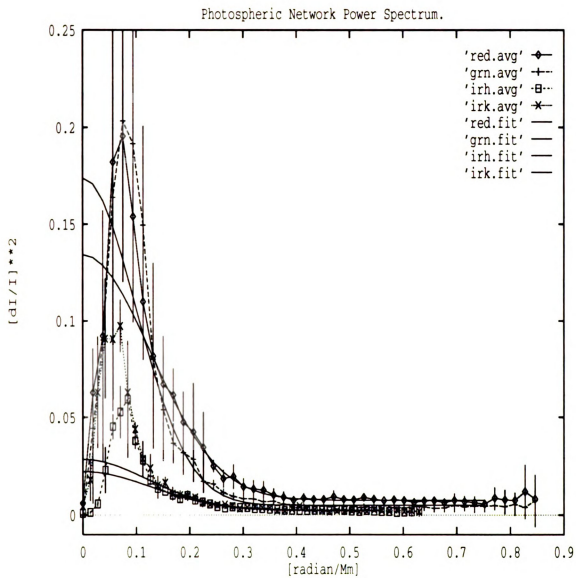


Figure 4.9 Average Power Spectrum of Photospheric Network. A Gaussian profile was fitted to the shoulder at $k=0.2$ radian Mm^{-1} . Solid lines show the fit.

power spectrum of the red, green, H, and K bandpass data. There are no significant peaks in the spectra. This is not unexpected, since a peak in the power spectrum implies the existence of long range order in the structure. Phenomenon such as waves do have long range order. However, the random distribution of dark and bright patterns observed in the residual images does not suggest long range order. The power spectrum of this kind of structure should be flat at low frequencies and fall off at higher frequencies, e.g. Lorentzian (Keil, Kuhn, Lin, and Reardon 1992). So, the feature of interest in Figure 4.9 is the shoulder around 0.2 radian/Mm. The presence of this shoulder in the power spectrum of all 4 band-pass indicates that it is not an artifact. This is the signal associated with the network structure.

We can construct a simple model to explain the observed power spectrum. Consider a 2D array populated with random numbers with rms amplitude σ . If this array is convolved with a Gaussian function with characteristic length λ , i.e., replacing the array element with the local average weighted by the gaussian envelope, the resulting image will have structures similar to the bright and dark mottles observed. There will not be long range ordering, since the correlation between any two points with distance d apart is the strength of the gaussian function at distance d away from the centroid. The power spectrum of this structure is

$$P(k) = [\sigma(k) \cdot G(k, \lambda)]^2 \quad (4 - 5)$$

where $G(k, \lambda) = \exp(-\lambda^2 k^2 / 2)$ is the Fourier transform of the gaussian function

$$G(x, \lambda) = \frac{1}{\sqrt{2\pi\lambda}} \exp\left(-\frac{x^2}{2\lambda^2}\right) \quad (4 - 6)$$

Since the gaussian function falls to 0.5 % of its central value at distance 3λ , a good estimate of the average cell size should be $l = 6\lambda$.

To calibrate this model, we calculated the power spectrum of solar granulation images in the infrared H band obtained with the infrared array camera with the vacuum tower telescope at Sac. Peak. The average power spectrum was fitted to the formula

$$P(k) = A \exp(-\lambda^2 k^2) + B \quad (4 - 7)$$

In this model, the amplitude A is a measure of the amplitude of the contrast of the structures, B is a measure of the noise in the images, and λ is the characteristic length of the structures. The fitted value of λ is $\lambda = 213$ km, which gives cell size of $6\lambda = l = 1,278$ km. This agrees well with the measured granule size of 500 km to 2,000 km. The fit of the shoulder of red, H, and K band in Figure 4.9, and power spectrum from green images of Sept. 4th, 1991 gives $l = 33,480 \pm 2400$ km. The green power spectrum from the 1990 data gives $l = 39,000$ km, but we have some evidence that the green images were poorly focused.

4.3.3 Cross-Correlation With The Chromospheric Network

Having established the size of the network, we calculated the correlation of the observed network with the chromosphere network. The NSO at Sac. Peak provided the CaK image of August 2nd, 1990. It was digitized by the Fast Scanning Micro Densitometer also at Sac. Peak. Figure 4.10 shows the cross correlation between the observed network with CaK network in regions near the solar north pole, disk center, and solar south pole. The chromosphere CaK network has been known to outline the supergranulation (Simon and Leighton 1964), as the photospheric

network does (Muller 1983). Hence, the positive correlation shown in Figure 4.10 comes as no surprise.

4.3.4 Cross-Correlation With the Supergranulation Velocity Field

It is also interesting to check the correlation between the observed network and SG velocity field. Assuming the velocity field of the supergranulation is driven by a convective process, the temperature structure should be hot at the cell center, and cool around the cell boundary. The divergence of the velocity field should be correlated with the temperature field. The simplest model suggests that

$$\nabla \cdot \vec{V} = \alpha T \quad (4 - 8)$$

where \vec{V} is the 2 dimensional surface velocity field, T is the surface temperature field, and α is a scaling constant. If we assume that $\vec{V} = \nabla\phi$, then we can solve for ϕ , given the measured temperature field, by solving the Poisson equation for ϕ ,

$$\nabla^2\phi = \alpha T \quad (4 - 9)$$

Thus we can infer a velocity field from $\vec{V}_{inf} = \nabla\phi$ based only on the measured temperature field.

Since the velocity field of supergranulation is predominantly horizontal, we should look for a correlation between the inferred velocity field and the measured velocity field near the limb. The velocity measurements we use were obtained at Big Bear Solar Observatory, provided by Dr. M. Woodard. Figure 4.11 shows the measured velocity field at the north (4.11c) and south (4.11d) limb, the inferred velocity field of the same regions projected along the direction toward the disk

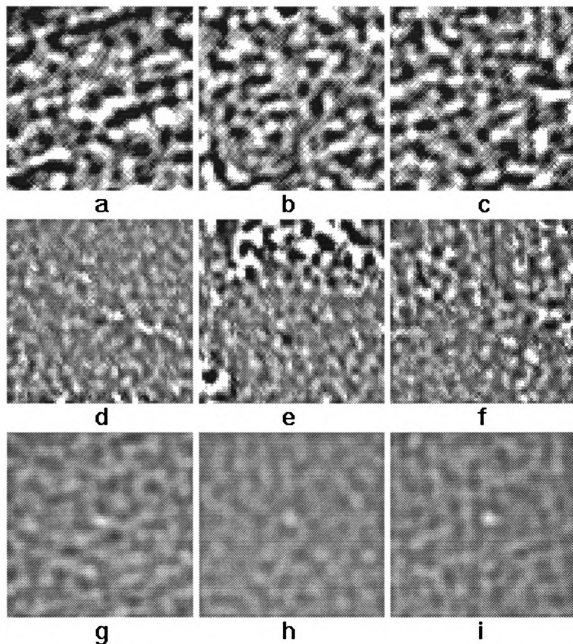


Figure 4.10 Cross-Correlation Between Photospheric Network and CaII Network. Panel a to c: 64×64 pixels area of the red residual images near the solar north pole, disk center, and south pole. Panel d to f: CaII K images from the same area as panel a to c. Panel g, h, and i: cross-correlation between panel a and d, b and e, and c and f, respectively. Strong correlation between the residual images and the CaII K images are clearly visible.

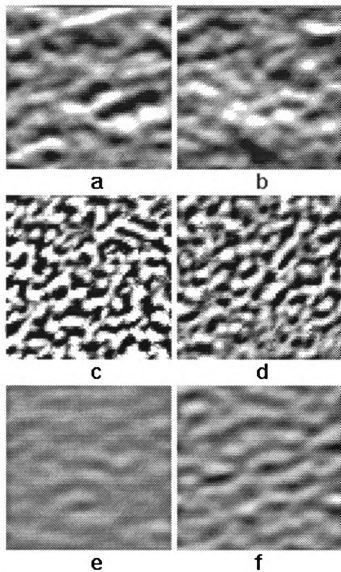


Figure 4.11 Cross-Correlation Between Supergranulation and Photospheric Network. Panel a and b: Inferred velocity field projected along the line-of-sight from regions near the solar north and south pole, respectively. Panel c and d: measured velocity field from the same regions as a and b. Panel e and f: Cross-correlation between a and c, and b and d, respectively. There are signs of negative correlation peak near zero shift.

center (4.11a and 4.11b), and the 2D cross-correlation between the measured, and inferred velocity field at the north (4.11e) and south (4.11f) limb. The covered area is about $450'' \times 450''$. This simple model to infer the velocity field doesn't take into account surface projection effects. The correlation maps are also noisy. However, both cross-correlation maps show definite negative peak near zero shift. The displacement of the peaks from the zero shift is probably due to the uncertainty in selecting the corresponding area from the velocity and temperature measurements, since there was nearly a 4 hour difference between the observations. Nevertheless, the negative correlation suggests that if the observed brightness structures are the thermal signature of a convective process, then the velocity field generated will have opposite direction with respect to the SG velocity field. Thus, we conclude that the observed brightness structure with SG scale is not the thermal signature of the convective flow associated with the supergranulation. This negative correlation can be expected from the positive correlation with CaK network.

It is clear from the above analysis that this brightness structure with characteristic scale of 32,000 km is the photospheric counterpart of the chromospheric network, the photospheric network.

4.3.5 Line Contribution to Network Contrast

The band pass of 100 \AA includes many absorption lines, which are formed higher in the atmosphere. The solar spectrum in the red and green bandpass are shown in Figure 4.12 and Figure 4.13, respectively. Since the spectroheliograms obtained in the core of the photospheric lines show high intensity modulation in the network, the broad band photometric measurements are contaminated by the line emission. The $H\alpha$ line is included in the wing of the red filter, as shown in Figure 4.12. The central 1 \AA of $H\alpha$ line contributes 0.1 % of the total intensity in the red band

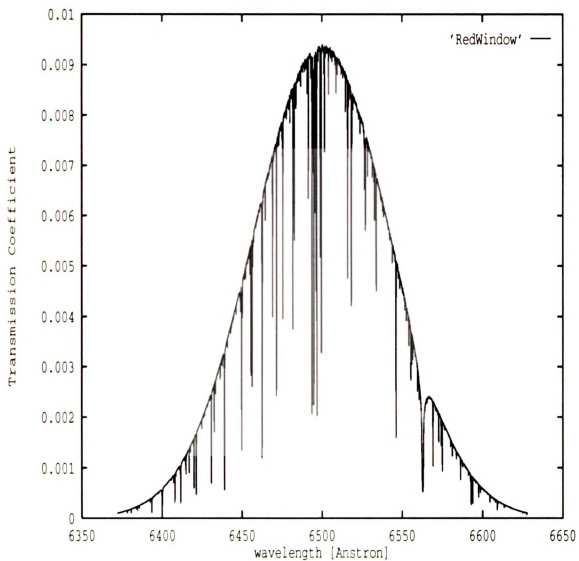


Figure 4.12 Transmission Function of the Red Filter. The transmission function of the filter (the Gaussian profile) was multiplied by the solar spectrum. The $H\alpha$ line at 6563 \AA is included near the wing.

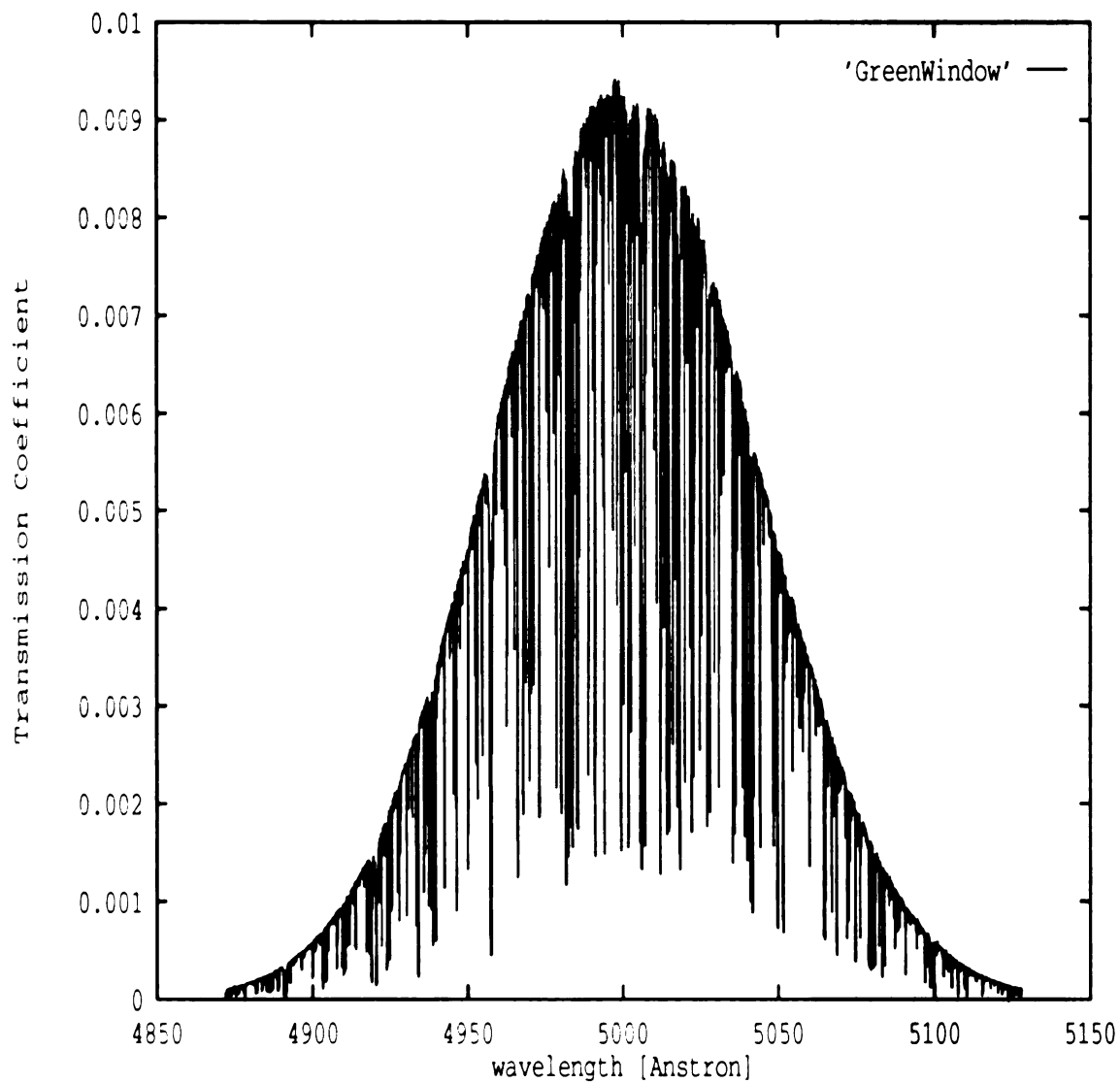


Figure 4.13 Transmission Function of the Green Filter. The transmission function of the filter (the Gaussian profile) was multiplied by the solar spectrum.

pass, since the transmission coefficient of the filter at $H\alpha$ is about 10 % of the peak transmission. Thus, a 10 % intensity modulation in the center of $H\alpha$ in the network will produce an intensity modulation of 10^{-4} . We estimated the total line contributions to the observed intensity by computing the fraction of the line emission to the total emission within the band-pass. The digitized Kitt Peak solar atlas was used for this calculation. The lines were identified with a pre-defined transmission coefficient threshold, i.e., all the emission with strength less than the threshold were identified as line emission. The line contributions vary with the threshold. For a threshold between 0.9 to 0.3, the line contributions vary from 6.2 % to 0.13 % in the red, and 19 % to 0.6 % in the green. This result predicts a green intensity modulation of 3 to 5 times larger than the red. This is inconsistent with our observations as discussed in the following section. Thus, we do not believe the line emission is the source of the observed intensity modulation in the network.

4.3.6 Photospheric Network Contrast near Disk Center

The above analysis established that the observed bright and dark mottles seen in Figure 4.4 and 4.5 are the photospheric network. Of interest are the contrast at disk center, and the center-to-limb variation of the contrast. The contrast of the network at disk center is measured by calculating the standard deviation of the central $450'' \times 450''$ area. The amplitude of the contrast is $(2.34 \pm 0.38) \times 10^{-3}$, $(1.83 \pm 0.51) \times 10^{-3}$, $(1.02 \pm 0.21) \times 10^{-3}$, and $(1.11 \pm 0.21) \times 10^{-3}$ for the green, red, H, and K band, respectively. Figure 4.14 shows the contrast vs. wavelength, with the contrast of a $5,800^\circ$ K blackbody with 2.9° K deviation. The green contrast was calculated from the June 1991 data taken with the new CCD. The 1990 green images were not used due to the focusing problem. The red contrast calculated from the August 1990 data and June 1991 data are consistent. It is clear that the

brightness signal of the network has approximately thermal wavelength dependence. Whether this is truly thermal due to some kind of local heating mechanism (e.g. magnetic heating), or is associated with the "hot wall" of the thin magnetic flux tubes is not clear, however.

4.3.7 Center-to-Limb Variation of Network Contrast

Figure 4.15 to Figure 4.18 shows the center-to-limb variation (CLV) of the contrast of the north and south active latitudes, and along the north-south axis in the green, red, H and K band. The regions from north (south) 15 degree to 45 degree were used to calculate the CLV of the north (south) active latitudes, and a region 30 degree wide, centered around the north-south axis was used for the quiet region. The CLV of the contrast was obtained by computing the rms amplitude of the pixels within a radial bin of 1 pixel interval within the selected region. Facular and sunspot pixels were discarded by repetitive 3σ cut. Since the number of pixels per radial bin is proportional to the radius, it is small near disk center. Thus, the rms contrast in this region shows some fluctuations. At $\mu = 0.9$, or $r = 56$ pixels, the radial bins of the active and quiet regions should contain more than 100 pixels. Thus, the rms amplitude is a good representation of the network contrast. The CLV of the quiet region contrast shows little variation in the visible wavelength, and that of the north and south active latitudes increase linearly from near disk center to $\mu \approx 0.35$, then rises sharply toward the limb. This is expected from the increase of bright pixels in the form of enhanced network and bright patches in the active regions.

The CLV of the contrast in the infrared was calculated by averaging the CLV of images from the 1990 observations. Since each image covers only part of the solar disk, the covered range in μ is different from image to image. The CLV of the

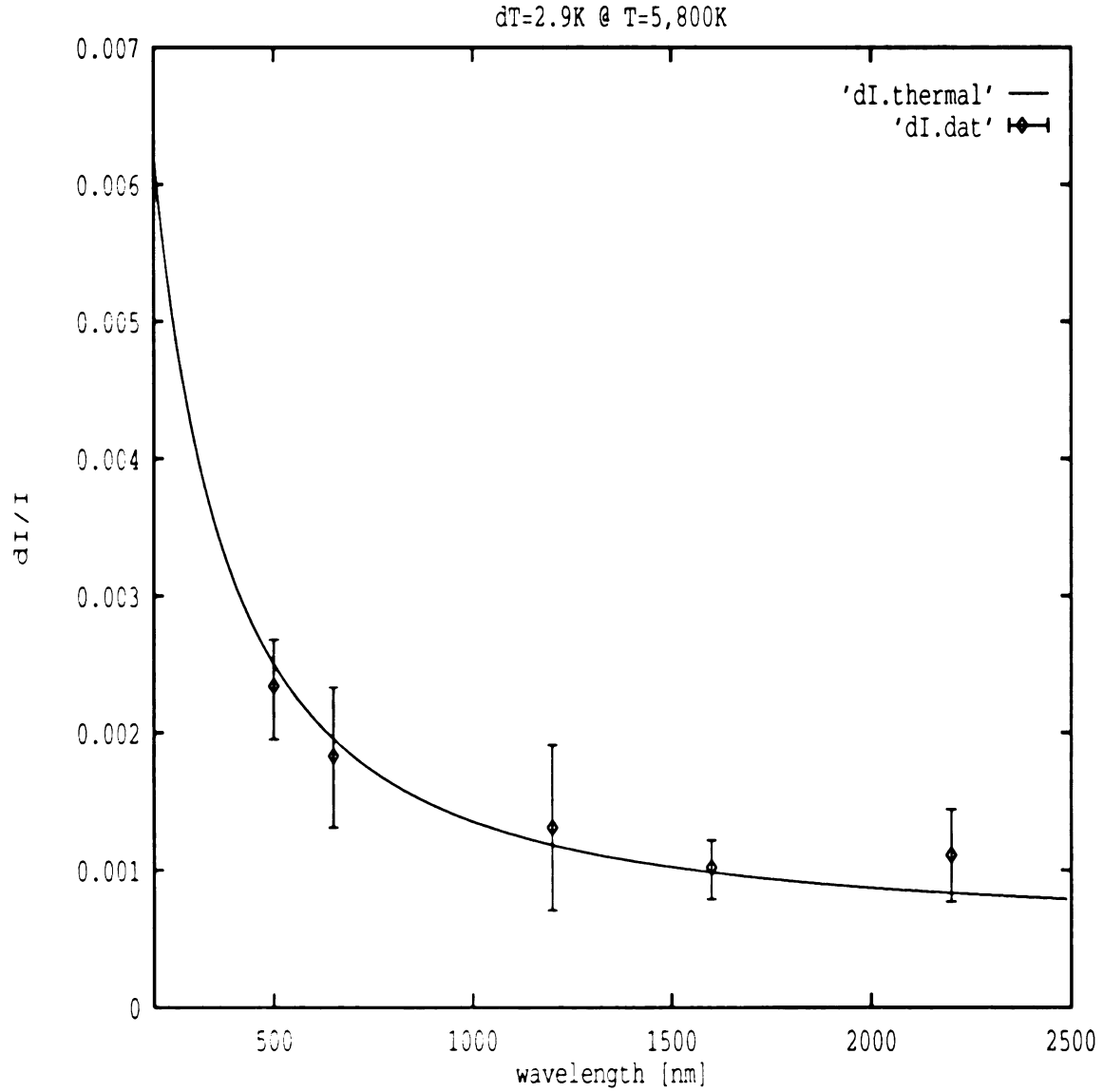


Figure 4.14 Photospheric Network Contrast Near Disk Center. The solid line is the theoretical contrast of a temperature perturbation of a blackbody at 5800 K with perturbation amplitude of 2.9 K. The error represent the 3σ scatter of the data.

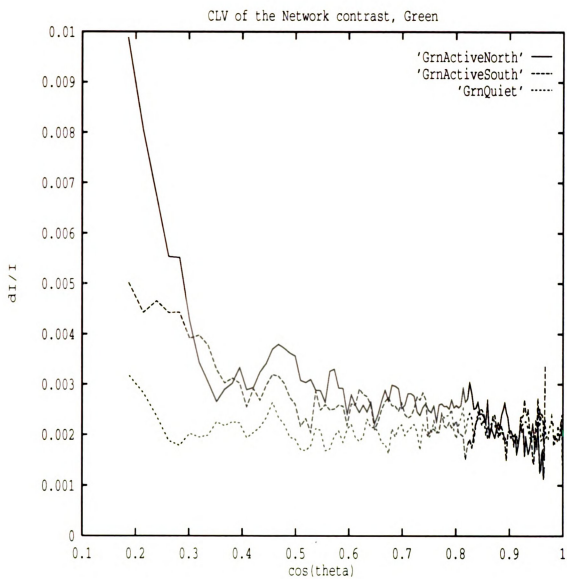


Figure 4.15 Network Contrast Center-to-Limb Variation in Green Band.

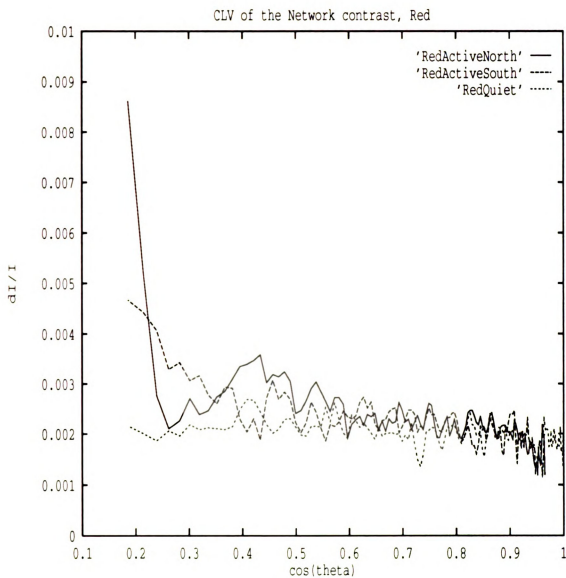


Figure 4.16 Network Contrast Center-to-Limb Variation in Red Band.

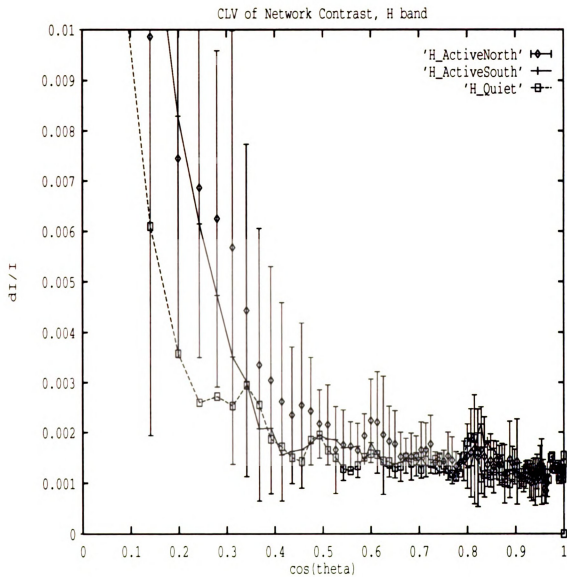


Figure 4.17 Network Contrast Center-to-Limb Variation in Infrared H Band.

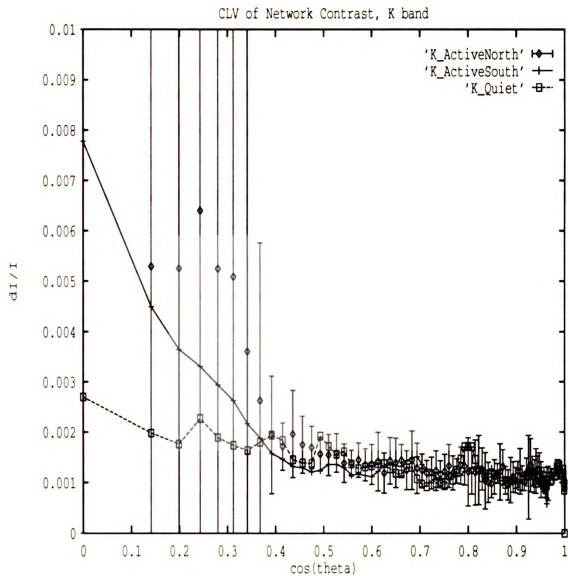


Figure 4.18 Network Contrast Center-to-Limb Variation in Infrared K Band.

contrast in the H band shows no distinction between the active and quiet region for $0.4 < \mu < 1$ and a rapid rise for $\mu < 0.4$ in both the active and quiet regions. The CLV of the K band images are similar to that of the H band, except that the CLV of the quiet regions did not rise to a high value, as the visible data. Since a filter with diameter of 20 pixels was used to remove the low frequency structures from the images, the filtering in the regions within 10 pixels from the limb have less weight. Thus, the CLV of the contrast in these regions, ie., the regions with $\mu < 0.4$ are noisier, as is reflected in the large error bar in this range. In the range between $0.4 < \mu < 1$ we expect to see a steady increase of contrast in the active latitudes similar to the visible data. Although the error in this range is smaller, it is still large compared to the small linear rise, if it does exist. Thus we conclude that the infrared data are too noisy to give a reliable measurement of the difference between the CLV of the active and quiet network between $0.4 < \mu < 1$. Although the CLV near the limb are very noisy, nevertheless, the rapid rise of the H band CLV is interesting. The H band continuum originates from the deepest observable layer in the solar photosphere when observed near disk center – 35 km below $\tau_{500} = 1$. The K band continuum is formed about 25 km above $\tau_{500} = 1$ (Vernazza, Avrett, and Loeser 1976). This is an interesting region of the solar atmosphere where the opacity is rapidly changing. Toward the limb, the H band images integrate larger physical depths due to the smaller opacity. Thus more of the network structures were included in each limb pixel in the H band than in the K, and visible wavelengths bands. This may cause the rms contrast to rise faster in the H band. Whether or not this difference between the CLV of the contrast in the H band and the other wavelengths represents different physical conditions at different heights needs further investigation.

4.3.8 Temperature Structure of Supergranulation

The supergranulation (SG) is suggested to be the convective flow associated with the He ionization layer (Simon and Leighton 1964, Leighton 1964) Many authors (Beckers 1968, Frazier 1970, Worden 1975, Koutchmy 1978, Foukal and Fowler, 1984) attempted to observe the thermal structure associated with this large scale convective flow, but the results are inconclusive. To date, there are no published theoretical models, nor numerical simulations of SG predicting the contrast of the thermal structure of the SG. Our observation suggests that any thermal structure associated with a convective flow of the SG must be imbedded in the brightness signal of the photospheric network and have an amplitude less than 3 K.

4.4 Properties of Photospheric Faculae

4.4.1 Spatial Distribution of Faculae

It is clear from the residual images that faculae, the extended bright patches seen near the limb, is absent near disk center. Tracing the faculae as they rotate into disk center from images taken on consecutive day, like the June 4th to June 8th series of 1991, showed that the facular contrast decreases rapidly with increasing μ . Thus, identifying faculae near disk center is difficult. Furthermore, the observation of Muller and Keil (1983) showed that FBPs form the perimeter of the network cell. Thus, faculae and network are really indistinguishable, at least near disk center. In the active regions near the limb, the issue is more complicated. There exist extended bright patches, as well as enhanced network. We had shown from comparison of active and quiet regions histograms that faculae increase the number of bright pixels in an active region. This can be explained either by a higher concentration of the facular bright points (FBP), or higher FBP contrast, or both. There also exist bright features of size from 0.5" to 1.5" called facular knots (Spruit and Zwaan

1981) or facular granules (Mehltretter 1974, Muller 1977) in the active regions which may contribute to the increased contrast. To study the spatial structure of bright patches, the power spectrum of 564×64 pixels regions from the red residual image, four from the active region at the northeast, northwest, southeast, and southwest corner of the solar disk, and one from a disk center quiet region were calculated and fitted to the formula of equation (4-7). If these bright features (FBP's, Facular knots, and Facular granules) appear as isolated bright points scattered over the active regions, then they should contribute a spectral frequency independent power to the power spectrum, thus a higher B . On the other hand, if the faculae appear as large extended bright patches, then they contribute to the low frequency part of the power spectrum. All the power spectra show structures with the same characteristic length, and same level of noise B . However, the active region power spectra show amplitudes A larger than the quiet region power spectra, suggesting that the high contrast pixels appear in the enhanced active network.

4.4.2 Faculae Contrast Near Disk Center

And Its Center-to-Limb Variation

The center-to-limb variation of facular contrast is of special interest to solar astronomer, since it bears information about the vertical structure of the thin magnetic flux tube, which is the basic constituent of faculae. It is also important for the proxy estimate of the faculae contribution to the solar irradiance variation. However, the facular contrast near disk center is not well-defined up to date. Most authors adopted zero contrast at disk center, but spatially resolved study showed that individual facular flux tube may have contrast as high as 40 % (Muller and Keil, 1983). The most interesting observation might be the measurements of Foukal, Little, Graves, Rabin, and Lynch (1990), and Foukal, Little, and Mooney (1989)

which showed that the faculae contrast is negative in the infrared H band near disk center. Since our analysis method described in Section 4.1 defines faculae as the excess number of bright pixels of histogram when compared with average quiet region histogram, we cannot check if the faculae contrast is indeed negative near disk center in the infrared H band with this definition. Nevertheless, we can still check the correlation between our infrared H band and J band images of the same area taken near disk center. This was shown in figure 4.8. Unit opacity of J band occurs at about the same height of $\tau_{5000} = 1$, hence if Foukal's claim is true, we would see negative correlation between the J and H band images. Although the two images were taken 90 minutes apart, there exists long-lived features such that the cross-correlation map showed positive peak at zero shift, suggesting positive correlation between the two images. Thus our observations suggest that most of the faculae in the infrared H band near disk center are bright compared with the surrounding photosphere.

The results of facular contrast distribution observations up-to-date are highly subjective to bias introduced by the analysis method. As we argue below, these methods tend to overestimate the facular contrast in most circumstances. Most authors (Nishikawa and Hirayama 1990, Hirayama, Hamana, and Mizugaki 1985, Chapman, Herzog, Lawrence, and Shelton 1986) define facular pixel in the images by choosing pixels with contrast higher than a fixed threshold. This definition is certain to bias the facular contrast. Lawrence (1988), and Lawrence, Chapman, and Herzog (1988) found the facular contrast distribution by assuming that an active region histogram is the superposition of a quiet photosphere component and a faculae component. In their analysis, two adjacent rectangular areas containing a few hundred pixels each were selected: one containing some facular pixels, the other

only quiet photosphere. The quiet photosphere rectangle were used to construct a quiet region contrast distribution. This distribution was then fitted to the low-contrast end of the combined histogram of the two rectangles by adjusting its mean and height. The difference of the combined histogram and the fitted histogram was interpreted as the contrast distribution of faculae. The two-component model of the histogram is a more reasonable assumption, however, the fitting procedure to find the quiet sun contrast distribution is really redundant, since it should be well represented by the contrast distribution of the quiet photosphere rectangle. Also the choice of regions containing easily identifiable facular pixels unavoidably involves human bias as to what is perceived as facular and runs the risk of neglecting the dimmer facular pixels. Thus, their analysis also tends to overestimate the facular contrast.

The method we used to obtain the faculae brightness distribution as described earlier is unbiased, since a large area including all the possible facular candidates were used to obtain the contrast distribution. However, the power spectrum analysis in Section 4.3.2 showed that most of the bright features appear as network. Thus, the division of it into a network and a faculae component seems groundless. On the other hand, the intrinsically different shape of the active and quiet regions contrast histogram does suggest that there are some differences in the properties between the two regions. Thus, we follow the traditional convention and define the excess number of bright pixels in the active region as faculae and treat them separately. What is the difference in the structure of the small flux tube in quiet regions network and in active region network? We are not in a position to answer this question here. An observation measuring the distribution of magnetic field strength in active and quiet regions, and the correlation between the magnetic field

strength and continuum contrast will provide more information on this issue.

To calculate the CLV of facular contrast, an average quiet region histogram $n_{quiet}(c)$, where c is the contrast, is obtained by averaging several quiet region histograms taken from different data set. Notice that $\bar{N}_{quiet}(c)$ has no μ dependence, since flat network contrast CLV in quiet region derived in section 4.3.7 inferred that there are no difference between the histograms of quiet photosphere at disk center and near solar limb. Histograms $N(\mu, c)$ of all the pixels with distance μ from solar disk center is also generated. Since each radial bin would contain different numbers of pixels, the histograms were normalized by the total number of pixel for each radial bin. That is,

$$n(\mu, c) = \frac{N(\mu, c)}{\sum_{c=-\infty}^{\infty} N(\mu, c)} \quad (4 - 10)$$

The summation over the whole range of contrast gives the total number of pixels in the given μ bin. The average quiet region histogram has to be normalized similarly. Denote the normalized quiet region histogram by $\bar{n}_{quiet}(c)$, we then calculate the differences between $n(\mu, c)$ and $\bar{n}_{quiet}(c)$. The excess number of bright pixels then gives the contrast distribution of faculae at that radius, i.e.,

$$n_{fac}(\mu, c) = n(\mu, c) - \bar{n}_{quiet}(c), \text{ for } c \geq 0, \text{ and } n \geq 0 \quad (4 - 11)$$

The average facular contrast as a function of μ can then be found by calculating the average contrast of all the excess bright pixels.

$$\bar{C}_{fac}(\mu) = \frac{\sum_{c=0}^{\infty} n_{fac}(\mu, c) \cdot c}{\sum_{c=0}^{\infty} n_{fac}(\mu, c)} \quad (4 - 12)$$

We calculated the CLV of the facular contrast of the 1991 visible wavelengths data listed in Table 3.1 and the 1992 infrared wavelengths data listed in Table 3.2, and the average CLV is plotted in Figure 4.19. The facular contrast measured by other authors were plotted also. The 100 images of each scan of the infrared data were mosaic together to make a full-disk infrared residual image in both the J and H band. Since there are large-scale scattered light error in the visible images, and the mosaicking procedure also produce large-scale error due to the uncertainties in adjusting overall intensity level between images, the full-disk contrast images were first filtered by a high-pass filter. The amplitude of these large-scale error are of order of a few tenth of a percent, this represents a error of the same order of magnitude in the small-scale contrast, which is acceptable. The CLVs of each full disk image were then averaged to obtain the average CLVs in Figure 4.19. The infrared CLVs rise sharply around $\mu = 0.3$. The visible wavelengths CLVs rise around $\mu = 0.15$. This may be due to contaminations of filtering error near the limb. This plot shows that the facular contrast does not vanish even at disk center. Also, we found that the facular contrast near the limb is smaller than some previously measured values. This is not a surprising result judging from the peak position of the facular contrast distribution in Figure 4.2. The difference between our measurements and the results of the others is clearly due to the lack of good references with which one can identify facular pixels unambiguously in the other observations. The low contrast facular pixels were simply been ignored by most observers. For example, Hirayama, Hamana, and Mizugaki (1985) used $H\alpha$ filtergrams to help identify fac-

ular regions in the continuum images, and the maximum excess intensities of the identified facular regions were used as representative of the facular contrast. Thus, they only counted the brightest facular pixels, and it is obvious that they should derive a much higher facular contrast.

The size of individual FBP is small, and with a spatial resolution of 1" or worse, each image pixel would contain several FBPs. The spatial resolution of the SPT changes from 7" in the 1990 dataset to 5" in the 1991 dataset. It is 2" in current configuration. We did not see any significant spatial resolution dependence in the observed contrast value. Since the spatial resolutions of the other observations fall mostly in this range, differences between spatial resolution may not play an important role here.

One may argue that with our definition of facular contrast distribution, one may always find image pixels with contrast higher than the average, and one cannot tell whether the excess contrast is really due to the presence of FBPs in the pixel, or it is just some brighter nonmagnetic pixels. Also, since the image pixels lost their identity in the histogram, we cannot make comparison with magnetic measurements to help identify facular pixels. Thus, one may argue that the nonzero facular contrast derived may not be accepted with confidence. However, if the brighter pixels are really due to the brightness variation of nonmagnetic photosphere, the difference between the histograms should show white-noise like distribution. This is not the case in the facular contrast contribution in Figure 4.2, which shows a population with positive contrast. Thus, we are confident that our definition of facular contrast distribution of equation (4-2) is of statistical significance. The spatially resolved facular contrast measurements of Muller and Keil (1983) derived a contrast of 0.4 near disk center. Assuming a 1 % filling factor, we would expect a 4×10^{-3} contrast

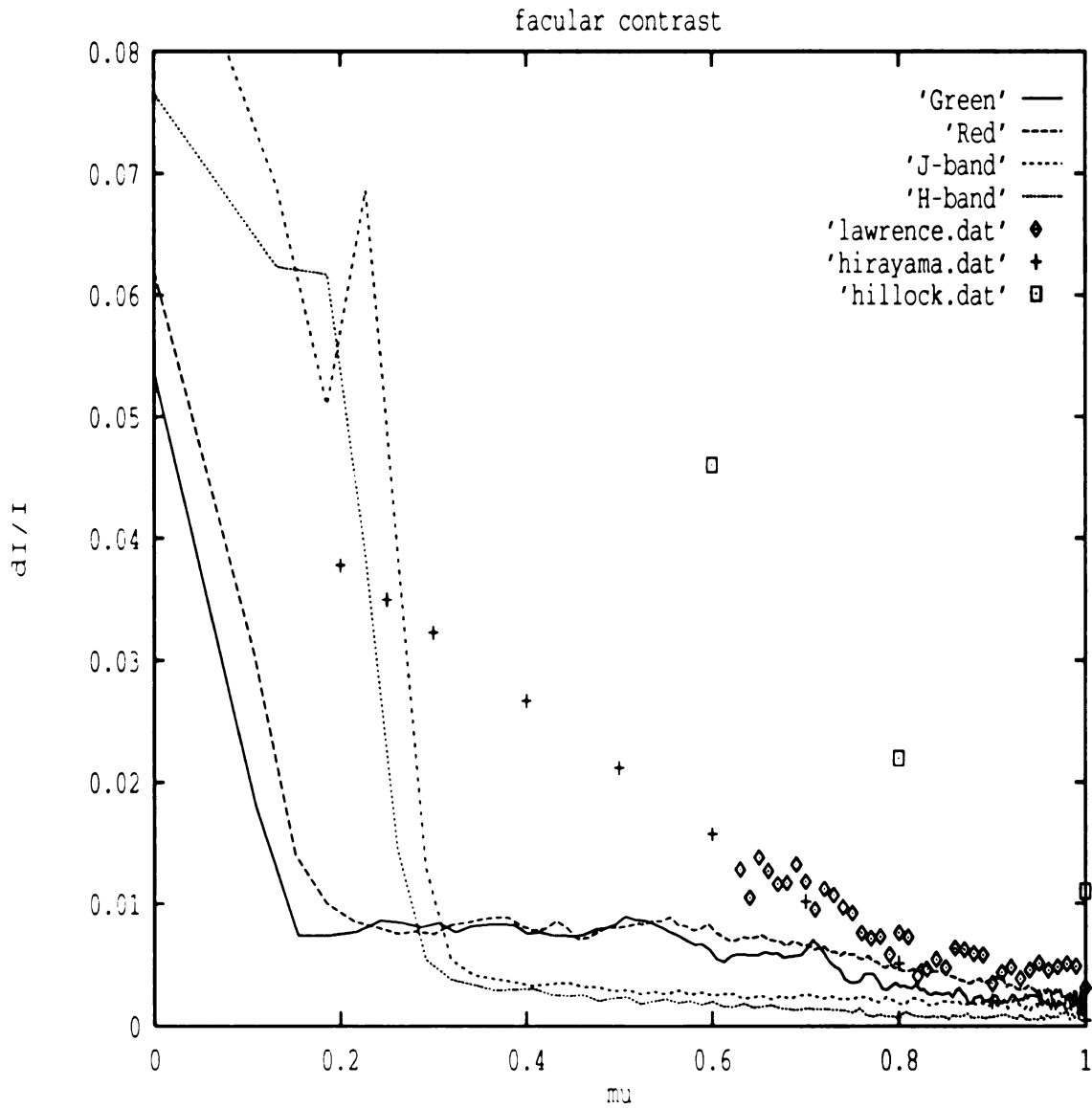


Figure 4.19 Center-to-Limb Variation of Faculae Contrast. The diamond curve was taken from Lawrence, Chapman, and Herzog (1988), the cross curve was taken from Hirayama, Hamana, and Mizugaki (1985), and the square curve was taken from the hillock model of Schatten, Mayr, Omidvar, and Maier (1986).

from spatially unresolved observations. This is in good agreement with our results.

CHAPTER 5

THE SOLAR IRRADIANCE VARIATIONS AND CONCLUSION

5.1 Introduction

The primary goal of this experiment is to identify the contribution of the various brightness structures to the total solar irradiance. The sensitivity of our instrument is limited by two factors. First, the poor spatial resolution of the SPT limits our ability to calculate the irradiance contributions of each brightness components independently. We are presently only able to isolate the sunspot and faculae contributions. Network and quiet photosphere are treated together as the "averaged photosphere". Secondly, absolute photometry with 10^{-3} accuracy from ground based observation is virtually impossible because the transparency of Earth's atmosphere is continuously changing. Relative photometry, however, can achieve high degree of accuracy with carefully chosen reference. Assuming that the intensity of the quiet sun is constant in time, it gives us a convenient reference to calculate the flux excess or deficit of each brightness component. This is a reasonable assumption on the time-scale of a few months—the duration of the dataset—for the following reasons. The radiative flux output of the photosphere is strongly modulated only by the presence of strong surface magnetic fields, like the dark sunspots and bright faculae. Preferably, we would like to use the nonmagnetic quiet photospheric intensity as the reference. However, a large quiet region inevitably includes network

bright points, and again, since we can not separate the network pixels from the nonmagnetic quiet photosphere pixels, we can only use the average quiet region photospheric intensities for the references. The filling factor of the NBP is approximately 0.01. With a spatial resolution of 6", the contrast of the network pixels is only 2×10^{-3} in the visible wavelengths as discussed in Chapter 4. The bias introduced by the inclusion of network element in the calculation of the average quiet photosphere intensity is of comparable magnitude. Since it is used as the reference for the calculation of image pixel contrast, the amplitude of the error in the contrast is 10^{-3} times the "true" contrast. This is small, and can be neglected. The limb brightness observations did suggest that the average photosphere would become brighter toward solar maximum, however, the brightness increase is small, and the error introduced can also be neglected for the time-scale considered here.

To calculate the flux deficit and excess of the sunspots and faculae, we first calculate the total irradiance of a quiet sun by integrating the average limb-darkening function over the full disk, i.e.,

$$I_{quiet} = \int_{\mu=0}^1 \int_{\theta=0}^{2\pi} \bar{L}(\mu) d\theta d\mu \quad (5-1)$$

where $\bar{L}(\mu)$ is the averaged limb-darkening function. The irradiance excess or deficit of an image pixel in unit of the total flux of the quiet sun is then given by

$$I(\vec{x}) = \frac{c(\vec{x})\bar{L}(\mu)}{I_{quiet}} = c(\vec{x})\bar{L}'(\mu) \quad (5-2)$$

where \vec{x} is the coordinate vector of the image pixel, and

$$\bar{L}'(\mu) = \frac{\bar{L}(\mu)}{I_{quiet}} \quad (5-3)$$

is the normalized limb-darkening function which, when integrated over θ and μ as in equation (5-1), gives unit total quiet sun flux.

5.2 Irradiance Contributions of Faculae and Sunspots

We have obtained the facular contrast distribution $n_{fac}(\mu, c)$ as a function of μ in Chapter 4. Multiply $n_{fac}(\mu, c)$ by the total number of image pixel at μ , the contrast c , and the normalized average limb-darkening function $\bar{L}'(\mu)$, and integrate over μ and c , then we obtain the full-disk faculae contribution to the solar irradiance in units of the total solar irradiance of the quiet sun. That is,

$$\begin{aligned} I_{fac} &= \int_{\mu=0}^1 \int_{c=-\infty}^{\infty} n_{fac}(\mu, c) c N(\mu) \bar{L}'(\mu) dc d\mu \\ &= \int_{\mu=0}^1 N_{fac}(\mu) \bar{C}_{fac}(\mu) \bar{L}'(\mu) d\mu \end{aligned} \quad (5-4)$$

where $\bar{C}_{fac}(\mu)$ is the average facular contrast function defined in equation (4-3), and $N_{fac}(\mu)$ is the total number of facular pixels at μ . The full-disk sunspot irradiance contributions can be evaluated similarly with the sunspot contrast distribution $n_{spot}(\mu, c)$,

$$I_{spot} = \int_{\mu=0}^1 \int_{c=-\infty}^{\infty} n_{spot}(\mu, c) c N(\mu) \bar{L}'(\mu) dc d\mu \quad (5-5)$$

$$= \int_{\mu=0}^1 N_{spot}(\mu) \bar{C}_{spot}(\mu) \bar{L}'(\mu) d\mu$$

Table 3 list the facular and sunspot irradiance contribution of data from 1991 observations. It is found that the total facular contribution is about a few times 10^{-4} of the total solar irradiance. The total sunspot contribution varies with sunspot number and positions, ranging from comparable to a few times that of the total facular contribution in our data.

Table 3. The Sunspots and Facular Irradiance Contributions of 1991 data

Date	Sunspots(red)	Faculae(red)	Sunspots(green)	Faculae(green)
June 4	$-1.2 \times 10^{-3*}$	0.47×10^{-3}	No data	
June 5	-1.30×10^{-3}	0.73×10^{-3}	-1.8×10^{-3}	0.67×10^{-3}
June 6	-1.7×10^{-3}	0.47×10^{-3}	-2.43×10^{-3}	0.40×10^{-3}
June 8	-3.4×10^{-3}	0.82×10^{-3}	-3.19×10^{-3}	0.97×10^{-3}
Sept 6	-1.27×10^{-3}	0.99×10^{-3}	No data	
Sept 21	-0.81×10^{-3}	0.83×10^{-3}	-0.74×10^{-3}	0.60×10^{-3}
Sept 28	-2.51×10^{-3}	0.83×10^{-3}	-1.41×10^{-3}	0.44×10^{-3}
Sept 29	-2.33×10^{-3}	0.76×10^{-3}	-1.68×10^{-3}	0.39×10^{-3}

* In unit of the total quiet sun irradiance.

It is also interesting to examine the integrand of equation (5-4) for images from consecutive time-steps, since they tell us how the facular and sunspot irradiance contributions evolve as they rotate across the Solar disk. Figure 5.1 shows the integrands of images of the June and September 1991 time series. It is clear that the facular contribution curves do not change appreciably, regardless of the changing position and area of the brightest facular area. The sunspot contribution curves, on

the other hand, show strong dependence on the position and the size of the sunspot groups, as might be expected.

5.3 The Energy Balance of Active Region

Observations with larger data bases have shown that sunspots and faculae are responsible for the short-term irradiance variations. The long-term effect of these two components are less certain. Bruning and LaBonte (1983), using monochromatic continuum images at the wing of Fe I $\lambda 5250$ line, showed that the total irradiance contribution from the magnetic features, i.e., sunspots and faculae, is nearly zero when averaged over a one-year period. Chapmann and Meyer (1986) used proxy measurements of sunspot and faculae areas of about 40 active regions to show that the irradiance excess of faculae and the deficit of sunspots roughly balance each other over the lifetime of active regions. These observations were interpreted as evidence for detailed balance between the sunspot energy deficit and facular energy excess, and there were some models (e.g., Schatten and Mayr 1985, Schatten, Mayr, Omidvar, and Maier 1986) put forward to explain these results. In these models, the energy flux blocked by the sunspots is reradiated away by the faculae. However, it is still a subject of controversy. If these results were correct, they imply that a third, or more components are responsible for the observed 11-year solar irradiance variations and there are some unknown mechanisms operating below the photosphere to channel the blocked energy to the faculae. Also, we must remember that we only measure the irradiance at Earth. The irradiance excess of faculae and deficit of sunspots may cancel each other, statements about the balance between the total energy flux is a dangerous extrapolation. We already know that faculae are not isotropic radiator. They radiate more in the direction tangent to the solar surface, since they are brighter near the limb. Thus, although a disk center facular

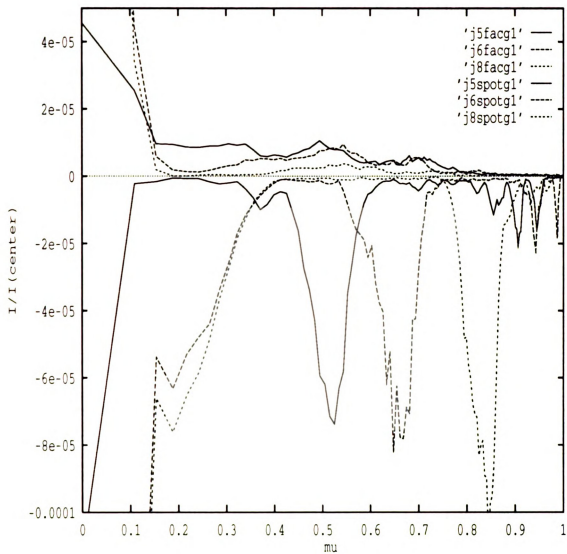


Figure 5.1 Sunspots and Faculae Irradiance Contributions.

contributes little to the total solar irradiance we observe, it still radiates measurable amount of energy in directions normal to our line-of-sight. The total energy radiated by any brightness element at any time is the integration of its radiation field over the 4π solid angle. To measure the radiation field $I(\theta, \phi)$, where θ and ϕ are the polar and azimuthal angles respectively, one would need to place detectors around the brightness element to get a faithful measurement. This is impossible in practice. Nevertheless, in the simplest model, the radiation field of any brightness element can be represented by the center-to-limb variation of its contrast assuming an azimuthal symmetric radiation field. The total energy output in excess or deficit ΔF of a brightness element with respect to the average photosphere is

$$\Delta F = 2\pi \int_{\mu=0}^{-1} c(\mu) \bar{L}'(\mu) d\mu \quad (5-6)$$

where $c(\mu)$ is the contrast of the brightness element at μ . Thus, the total flux excess radiated by all the facular elements under consideration is

$$\begin{aligned} \mathbf{F}_{fac} &= \int_{\mu'=1}^0 N_{fac}(\mu') \Delta F_{fac} d\mu' \\ &= 2\pi N_{fac} \int_{\mu=0}^1 \bar{C}_{fac}(\mu) \bar{L}'(\mu) d\mu \end{aligned} \quad (5-7)$$

where $\bar{C}_{fac}(\mu)$ is the average contrast function of the faculae, and N_{fac} is the total number of facular pixels in the area under consideration. The energy flux deficit of the sunspots can be calculated similarly using the sunspot contrast function. Note that equation (5-4) and (5-7) give only the instantaneous irradiance and energy

output. They should be integrated over the lifetime of the faculae and sunspots to obtain the total irradiance and energy output.

Our observations of the facular contrast function showed that it does not have large variation over the time scales considered here. Hence, the use of an average contrast function for all the faculae can be justified. The sunspot contrast function, however, varies with the size of the sunspot. Thus, the contrast function of any sunspot must be measured separately. Another difficulty associated with the problem of active region energy budget is that we don't know where to draw a line for the active region, since we don't know how far-reaching the sunspots affect the photosphere. Also, all the features on the sun spend half of their lifetime on the invisible side of the solar hemisphere due to solar rotation. Thus, there is always some uncertainty in any observation trying to prove or disprove the energy balance between sunspot and faculae.

Facing the observational difficulties associated with the problem of active region energy balance, Kuhn's (1992) idea that the horizontal energy transport is more important than the vertical energy transport in supplying the excess energy of faculae seems to provide a natural explanation for the observed irradiance balance between faculae and sunspots. Since horizontal energy transport is more effective, the energy blocked by sunspots is deposited in the surrounding layer, and then picked up by the faculae if they appear simultaneously. Thus, the total energy radiated by the sunspots and faculae in an active region is balanced. However, the sunspot blocked energy has not necessarily been channeled to the faculae. There are occasions where isolated sunspots appear without accompanying facular regions. In this case, the blocked energy is re-radiated by the surrounding photosphere.

The above picture is attractive, but how do we go from energy balance to

irradiance balance? Judging from the very different form of the integral equations of irradiance (Equation (5-4)) and total flux (Equation (5-7)), It is hard to understand how the time-integral of the irradiance and flux integral of sunspot and faculae can be balanced simultaneously. On the other hand, if we consider the irradiance excess or deficit of a single magnetic element $\delta I(\mu)$ when it is positioned at μ on the solar disk, then

$$\delta I(\mu) = C(\mu)L(\mu) \quad (5 - 8)$$

If we trace it across the solar disk, and integrate over time, then the time-integrated irradiance contribution is exactly the flux integral of equation (5-7). Thus, integrating a large number of faculae and sunspots over a long period of time, as the observations of Bruning and LaBonte (1983) and Chapman and Meyer (1986), is equivalent to measuring the average flux integral of the faculae and sunspot. It is then not too surprising to find that the time-integrated irradiance contribution of the two components should balance each other.

5.4 The Average Photosphere

The limb brightness observations of Kuhn Libbrecht, and Dicke (1988) demonstrated the existence of a global scale brightness structure. They also argued that the contrast of this structure is not subject to a facular limb brightening function, but has a μ independent contrast. The amplitude of this global scale structure should be of a few times 10^{-3} , depending on the phase of the solar cycle. However, in a full disk contrast image, this structure is mingled with the extended facular regions near the limb. The large scale scattered light noise further hampers our ability to detect this structure. Since the scattered light noise appears randomly in

the images, there is no systematic way of removing it. The data base is not large enough to reduce its effect by direct averaging either. Thus, we applied a biased averaging method by discarding all the pixels with contrast greater than 0.6 % or less than -0.6 %. This threshold is chosen based on the observation that the quiet region network contrast is $\approx 0.2\%$, and a 3σ cut should exclude the faculae and sunspots pixels. This also excludes most of the scattered light error in the images. The averaged contrast images of 1991 visible wavelengths data are shown in Figure 5.2 and Figure 5.3. We did not attempt to do the same averaging for the infrared wavelength data, since the mosaicking error is of the order of a few times 10^{-3} . This is large enough to mask the small signal in the infrared. Near the limb, the green average contrast image shows that some of the additive error leaked through the 3σ filtering, while the red average contrast image appears cleaner. This is not unexpected, since the amplitude of the error in the green images is smaller and has a higher probability of leaking through the filter. Despite the difficulty in averaging, both images show brighter active latitudes compared with the solar equator and the pole regions. This is consistent with the limb brightness observations.

To check if we can reproduce the limb brightness profile observed by the solar oblateness telescope, the pixels with the same latitude were averaged to make a contrast profile as a function of latitude l for both colors. This is assuming that the contrast of this large-scale structure does not change appreciably as across the solar disk. The results are shown in Figure 5.4. The equivalent brightness temperature profile is shown in Figure 5.5. Considering the very different amplitudes and distribution of the large scale noise in the green and red contrast images, it is surprising to find the excellent agreement of the two curves between -70° and 70° . The amplitude in the green is slightly larger, in agreement with the assumption that

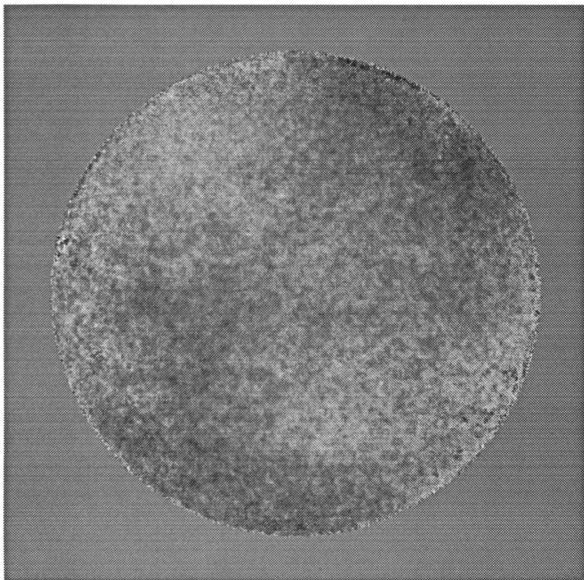


Figure 5.2 The Average Photosphere in Green Bandpass.

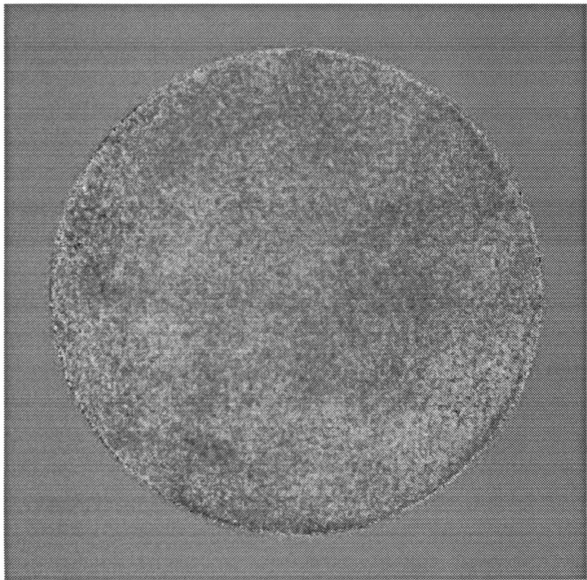


Figure 5.3 The Average Photosphere in Red Bandpass

this signal is of thermal origin. The data 70° poleward had only a small number of pixels for averaging, and the discrepancy between the two colors in these region are not unexpected. Comparing this plot with the limb brightness temperature of Kuhn et al, it shows qualitatively the same feature. We see temperature excess at both north and south active latitudes. The small dip at the equator also agrees well. To check if these features are μ independent, curves averaging over different range of μ were calculated, and it showed that the temperature profile of Figure 5.3 is indeed independent of μ . The amplitude of the temperature excess at active latitudes with respect to the polar area is approximately 2 K. This is a large drop from the 7 K amplitude from 1990. Unfortunately, the limb brightness experiment was discontinued after the summer observing season of 1990, and no data were available for comparison with this observation. The ERB data in Figure 1.1 shows that the irradiance remains near peak value on the first half of 1991, and only shows some sign of decrease. Thus, the 2 K amplitude does not seem to agree well with the ERB data. This maybe due to error from the 3σ filtering. Nevertheless, the position of the peak at about 20° south and about 30° north is also consistent with the trend in the shift of the position of the peak observed in the limb brightness observations. Thus, we believe that this is the large-scale brightness structure observed by the limb brightness observations.

5.5 Interpretations

We have successfully resolved the photospheric network, and we can measure its rms contrast as it varies with solar cycle. However, we still cannot deduce its irradiance contribution to our data. Thus we still cannot answer the important question of whether the active network contrast is responsible for the observed solar cycle irradiance variations. Even if we can reduce the network irradiance

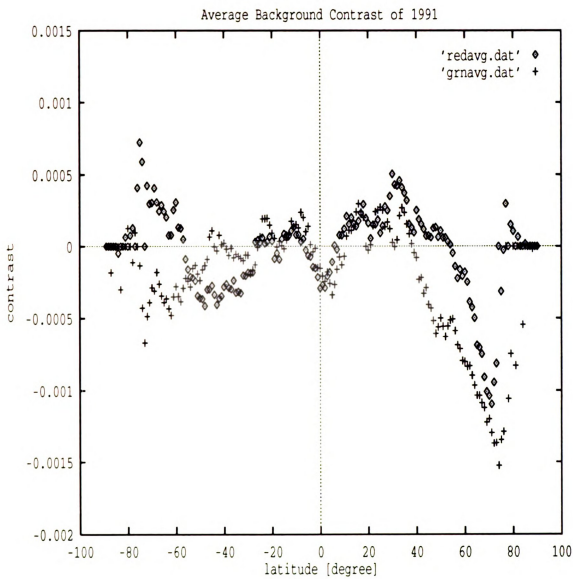


Figure 5.4 Limb Brightness Profile of the Average Photosphere.

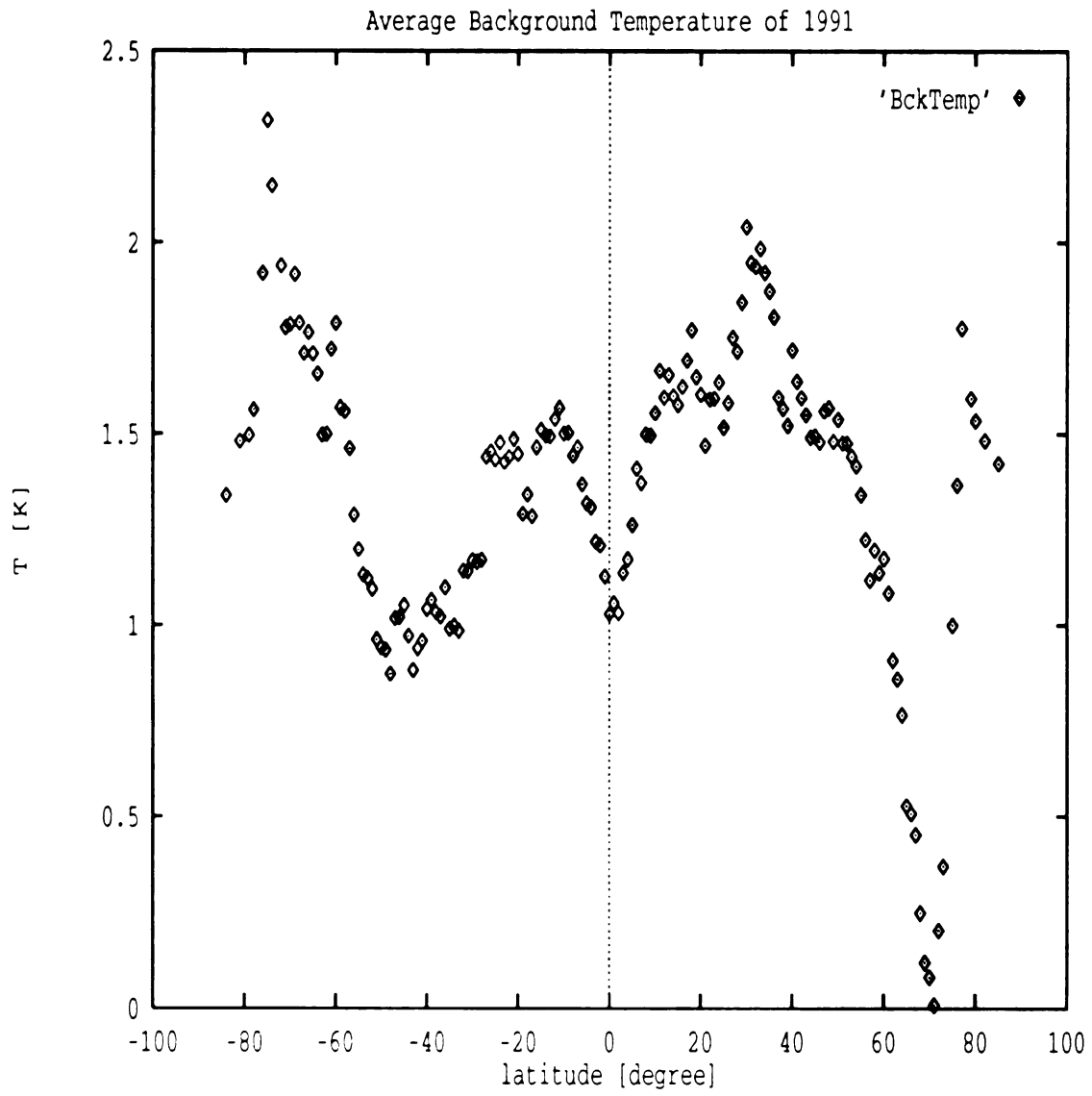


Figure 5.5 Brightness Temperature Profile of the Average Photosphere.

contribution, it would still take observations spanning over the whole phase of a solar cycle before we can make any conclusions. Thus, it seems appropriate to look into other kinds of observations which might provide useful information to help resolve the confusion.

The observations of the solar p -mode oscillations provide information about the interior of the Sun that is inaccessible with photometric observations. One of the major differences between the active network model of Foukal et al and the hot active-region photosphere model of Kuhn et al is the thermal structure of the Solar Convection Zone (SCZ). The active network model speculated that the changing contrast and area of the active network is the cause of the Solar cycle irradiance variations, but it did not elaborate on how the changing active network might affect the thermal structure of the underlying solar atmosphere. The calculations of Spruit assume the SCZ redistributes the energy not radiated away during Solar minimum uniformly throughout the SCZ. Thus the thermal structure of the SCZ would not deviate significantly from a spherically symmetric model. Kuhn et al's model, on the other hand, argued that the thermal structure of the solar photosphere along the active latitudes is modulated by the toroidal field deep below. In a separate paper Kuhn (1988) argued that a small thermal perturbation originated deep in the convection zone would not be smoothed out uniformly over the entire solar convection zone, but would produce a visible temperature perturbation dT in a shallow layer below the photosphere. This would produce an observable asphericity in the thermal structure of the photosphere. Goode and Kuhn (1990) developed a model in which the brightness temperature dT was related to the local effective sound speed. They were able to explain consistently the 2nd and 4th order p -mode splitting coefficients variations observed by various groups over different phase of the

solar cycle. Moreover, the measured centroid frequency shifts of low-order p -modes also agrees well with the calculated shifts. The 2nd and 4th order p -mode splitting coefficients measure the deviation of the structure of the SCZ from a spherically symmetric model. Thus, the calculations of Spruit are inconsistent with the p -mode splitting coefficients observations. The centroid frequency shifts are proportional to the temperature excess dT . The active network model requires the SCZ to store the excess energy not radiated away during solar minimum. Thus the SCZ should be hotter during Solar minimum. The amplitude of the temperature increase of the SCZ may be too small to be observed, but the sign of the temperature perturbation dT should predict a centroid frequency shifts with a 180 phase shift with respect to the shifts predicted by the limb brightness temperature observations.

The p -mode frequency shift and splitting observations also provide information on the radial structure of the temperature perturbations. Since the penetration depth of a mode depends on the mode frequency, the radial temperature perturbation would produce frequency dependent frequency shifts. Comparing the BBSO frequency shifts observations between 1986 and 1988 with model radial temperature perturbation profile, it was concluded that the radial temperature perturbation must peak a few hundred km below the solar photosphere, and then decreases toward the photosphere. Exactly how the toroidal field setup the observed temperature perturbation is not easily solvable, nevertheless, Kuhn (1991) was able to show with numerical simulation qualitatively how a small perturbation at the base of a convective box can evolves in time to produce the observed radial temperature perturbation profile. These results strongly support the interpretations of the observed dT as a true thermal perturbation originated deep in the SCZ. The active network model, on the other hand, seems unlikely to produce the thermal structure

observed by the seismology observations.

5.5 Conclusion

We presented multi-wavelength measurements of, (1) the photospheric network contrast, its center-to-limb variation, and a statistical measurement of its characteristic size; (2) the facular contrast and the facular contribution to the total solar irradiance; (3) the sunspot contribution to the total solar irradiance; (4) the brightness profile of the average photosphere. From these measurements, we discussed the various possible physical processes that could lead to the observed active region irradiance balance, and the solar cycle irradiance variation. These observations also demonstrated that, with carefully designed instruments, observation techniques, and data reduction algorithms, it is possible to achieve better than 10^{-3} /pixel accuracy on a spatial scale ranging from 10^4 km to the full disk. We feel justified to say that we have achieved what we set out to do. However, it is not enough, still. It is clear that more observations spanning the whole phase of the solar cycle are needed to provide information for a full understanding of the physics at work. Beside a longer time series, improved spatial resolution is indispensable to resolve the network contribution to the irradiance variation. This is one problem that we are unable to solve due to the limited spatial resolution of our instruments. The first dataset obtained with the improved optics of the SPT with 2" resolution showed that it does not provide more new information than what we can get with the medium resolution optics. We feel that sub-arcsecond resolution is needed. Hopefully instruments of upcoming projects will provide enough resolution to solve this problem.

APPENDICES

APPENDIX A

THE GAUGE FREEDOM OF THE GAIN ITERATING ALGORITHM

In our 1991 paper (Kuhn, Lin, and Loranz 1991) we stated that there is an ambiguity associated with the solution of the gain iterating algorithm, due to the gauge invariant property of the formulation under a gauge transformation of the form

$$G(\mathbf{x}) \rightarrow G(\mathbf{x}) + \phi(\mathbf{x}) \quad (A-1)$$

where $G(\mathbf{x})$ is the logarithm of the gain function of the imaging array, and $\phi(\mathbf{x})$ is the gauge of the transformation. We also pointed out that one of the possible form for $\phi(\mathbf{x})$ is

$$\phi(\mathbf{x}) = \vec{\beta} \cdot \vec{\mathbf{x}} \quad (A-2)$$

where $\vec{\beta}$ is a constant vector. In other words, we can only determine a solution of the algorithm up to a linear constant term in the logarithm of the gain. However, the question of whether other possible form of $\phi(\mathbf{x})$ exist was not fully investigated. In this section, we will demonstrate that the solution for $\phi(\mathbf{x})$ is equation (A-2) is the only possible solution of the algorithm as follows.

Assume that $G(\mathbf{x})$ is the logarithm of a solution of the gain integrating algorithm. Let's now perform a transformation of the form in equation (A-1), and substitute $G(\mathbf{x}) + \phi(\mathbf{x})$ in the formulation. It is then straightforward to show that the iterating formula in Chapter 3 (equation (3-1)) becomes

$$G^{r+1}(\mathbf{x}) = K(\mathbf{x}) + \frac{1}{n(\mathbf{x})} \sum_{i < j} [G^r(\mathbf{x} - \mathbf{a}_i + \mathbf{a}_j) + G^r(\mathbf{x} - \mathbf{a}_j + \mathbf{a}_i) - (\phi(\mathbf{x}) - \phi(\mathbf{x} - \mathbf{a}_i + \mathbf{a}_j)) - (\phi(\mathbf{x}) - \phi(\mathbf{x} - \mathbf{a}_j + \mathbf{a}_i))] \quad (A-3)$$

where all the symbols are as defined in Section 3.3.4. Thus, the condition that $\phi(\mathbf{x})$ must satisfy to make the transformation gauge invariant is

$$\sum_{i < j} [(\phi(\mathbf{x}) - \phi(\mathbf{x} - \mathbf{a}_i + \mathbf{a}_j)) + (\phi(\mathbf{x}) - \phi(\mathbf{x} - \mathbf{a}_j + \mathbf{a}_i))] = 0 \quad (A-4)$$

Note that this equation must hold for any \mathbf{x} within the domain of the array. Define $\mathbf{a}_i - \mathbf{a}_j \equiv d\mathbf{x}_{ij}$, we can rewrite equation (A-4) as

$$\sum_{i < j} [(\phi(\mathbf{x}) - \phi(\mathbf{x} - d\mathbf{x}_{ij})) + (\phi(\mathbf{x}) + \phi(\mathbf{x} + d\mathbf{x}_{ij}))] = 0 \quad (A-5)$$

In the special case that the shifts are infinitesimal, equation (A-5) reduces to a Laplace equation. There are many solutions that will satisfy the Laplace equation, e.g., any harmonic function. However, since equation (A-5) must be satisfied with arbitrary choice of number of shifted images and size of shift, $\phi(\mathbf{x})$ must be an odd function around the point under consideration. This is a more restrictive condition than the Laplace equation, but there are still a large number of functions that satisfy

this condition. In addition to equation (A-5), there is another criteria that $\phi(\mathbf{x})$ must satisfy. That is, equation (A-5) must be satisfied on every point in the valid pixel domain of the imaging array, or, equation (A-5) is translational invariant. Summarizing, we have two conditions that $\phi(\mathbf{x})$ must satisfy to make the gauge transformation of equation (A-1) invariant:

$$\phi(\mathbf{x} + d\mathbf{x}) = -\phi(\mathbf{x} - d\mathbf{x}) \quad (\text{A} - 6)$$

$$\phi(\mathbf{x} + \mathbf{x}_0 + d\mathbf{x}) = -\phi(\mathbf{x} + \mathbf{x}_0 - d\mathbf{x}) \quad (\text{A} - 7)$$

where $d\mathbf{x}$ is the displacement vector around \mathbf{x} between a pair of images, and \mathbf{x}_0 is a translation vector. To examine what kind of solutions condition (A-6) and (A-7) yield, let's expand $\phi(\mathbf{x})$ by a polynomial expansion around some arbitrary point \mathbf{x} , i.e.,

$$\phi(\mathbf{x} + d\mathbf{x}) = \sum_{n=0}^N a_n(\mathbf{x}) d\mathbf{x}^n \quad (\text{A} - 8)$$

The condition in equation (A-6) requires that all the even order coefficients, a_{2i} where i is arbitrary integer, must vanish. Condition (A-7) further requires that all the odd coefficients except the first order term vanish. This is due to the fact that any term in the expansion with 3rd power or higher will introduce terms with even power, thus violating condition (A-6). Thus, the only possible family of solution that satisfies both equation (A-6) and equation(A-7) is

$$\phi(\mathbf{x}) = \vec{\beta} \cdot \mathbf{x} \quad (A - 9)$$

This proves our observations in the 1991 paper that there can be an ambiguity in the form of a linear gradient term in the logarithm of the gain function in the solution of the gain iterating algorithm, and that it is the only possible form of the ambiguity.

The above derivation is valid for an perfect infinite array. However, notice that we don't have an infinite array, and there are always bad pixels. Thus, the square symmetry of equation (A-5) is not satisfied in these regions. However, as long as the numbers of bad pixels and boundary pixels are small, the solution of the algorithm will not be significantly affected, and an perfect infinite array approximation can be assumed. This result was confirmed by numerical experiments.

APPENDIX B

LEAST SQUARE ALGORITHM TO FIND THE DISK CENTER COORDINATES OF FULL DISK SOLAR IMAGE

A CCD image can be described by a 3-dimensional function (x , y , and intensity) $I(\vec{r}) = I(x, y)$, where $\vec{r} = (x, y)$ is a position vector in the array coordinates system. A solar image without any distortion can be considered symmetrical about its center, (x_c, y_c) . The image function $I(\vec{r})$ have radial symmetry if the origin of the coordinates system is translated to (x_c, y_c) , i.e., $I(x \rightarrow x - x_c, y \rightarrow y - y_c) = I(\vec{r}) = I(r)$. The solar images have a linear gradient introduced by the use of sky as the flatfield. Thus, the image function that describes the sky-calibrated solar image is

$$\begin{aligned} S(x, y) &= I(x, y)g(x, y) && (B - 1) \\ &= I(r)(1 + \alpha x + \beta y) \end{aligned}$$

where α and β are the amplitude of the sky gradient in the x and y direction, respectively. Note that the coordinates system used now is the solar center coordinates system. However, we have only limited accuracy in the knowledge of (x_c, y_c) . Given an estimated disk center position with a small error $(x'_c, y'_c) = (x_c + \Delta x, y_c + \Delta y)$, the image function $S'(\vec{r}')$ that describes the observed image in the coordinates system of (x'_c, y'_c) is

$$\begin{aligned}
S'(x', y') &= S(x - \Delta x, y - \Delta y) & (B - 2) \\
&= I(x - \Delta x, y - \Delta y)g(x - \Delta x, y - \Delta y) \\
&\approx [I(r) + D(r)(x \Delta x + y \Delta y)](1 + \alpha(x - \Delta x) + \beta(y - \Delta y))
\end{aligned}$$

where $D(r) = \frac{1}{r} \frac{dI(r)}{dr}$. Given the two functions $I(r)$ and $D(r)$, we can find the parameters $\alpha, \beta, \Delta x$, and Δy by fitting a observed solar image $d(\vec{r}')$ to the function S' with least square fitting method. Define

$$\sigma^2 = \sum_{\vec{r}'} [S'(\vec{r}') - d(\vec{r}')]^2 \quad (B - 3)$$

and minimize σ^2 with respect to $\alpha, \beta, \Delta x$, and Δy gives 4 equations,

$$\frac{d\sigma^2}{d\alpha} = 0 \quad (B - 4)$$

$$\frac{d\sigma^2}{d\beta} = 0 \quad (B - 5)$$

$$\frac{d\sigma^2}{d\Delta x} = 0 \quad (B - 6)$$

and

$$\frac{d\sigma^2}{d\Delta y} = 0 \quad (B - 7)$$

Assume that $\alpha, \beta, \Delta x$, and Δy are small, then to the first order of these parameters, we have a system of linear equations:

$$\begin{aligned} & \sum_{\bar{r}} [x^2 D^2] \Delta x + \sum_{\bar{r}} [xy D^2] \Delta y + \sum_{\bar{r}} [x^2(2I - d)D - I(I - d)]\alpha \\ & + \sum_{\bar{r}} [xy(2I - d)D]\beta = \sum_{\bar{r}} [x(d - I)D] \end{aligned} \quad (B - 8)$$

$$\begin{aligned} & \sum_{\bar{r}} [xy D^2] \Delta x + \sum_{\bar{r}} [y^2 D^2] \Delta y + \sum_{\bar{r}} [xy(2I - d)D]\alpha \\ & + \sum_{\bar{r}} [y^2(2I - d)D - I(I - d)]\beta = \sum_{\bar{r}} [y(d - I)D] \end{aligned} \quad (B - 9)$$

$$\begin{aligned} & \sum_{\bar{r}} [x^2(2I - d)D - I(I - d)] \Delta x + \sum_{\bar{r}} [xy(2I - d)D] \Delta y + \sum_{\bar{r}} [x^2 I^2]\alpha \\ & + \sum_{\bar{r}} [xy I^2]\beta = \sum_{\bar{r}} [x(d - I)I] \end{aligned} \quad (B - 10)$$

$$\begin{aligned} & \sum_{\bar{r}} [xy(2I - d)D] \Delta x + \sum_{\bar{r}} [y^2(2I - d)D - I(I - d)] \Delta y + \sum_{\bar{r}} [xy I^2]\alpha \\ & + \sum_{\bar{r}} [y^2 I^2]\beta = \sum_{\bar{r}} [y(d - I)I] \end{aligned} \quad (B - 11)$$

which can be solved for α , β , Δx , and Δy easily.

Since we do not know the true center at the beginning, the functions $I(r)$ must be calculated with the estimated center (x'_c, y'_c) , i.e.,

$$I'(r') = \int_{r'=r_0} S'(\bar{r}') d\theta \quad (B - 12)$$

We can estimate the error of this calculation by integrating in the coordinates system of the true center. Discarding terms with 2nd order and higher of Δx and Δy , we have

$$\begin{aligned}
r' &= [(x - \Delta x)^2 + (y - \Delta y)^2]^{1/2} & (B - 13) \\
&= [r^2 + \Delta r^2 - 2r(\cos\theta \Delta x + \sin\theta \Delta y)]^{1/2} \\
&\approx r + (\cos\theta \Delta x + \sin\theta \Delta y)
\end{aligned}$$

Thus,

$$\begin{aligned}
I'(r') &= \int_{r=r_0-(\cos\theta\Delta x+\sin\theta\Delta y)} I(r)(1 + \alpha\cos\theta + \beta r\sin\theta)d\theta & (B - 14) \\
&= \int [I(r_0) + \frac{dI(r)}{dr}|_{r=r_0}(\cos\theta \Delta x + \sin\theta \Delta y)](1 + \alpha\cos\theta + \beta r\sin\theta)d\theta
\end{aligned}$$

Note that all the terms with 1st order of Δx , Δy , α , and β contain either $\cos\theta$ or $\sin\theta$, which vanish when integrating over θ . Thus, the error in $I'(r')$ is of second order or higher of Δx , Δy , α , and β , and $I'(r')$ can be used for $I(r)$.

BIBLIOGRAPHY

BIBLIOGRAPHY

- Allen, C. W. 1963. *Astrophysical Quantities*. *The Athlone Press*.
- Beckers, J. M. 1968. Photospheric brightness differences associated with the solar supergranulation. *Solar Phys.* **5**:309-322.
- Bruning, D. H., and LaBonte, B. J. 1983. Interpretation of solar irradiance variations using ground-based observations. *Astrophys. J.* **271**:853-858.
- Chandrasekhar, S., and Breen, F. H. 1946. On the continuous absorption coefficient of the negative hydrogen ion. *Astrophys. J.* **104**:430.
- Chandrasekhar, S. 1961. *Hydrodynamic and hydromagnetic stability*. *Oxford University Press*.
- Chapman, G. A., Herzog, A. D., Lawrence, J. K., and Shelton, J. C. 1986. Time-integrated energy budget of a solar activity complex. *Nature* **319**:654-655.
- Chapman, G. A., and Meyer, A. D. 1986. Solar irradiance variations from photometry of active regions. *Solar Phys.* **103**:21-31.
- Chapman, G. A. 1987. Variations of solar irradiance due to magnetic activity. *Ann. Rev. Astron. Astrophys.* **25**:633-667.
- Deinzer, W., Hensler, G., Schüssler, M., and Weisshaar, E. 1984. Model calculations of magnetic flux tubes, II. Stationary results for solar magnetic elements. *Astro. Astrophys.* **139**:435-449.
- Dicke, R. H., and Goldenberg, H. M. 1967. Solar oblateness and general relativity. *Phys. Rev. Lett.* **18**:313-315.
- Donnelly, R. F., Harvey, J. W., Heath, D. F., and Repoff, T. P. 1985. Temporal characteristics of the solar UV flux and He I line at 1083 nm. *J. of Geophys. Res.* **90**:6267-6273.

- Foukal, P. and Fowler, L. 1984. A Photospheric study of heat flow at the solar photosphere. *Astrophys. J.* **281**:442-454.
- Foukal, P. and Lean, J. 1988. Magnetic modulation of solar luminosity by photospheric activity. *Astrophys. J.* **328**:347-357.
- Foukal, P., Little, R., Mooney, J., 1989. Infrared imaging of sunspots and faculae at the photospheric opacity minimum. *Astrophys. J.* **336**:L33-L35.
- Foukal, P. 1990. Solar Astrophysics. *John Wiley & Sons, Inc.*
- Foukal, P., Little, R., Graves, J., Rabin, D. and Lynch, D. 1990. Infrared Imaging of Faculae at the Deepest Photospheric Layers. *Astrophys. J.* **353**:712-715.
- Frazier, E. N. 1970. Multi-channel magnetograph observations. II. Supergranulation. *Solar Phys.*, **14**:89-111.
- Fröhlich, C., Foukal, P. V., Hickey, J. R., Hudson, H. S., and Willson, R. C. 1991. Solar irradiance variability from modern measurements. *The sun in time*:11-29.
- Goode, P. R. and Kuhn, J. R. 1990. Consistency in trends in helioseismic data and photospheric temperature data through the solar cycle. *Astrophys. J.* **356**:310-314.
- Harvey, J. W. 1984. Helium 10830 Å irradiance: 1975-1983. *Solar irradiance variations on active region time scales. NASA Conf. Publ.* **2310**:197-211.
- Hirayama, T. Hamana, S. and Mizugaki, K. 1985. Precise wideband photometry of photospheric faculae with an emphasis on the disk center. *Solar Phys.* **99**:43-54.
- Hudson, H. S. 1988. Observed variability of the solar luminosity. *Ann. Rev. Astron. Astrophys.* **26**:474-507.
- Jackson, J. D. 1975. Electrodynamics. *John Wiley & Sons, Inc.*
- Keil, S. L., Kuhn, J. R., Lin, H., and Reardon, K, 1992. Simultaneous IR and visible light measurements of the solar granulation. *Proceeding of IAU Symposium 154: Infrared Solar Physics* in press.
- Knölker, M., Schüssler, M., and Weisshaar, E., 1988. Model calculations of magnetic flux tubes, III. Properties of solar magnetic elements. *Astron. and Astrophys.* **194**:257-267.

- Koutchmy, S. 1978. Super granulation in the deep photosphere. *Deuxième assemblée européenne de physique solaire*. **282**:155-159.
- Kuhn, J. R., Libbrecht K. G., and Dicke R. H. 1988. The surface temperature of the sun and changes in the solar constant. *Science* **242**:908-911.
- Kuhn, J. R. 1988. Helioseismological splitting measurements and the non-spherical solar temperature structure. *Astrophys. J. Letts*. **331**:L131-L133.
- Kuhn, J. R., Lin H. and Loranz D. 1991. Gain calibrating nonuniform image-array data using only the image data. *Publications of the Astronomical Society of the Pacific* **103**:1097-1108.
- Kuhn, J. R. 1991. Inferring solar structure variations from photospheric and helioseismic observations. *Advances in Space Research* **11**:171-184.
- Kuhn, J. R., 1992. What causes cycle-related global solar changes? *The 1992 Ann. GONG Meeting*, Ed. T. Brown, *PASP* in press.
- Lang, K. R. 1974. *Astrophysical Formulae*. Springer-Verlag.
- Lawrence, J. K. 1988. Multi-color photometric observations of facular contrast. *Solar Phys.* **116**:17-32.
- Lawrence, J. K., Chapman, G. A., and Herzog, A. D. 1988. Photometric determination of facular contrast near the solar disk center. *Astrophys. J.* **324**:1184-1193.
- Leighton, R. B. 1964. Transport of magnetic fields on the sun. *Astrophys. J.* **140**:1559-1562.
- Libbrecht, K. G., and Kuhn, J. R., 1985. On the facular contrast near the solar limb. *Astrophys. J.* **299**:1047-1050.
- Liu, S. 1974. White light network in the solar photosphere. *Solar Phys.*, **39**:297-300.
- McPherson, M., Lin, H., and Kuhn, J. R. 1991. Infrared array measurements of sunspot magnetic fields. *Solar Phys.* **139**:255-266.
- Mehlretter, J. P. 1974. Observations of photospheric faculae at the center of the solar disk. *Solar Phys.* **38**:43-57.
- Muller, R. 1977. Morphological properties and origin of the photospheric facular granules. *Solar Phys.* **52**:249-262.

- Muller, R. 1983. The dynamical behavior of facular points in the quiet photosphere. *Solar Phys.* **85**:113-121.
- Muller, R. and Keil, S. 1983. The characteristic size and brightness of facular points in the quiet photosphere. *Solar Phys.* **87**:243-250.
- Nishikawa, N. 1990a. Estimation of total irradiance variations with the CCD solar surface photometer. *Astrophys. J.* **359**:235-245.
- Nishikawa, N., 1990b. A new system of precise full-disk solar surface photometry. *Astrophys. J. Suppl.* **74**:315-323.
- Nishikawa, N. and Hirayama, T. 1990. Facular structures derived from precise two-color contrast observations. *Solar Phys.* **127**:211-228.
- Parker, E. N. 1987a. The dynamical oscillation and propulsion of magnetic fields in the convection zone of a star. I. General considerations. *Astrophys. J.* **312**:868-879.
- Parker, E. N. 1987b. The dynamical oscillation and propulsion of magnetic fields in the convection zone of a star. II. Thermal shadows. *Astrophys. J.* **321**:984-1008.
- Parker, E. N. 1987c. The dynamical oscillation and propulsion of magnetic fields in the convection zone of a star. III. Accumulation of heat and the onset of the Rayleigh-Taylor instability. *Astrophys. J.* **321**:1009-1030.
- Rabin, D. 1992. Spatially extended measurements of magnetic field strength in solar plages. *Astrophys. J.* **391**:832-844.
- Schatten, K. H., and Mayr, H. G. 1985. On the maintenance of sunspots: An ion hurricane mechanism. *Astrophys. J.* **299**:1051-1062.
- Schatten, K. H., Mayr, H. G., Omidvar, K., and Maier, E. 1986. A hillock and cloud model for faculae. *Astrophys. J.* **311**:460-473.
- Schatten, K. H. and Mayr, H. G. 1991. On the contrast of facular hillocks in the infrared. *Astrophys. J.* **372**:728-732.
- Simon, G. W. and Leighton, R. B. 1964. Velocity fields in the solar atmosphere. III. Large-scale motions, the chromospheric network, and magnetic fields. *Astrophys. J.* **140**:1120-1147.

- Skumanich, A., Smythe, C., and Frazier, E. N. 1975. On the statistical description of inhomogeneities in the quiet solar atmosphere. I. Linear regression analysis and absolute calibration of multichannel observations of the Ca+ emission network. *Astrophys. J.* **200**:747-764.
- Solanki, S. K., Ruedi, I., and Livingston, W. 1992. 1.56 μm observations and depth of sunspot penumbrae. *Proceeding of IAU Symposium 154, Infrared Solar Physics* in press.
- Spruit, H. C. 1977. Heat flow near obstacles in the solar convection zone. *Solar Phys.* **55**:3-14.
- Spruit, H. C. and Zwaan, C. 1981. The size dependence of contrasts and numbers of small magnetic flux tubes in an active region. *Solar Phys.* **70**:207-228.
- Spruit, H. C. 1991. Theory of Luminosity and Radius Variations. *The Sun in Time*, 118-158.
- Vainstein, S. I., Kuklin, G. V., and Maksimov, V. P. 1977. On a possible mechanism of solar faculae heating. *Solar Phys.* **53**:15-23.
- Vernazza, J. E., Avrett, E. H., and Loeser, R. 1976. Structure of the solar chromosphere. II. The underlying photosphere and temperature-minimum region. *Astrophys. J. Suppl.* **30**:1-60.
- Wang, H. and Zirin, H. 1987. The contrast of faculae near the solar limb. *Solar Phys.* **110**:281-293.
- Worden, S. P. 1975. Infrared observations of supergranulation temperature structure. *Solar Phys.* **45**:521-532.
- Willson, R. C., Gulkis, S., Janssen, M., Hudson, H. S., and Chapman, G. A. 1981. Observations of solar irradiance variability. *Science* **211**:700-702.
- Willson, R. C. and Hudson, H. S. 1988. Solar luminosity variations in solar cycle 21. *Nature* **332**:810-812.
- Zirin, H. 1988. *Astrophysics of the Sun*. Cambridge University Press.

MICHIGAN STATE UNIV. LIBRARIES



31293007944899